UNIVERSITY OF BELGRADE

FACULTY OF PHYSICS

Dušan Vudragović

FARADAY WAVES IN ULTRACOLD DIPOLAR BOSE GASES

Doctoral dissertation

Belgrade, 2019

УНИВЕРЗИТЕТ У БЕОГРАДУ

ФИЗИЧКИ ФАКУЛТЕТ

Душан Вудраговић

Фарадејеви таласи у ултрахладним диполним Бозе гасовима

Докторска дисертација

Београд, 2019. година

Thesis advisor, Committee member:

Dr. Antun Balaž

Research Professor

Institute of Physics Belgrade

University of Belgrade

Committee member:

Dr. Ivana Vasić

Associate Research Professor

Institute of Physics Belgrade

University of Belgrade

Committee member:

Prof. Dr. Milan Damnjanović

Professor

Faculty of Physics

University of Belgrade

Committee member:

Prof. Dr. Milan Knežević

Professor

Faculty of Physics

University of Belgrade

Acknowledgements

This thesis was completed at the Scientific Computing Laboratory, National Center of Excellence for the Study of Complex Systems, Institute of Physics Belgrade under the supervision of Dr. Antun Balaž. The presented research was supported by the Ministry of Education, Science, and Technological Development of the Republic of Serbia under projects ON171017 (led by Dr. Antun Balaž), and III43007 (work-package PP4, led by Dr. Aleksandar Bogojević). I thank Dr. Antun Balaž and Dr. Aleksandar Bogojević for giving me the opportunity to participate and contribute to these projects.

Trying to avoid any pathetic here, I would like to say that any discussion with Antun somehow makes you feel smart, and makes you feel that you together can solve any problem. I believe that this is crucial in the education process and in establishing a productive scientific environment such as the Scientific Computing Laboratory. However, this imposes many obligations on you as well, to do better, to work harder, to keep trying in order to achieve and exceed the excellence established by him.

Working on the thesis, I have been surrounded by very kind and helpful colleagues at the Institute of Physics Belgrade. Implementation of the algorithm has been done with the assistance of the PARADOX team, and I give thanks to them for their help in writing the codes, and usage of the PARADOX Supercomputing Facility. I would also like to express my gratitude to Dr. Axel Pelster from the Technical University of Kaiserslautern, Dr. Alexandru Nicolin from the University of Bucharest, and Dr. Sadhan Kumar Adhikari from the São Paulo State University for all the generous help and productive discussions.

Abstract

After pioneering experiments that realized Bose-Einstein condensates in systems of ultracold atoms with weak contact interactions, it took a decade for experimental techniques to advance and enable measurement of effects of the dipole-dipole interaction that exist between atoms or molecules with a permanent or induced electric or magnetic dipole moment. The first such experiment was realized in 2005 with chromium atoms, followed by the experiments with atoms with much larger magnetic moments, such as dysprosium and erbium. Furthermore, the dipolar condensates comprised of polar molecules with much stronger electrical or magnetic dipole moments were also realized. While the contact interaction is symmetric and has a short range, the dipole-dipole interaction between atoms or molecules is anisotropic and has a long range. These features are responsible for a whole series of new phenomena that appear in ultracold dipolar gases. If we take into account that the strength of the contact interactions can be varied over many orders of magnitude using the Feshbach resonance technique, and that the dipole-dipole interaction strength can also be tuned using a fast rotating magnetic or electric field, it is easy to see that such a versatility of dipolar quantum gases is unparalleled and makes them an obligatory element in a toolbox for engineering quantum devices and sensors.

The main contribution of this thesis is the study of Faraday and resonant density waves in ultracold bosonic systems with the contact and the dipole-dipole interaction. Such waves emerge in Bose-Einstein condensates as a result of the harmonic driving of the system. They represent nonlinear excitations and are generated due to the interaction-induced coupling of collective oscillation modes and the existence of parametric resonances. We introduce here a variational mean-field approach for the description of the dynamics of the Faraday and resonant waves in dipolar condensates. This approach is based on the Gaussian variational ansatz, which includes the condensate widths and the conjugated dynamical phases as parameters. The ansatz also includes the density modulations in order to capture the dynamics of density waves.

Using the developed variational approach, as well as a full numerical approach, we study in detail the properties of density waves in dipolar condensates at zero temperature, where breaking of the symmetry due to anisotropy of the dipole-dipole interaction plays an important role. We derive equations of motion for the dynamics of a driven dipolar system and identify the most unstable modes that correspond to the Faraday and resonant waves. Based on this, we derive the analytical expressions for spatial periods of both types of density waves as functions of the contact and the dipole-dipole interaction strength. We compare the obtained variational results with the results of extensive numerical simulations that solve the dipolar Gross-Pitaevskii equation in three dimensions, and find a very good agreement.

In this thesis, we also study the effects of the contact and the dipole-dipole interaction on the properties of the ground state and of the collective oscillation modes of dipolar condensates. While the increase of the contact interaction strength always leads to an increase of condensate widths, the situation is more complex when the dipole-dipole interaction is varied. In a cigar-shaped geometry, when the dipoles are oriented in the radial direction, the increase of the dipole-dipole interaction strength leads to the increase of condensate widths in the weak-confinement direction and in the direction of the dipoles, while the width in the third direction decreases. We also study the frequencies of the collective modes, where the interaction effects turn out to be less pronounced, in particular for the breathing and the quadrupole mode, whose values practically remain constant over the whole range of experimentally relevant values of both interaction strengths. The frequency of the radial-quadrupole mode is more sensitive to changes of interaction strengths, especially the contact interaction strength, and shows a nonmonotonous behavior as a function of the dipole-dipole interaction strength.

Keywords: Bose-Einstein condensate, pattern formation, dipole-dipole interaction, parametric resonance, interaction effects
Research field: Physics
Research subfield: Condensed matter physics
UDC number: 538.9

Резиме

Након пионирских експеримената са системима ултрахладних атома у којима је реализована Бозе-Ајнштајн кондензација са слабом контактном интеракцијом, била је потребна читава деценија да би се прецизност експеримената повећала и омогућила мерење ефеката дипол-дипол интеракције која постоји између атома или молекула са перманентним или индукованим електричним или магнетним диполним моментом. Први такав експеримент је изведен 2005. године са атомима хрома, а након тога су уследили експерименти са диспрозијумом и ербијумом, атомима са јаким магнетним диполним моментима, као и са поларним молекулима са далеко већим електричним и магнетним диполним моментима. Док је контактна интеракција симетрична и краткодометна, дипол-дипол интеракција између атома или молекула је анизотропна и дугодометна и узрок је читавог низа нових особина ултрахладних бозонских система. Ако узмемо у обзир да се у експериментима јачина контактне интеракције може мењати од јако одбојне до јако привлачне користећи технику Фешбах резонанци, као и то да се јачина дипол-дипол интеракције може контролисати помоћу брзо ротирајућег магнетног или електричног поља, лако је закључити да прилагодљивост и разноврсност особина диполних квантних гасова чини ове системе неупоредивим и обавезним алатом у инжењерингу квантних уређаја и сензора.

Главни допринос ове дисертације је проучавање феномена Фарадејевих и резонантних таласа густине у ултрахладним бозонским системима са контактном и дипол-дипол интеракцијом. Овакви таласи настају као резултат хармонијске модулације система и представљају нелинеарне ексцитације система услед присуства интеракција, спрезањем колективних осцилација и параметарских резонанци. У овој дисертацији смо у оквиру теорије средњег поља развили варијациони приступ за опис динамике Фарадејевих и резонантних таласа у диполним кондензатима. Овај приступ је заснован на Гаусовом варијационом анзацу који за параметре има ширине кондензата, конјуговане фазе, а укључује и модулације густине како би описао динамику таласа густине.

Користећи развијени варијациони приступ, као и пун нумерички приступ, детаљно смо проучавали особине таласа густине у диполним кондензатима на нултој температури, где дипол-дипол интеракција игра важну улогу због нарушења симетрије услед анизотропије система. Извели смо једначине кретања које описују динамику модулисаног диполног бозонског система и идентификовали најнестабилније моде које одговарају Фарадејевим и резонантним таласима. Даље, на основу тога, извели смо аналитичке изразе за просторне периоде оба типа таласа густине, као и њихову зависност од јачине контактне и дипол-дипол интеракције. Добијене варијационе резултате упоредили смо са резултатима детаљних нумеричких симулација које решавају диполну Грос-Питаевски једначину у три просторне димензије и добили смо веома добро слагање.

У овој дисертацији проучавали смо и утицај контактне и дипол-дипол интеракције на својства основног стања и колективних осцилација диполних кондензата. Док повећање јачине контактне интеракције увек доводи до ширења кондензата, ситуација је сложенија када се мења јачина дипол-дипол интеракције. За замку у облику цигаре у којој су диполи оријентисани у радијалном смеру, повећање јачине дипол-дипол интеракције доводи до ширења кондензата у лонгитудиналном правцу и у правцу поларизације, док се ширина у трећем правцу смањује. Поред тога, проучавали смо и фреквенције колективних мода, где су ефекти интеракција мање изражени. Ово се посебно односи на монополну (дишућу) и квадруполну моду, чије вредности практично остају константне у целом распону експериментално релевантних вредности јачина интеракција. Са друге стране, фреквенција радијалне квадруполне моде је осетљивија на промену јачине интеракције, посебно јачине контактне интеракције, док при промени јачине дипол-дипол интеракције показује немонотоно понашање.

Кључне речи: Бозе-Ајнштајн кондензација, формирање патерна, дипол-дипол интеракција, параметарска резонанца, ефекти интеракције
Научна област: Физика
Ужа научна област: Физика кондензованог стања
УДК број: 538.9

Contents

List of figures

List of tables

1 Introduction

According to the quantum statistical physics, there is a critical temperature below which the weakly-interacting bosons populate the lowest energy state of the system, which becomes macroscopically occupied. For temperatures well below the critical one, the thermal excitations can be usually neglected, and the same applies to the quantum fluctuations. The emergence of a macroscopically occupied ground state represents one of the few macroscopic quantum phenomena and is known as the Bose-Einstein condensation. It was experimentally realized for the first time in 1995 in dilute ultracold atomic gases of alkali metals, such as lithium ^{7}Li [1], rubidium ^{87}Rb [2] and sodium ^{23}Na [3]. Theoretically, the Bose-Einstein condensate (BEC) as a new phase of matter was predicted in 1924 by Indian physicist Satyendra Nath Bose [4] and German physicist Albert Einstein [5]. The theoretical study of BECs and a long quest for its experimental realization has significantly contributed to the development of quantum statistical physics, condensed matter physics, atomic and molecular physics, quantum optics, and laser physics, as well as to the other areas of physics, such as quantum information, quantum field theory, high-energy physics, and even the theory of general relativity. Such a wide applicability stems from the fact that BECs represent almost ideal Feynman's quantum simulators [6] for many physical systems.

In typical experiments with BECs, an ultracold dilute atomic cloud has a number density between $10^{19} - 10^{21}\,\mathrm{m}^{-3}$, i.e., three to six orders of magnitude lower than the density of air at room temperature and atmospheric pressure. The system is usually confined in a magneto-optical trap that can be described by a harmonic

potential, which is experimentally realized by a six-beam laser setup, where two counter-propagating beams in each spatial direction provide harmonic confinement. Atoms of selected species are cooled down to the nanokelvin temperatures using a combination of different techniques, such as the Zeeman slower, the laser cooling, and the evaporative cooling. In order to experimentally realize a BEC in a system with weak inter-atomic interactions, it is essential that the gas is rarefied. If this is the case, the system is close to the ideal gas of bosons, and the standard Bogoliubov theory can be applied. In practice, the diluteness requirement can be expressed by the condition [7, 8]:

$$na_s^3 \ll 1\,, \tag{1.1}$$

where n is the number density and a_s is the s-wave scattering length of atoms, which characterizes atomic interactions, seen as scattering processes in a dilute gas. Figure 1.1 illustrates the experimentally measured momentum distribution of a sodium

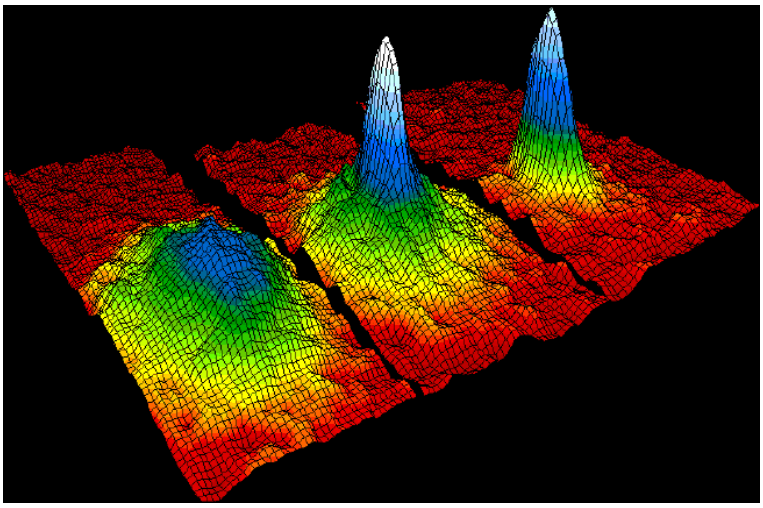

Figure 1.1: The first experimental realization of a BEC in 1995 in a dilute ultracold atomic gas of sodium ^{23}Na. The three momentum distributions at different temperatures illustrate how the condensation sets in: well above T_c we have the Maxwell-Boltzmann distribution (left); at T_c the peak corresponding to the macroscopic occupation of the ground state appears (middle); well below T_c the thermal cloud disappears and only the peak around $\mathbf{p} = 0$ remains (right). The figure is taken from Wikipedia and authored by NIST/JILA/CU-Boulder [NIST Image, public domain, https://commons.wikimedia.org/wiki/File:Bose_Einstein_condensate.png].

gas at three different temperatures. The distribution on the left-hand side corresponds to the thermal (Maxwell–Boltzmann) distribution at a temperature well above the critical one (T_c), while the distribution in the middle represents the results for the system at the critical temperature $T_c = 170\,\mathrm{nK}$. This distribution is bimodal, containing both the thermal component and a peak that corresponds to the emerging condensed fraction of atoms. The distribution on the right-hand side is obtained after an additional evaporative cooling brings the system down to the temperature $T = 20\,\mathrm{nK} \ll T_c$. Since the system is now significantly below the critical temperature, practically all atoms are in the condensate, and the experimental momentum distribution exhibits a single-peak distribution that corresponds just to the condensed fraction.

1.1 Role of interactions

Investigation of ultracold quantum gases is a very attractive research field that involves a large number of theoretical and experimental groups worldwide. Such a widespread interest comes from the fact that properties of the BEC systems can be broadly tuned in an unprecedented range. In particular, this applies to the strength of contact interactions that can be varied over many orders of magnitude using the Feshbach resonance [9] technique. The existence of Feshbach resonances is related to atomic bound states and can be practically manipulated by an external magnetic field, thus adjusting the electronic structure of atoms. In this way, close to a Feshbach resonance, the strength of the contact interaction can be dynamically tuned over a wide range of values. Furthermore, not only the amplitude, but also the sign of the interaction can be changed, i.e., the interaction can be tuned from very repulsive to very attractive.

After pioneering experiments that realized BEC in systems with weak contact interactions, it took a decade of work on accuracy improvement of experimental techniques to enable measurement of effects of the dipole-dipole interaction (DDI) that exists between atoms or molecules with a permanent or induced electrical or

magnetic dipole moment. The very first such experiment was realized in 2005 with chromium atoms ^{52}Cr [10], while the experiments with atoms with much larger magnetic moments, such as dysprosium ^{164}Dy [11] and erbium ^{168}Er [12] came after. Furthermore, the dipolar condensates comprised of ultracold polar molecules with much stronger electrical [13] and magnetic [14] dipole moment were realized some years ago. While the contact interaction is symmetric and has a short-range, the DDI between atoms or molecules is anisotropic and long-range. These features are responsible for a whole series of new phenomena that appear in ultracold dipolar gases [15]. For example, due to the attractive component of the DDI, an instability exists, and the system is stable only for a number of atoms below the critical one. This is closely related to the trap geometry, and if the system contains a number of particles larger than the critical one, it may still be quasi-stable or collapse. The stability of the system depends not only on the trap geometry, but also on its interplay with the orientation of the dipoles. Note that in experiments the dipoles are not randomly oriented, but usually follow a preferential direction, determined by an external magnetic or electric field. If the system becomes unstable due to changes in the geometry of the trap or due to a number of particles which is above the critical, it undergoes a dynamical collapse during which interesting structures appear [16–18].

Although quantum fluctuations can be usually neglected, close to stability border they may play a crucial role and lead to new states of matter, such as the quantum droplets that were recently observed in dipolar condensates of dysprosium [19, 20] and erbium [21]. In these recent experiments, it was observed that the Rosensweig instability [22] due to the DDI is compensated by the stabilizing effect of quantum fluctuations. Note that the quantum droplets, emerging from the partial condensate collapse, are arranged in a lattice that, under certain circumstances can behave as the elusive supersolid state of matter [23]. Another interesting feature of quantum droplets is that they can be considered to be made of an incompressible quantum liquid.

The strength of the DDI can be also tuned using a fast rotating magnetic or

electric field [24, 25]. Therefore, both the contact interaction and the DDI strength can be varied in experiments, and they represent the important parameters of the system. We also note that the dimensionality of the system can be tuned and considered as a free parameter. Namely, by manipulating the harmonic trap frequencies, the geometry of the system can be transformed from the three-dimensional to quasi-two-dimensional or quasi-one-dimensional. Furthermore, this can also be done dynamically, during the experiment, at the same time as possible changes of the contact interaction and the DDI. Due to all of these features, the versatility of dipolar quantum gases is unparalleled and makes them obligatory elements of a toolbox for engineering quantum devices and sensors.

1.2 Collective oscillation modes

The very first BEC experiments have focused on the measurement of frequencies of low-lying collective oscillations modes of the system [26, 27]. Until nowadays such experiments remain the most accurate, and the frequencies of the collective oscillations can be measured with the precision of few per mill. These experiments are also the most natural ones, since they measure the response of the system to small perturbations. In a typical experiment, the system is prepared such that it occupies the ground state for a given set of parameters and the trap geometry. Afterward, the system is excited by a small perturbation of one of the parameters, e.g., a small variation of one of the trap frequencies, or moving of the trap origin, or change of the interaction strength. Such a perturbation generates the dynamical response of the system, which can be measured by imaging of the density profile of the system. This is done by the time-of-flight imaging or using one of *in situ* techniques [7, 8], which allow to measure the time dependence of the BEC properties, such as a center of mass position, condensate widths, etc. The Fourier analysis of these time dependencies reveals frequencies of the low-lying collective modes, typically breathing, quadrupole, radial-quadrupole, and dipole mode.

However, this approach does not allow the specific collective modes to be iden-

tified with the corresponding frequencies. Only if we know how the system should be excited in order to induce only one of the modes, it is possible to measure its frequency. Even if this the case, BEC systems are nonlinear and different collective modes are coupled. Therefore, although initially only one mode could be excited, other collective modes will get excited over time through the transfer of energy. Only detailed theoretical modeling of the systems' dynamics allows us to identify the frequencies with the corresponding collective modes properly. One of the most conventional methods for this is the time-dependent variational approach. Usually, variational parameters include the condensate widths and their dynamics reveal not only the frequencies, but also the type of the collective modes. The variational approach leads to a set of nonlinear differential equations, which reflect the nonlinear nature of BECs. The analysis of these equations allows to calculate not only the collective oscillation modes, but also to study the dynamics of the system. This includes the response of the system to driving of one of the parameters and the emergence of parametric resonances.

From a theoretical point of view, a BEC is usually studied in the formalism of second quantization. The corresponding many-body Hamiltonian includes the two-body interactions between the particles, which are of two types: the short-range contact interaction and the long-range DDI. Since the interactions are usually weak, they can be treated perturbatively, and the mean-field theory gives a basic description of the system. At zero temperature, we can neglect thermal excitations, and the mean-field theory yields the Gross–Pitaevskii equation (GPE). For dipolar systems, the standard GPE has to be extended to include the corresponding dipolar interaction term. These equations, which are also called nonlinear Schrödinger equations, due to the presence of nonlinear interaction-induced terms, are capable of describing practically all phenomena that appear in BEC systems, with reasonable precision. In particular, the GPE can be used as a basis for the variational approach, as outlined above. However, if a more precise description of the system is necessary, a full numerical solution of the GPE may be required. Its analysis can also be used to calculate the frequencies of the collective modes. Since the frequencies of the collective modes are measured experimentally with high accuracy, they are used to

estimate the accuracy of all theoretical and numerical approaches for the modeling of BECs. While the variational and other theoretical approaches enable the derivation of functional dependencies of the collective mode frequencies on the system's parameters, it is clear that their accuracy is limited by the selection of the variational ansatz and by the approximation order in a perturbation expansion. On the other hand, a full numerical approach is much more accurate. It allows direct solving of the mean-field theory equations, or higher-order theories, but requires a numerical simulation for each given set of parameters. Only a combination of analytical and numerical approaches, and a comparison with experimental results, provide us with full description and understanding of the system in a comprehensive way.

In addition to well-known low-lying excitation modes mentioned previously, due to nonlinearity in ultracold quantum gases some other types of excitations can emerge as well. Density waves are an important example of nonlinear excitations and can be induced by a harmonic modulation of the trap frequencies or interaction strength. The motivation for this comes from the classical phenomenon of Faraday waves, which may appear on the surface of the shallow layer of liquid under certain conditions. Namely, if the container with the liquid is harmonically oscillated in a vertical direction, the wave patterns may emerge, depending on the ratio of the liquid depth and the container size, as well as depending on the modulation frequency. This phenomenon was first studied and described by Michael Faraday at the beginning of the XIX century [28]. The interest for such type of excitations arose again during the 1980s in the context of nonlinear liquids. In the context of ultracold gases, Faraday waves were first investigated theoretically in 2002 by Staliunas [29]. After his first theoretical and numerical results for the systems with contact interaction where he assumed that the interaction strength is harmonically modulated, the Faraday waves were first measured in the BEC experiments with rubidium atoms in 2007 by Engels [30]. In the experiment, the radial part of the harmonic trap was modulated instead of interaction strength. However, qualitatively this leads to the same type of density waves. Although in the case of nonlinear liquids the generated waves are surface waves, in the literature the same name, i.e., Faraday waves is also used for the density waves that emerge as a result of the harmonic modulation in

the realm of ultracold quantum gases.

Faraday waves in ultracold gases are a consequence of the existence of parametric resonances in the system. While the spatial period of these waves depends on the geometry of the system and other parameters, the frequency of their oscillations is constant and is two times smaller than the modulation frequency. This is characteristic of all parametric resonant phenomena, and in the variational approach leads to the Mathieu-like differential equation that gives the observed ratio of the frequency of Faraday waves and the modulation. The Faraday density waves with half of the modulation frequency, are not the only nonlinear excitation of the system. In a driven system, there are always excitations corresponding to waves that have the same frequency as the modulation. However, they become resonant when the modulation frequency corresponds to one of the collective mode frequencies, or their linear combination, or a multiple. The resonant waves develop in the system and grow exponentially, much faster than the Faraday waves. Therefore, these two phenomena can be easily distinguished, not only by comparing their frequencies, but also the corresponding onset times. So far, Faraday and resonant waves have been studied in a single [29] and binary BEC systems [31], both with spatially homogeneous and inhomogeneous contact interactions [32].

1.3 This thesis

The focus of this thesis is on the study of excitation modes of dipolar Bose-Einstein condensates, including the collective oscillation modes, and density waves that emerge as a result of the driving of the system. In particular, the thesis investigates the Faraday waves and effects of the contact and dipole-dipole interaction.

Chapter 1 gives an introduction into the field of ultracold atoms and important role that interactions play for the properties of Bose-Einstein condensates. It also introduces collective oscillation modes, Faraday and resonant waves, and discusses the theoretical approaches used for their description.

Chapter 2 describes in detail noninteracting Bose gases at zero temperature, and presents a mean-field theory for weakly interacting Bose systems with the short-range contact and the long-range dipole-dipole interaction. This chapter also presents a variational approach for the description of static and dynamic properties of dipolar BECs.

Ground-state properties of dipolar condensates are explored in Chapter 3. Using the variational approach introduced in Chapter 2, the corresponding equations for the ground state are derived, including the special cases of cylindrical symmetry, and pure contact interaction. The variational results are compared with full numerical results obtained by solving the three-dimensional dipolar GPE for three atomic species that posses the magnetic dipolar moments: chromium, erbium, and dysprosium.

Chapter 4 provides a variational description of the collective oscillation modes and derives the expressions for their frequencies as functions of the contact and dipole-dipole interaction strength, which are then verified by comparison with the full numerical results.

The Faraday and resonant waves are studied in Chapter 5. At first, a variational approach is developed, that is capable of capturing the emergence and dynamics of density waves in dipolar condensates. Using the properties of Mathieu's differential equation, the most unstable modes are identified and the expressions for the spatial periods of Faraday and resonant waves are derived. The phenomenon of density waves is then studied numerically in detail for the three atomic species and the obtained results are compared with the variational ones [33].

Chapter 6 presents details on the algorithm we use to solve the dipolar GPE and the split-step semi-implicit Crank-Nicolson method. Finally, Chapter 7 summarizes all results and gathers our conclusions. Appendices A – F present further analytical and numerical details that are relevant for certain chapters, but would overburden the main text.

2 Bose-Einstein condensation and dipole-dipole interaction

BEC is usually described in the formalism of second quantization [7,8]. First, using this formalism we will show that the macroscopic occupation of the ground state leads to the spatial coherence in the condensate, i.e., to the off-diagonal long-range order (ODLRO). The system is described in terms of the one-body density matrix, which can be defined in the coordinate space by

$$\rho(\mathbf{r},\mathbf{r}') = \langle \hat{\Psi}^\dagger(\mathbf{r})\, \hat{\Psi}(\mathbf{r}') \rangle \,, \tag{2.1}$$

where $\hat{\Psi}^\dagger(\mathbf{r})$ is a creation operator and $\hat{\Psi}(\mathbf{r})$ is the corresponding annihilation operator, and the averaging is performed over the ensemble. These operators describe a creation or annihilation of a particle at the position $\mathbf{r}$, and, in the case of bosons, satisfy the bosonic commutation relations

$$[\hat{\Psi}(\mathbf{r}) \,, \hat{\Psi}^\dagger(\mathbf{r}')] = \delta(\mathbf{r}-\mathbf{r}') \,, \quad [\hat{\Psi}(\mathbf{r}) \,, \hat{\Psi}(\mathbf{r}')] = 0 \,, \quad [\hat{\Psi}^\dagger(\mathbf{r}) \,, \hat{\Psi}^\dagger(\mathbf{r}')] = 0 \,. \tag{2.2}$$

For the system consisting of N identical bosons in a pure state, which is described by the N-body wave function $\Psi_n(\mathbf{r}_1,\ldots,\mathbf{r}_N)$, the one-body density matrix can be written as an integral

$$\rho_n(\mathbf{r},\mathbf{r}') = N \int d\mathbf{r}_2 \cdots d\mathbf{r}_N \, \Psi_n^*(\mathbf{r},\mathbf{r}_2,\ldots,\mathbf{r}_N)\, \Psi_n(\mathbf{r}',\mathbf{r}_2,\ldots,\mathbf{r}_N) \,, \tag{2.3}$$

which motivates the name of the matrix ρ. In a more general case, for a system in a mixed state in thermodynamic equilibrium, the one-body density matrix is calculated as an ensemble average, where the weights are given by the Boltzmann

distribution

$$\rho(\mathbf{r},\mathbf{r}') = \frac{1}{Z}\sum_n e^{-\beta E_n}\,\rho_n(\mathbf{r},\mathbf{r}')\,, \tag{2.4}$$

where n enumerates system's eigenstates Ψ_n, $\beta = 1/(k_B T)$ is the inverse temperature, and $Z = \sum_n e^{-\beta E_n}$ is the partition function. The diagonal elements of the density matrix correspond to the particle density

$$\rho(\mathbf{r},\mathbf{r}) = \langle \hat{\Psi}^\dagger(\mathbf{r})\,\hat{\Psi}(\mathbf{r})\rangle = n(\mathbf{r})\,, \tag{2.5}$$

and the total number of particles can be calculated as $N = \int d\mathbf{r}\, n(\mathbf{r}) \equiv \int d\mathbf{r}\,\rho(\mathbf{r},\mathbf{r})$.

Similarly, the one-body density matrix can be represented in the momentum space

$$\rho(\mathbf{p},\mathbf{p}') = \langle \hat{\Psi}^\dagger(\mathbf{p})\,\hat{\Psi}(\mathbf{p}')\rangle\,, \tag{2.6}$$

where the field operator in momentum space can be obtained from the coordinate representation by a Fourier transform

$$\hat{\Psi}(\mathbf{p}) = \frac{1}{(2\pi\hbar)^{3/2}}\int d\mathbf{r}\, e^{-\frac{i}{\hbar}\mathbf{p}\cdot\mathbf{r}}\,\hat{\Psi}(\mathbf{r})\,. \tag{2.7}$$

Again, the diagonal elements give the density of the particles, this time in momentum space, $n(\mathbf{p}) = \rho(\mathbf{p},\mathbf{p})$, and the total number of particles can be calculated in a similar manner, $N = \int d\mathbf{p}\, n(\mathbf{p})$. In a Bose-Einstein-condensed system, we have a macroscopic occupation of the ground state, which means that the particle density in momentum space has a form

$$n(\mathbf{p}) = N_0\,\delta(\mathbf{p}) + \tilde{n}(\mathbf{p})\,, \tag{2.8}$$

where the occupation $N_0/N \lesssim 1$. Let us see what consequences this has for the density matrix. If we insert equation (2.7) into equation (2.6) for $\mathbf{p} = \mathbf{p}'$, we get

$$n(\mathbf{p}) = \frac{1}{(2\pi\hbar)^3}\int d\mathbf{R}\, d\mathbf{s}\,\rho\left(\mathbf{R}+\frac{\mathbf{s}}{2},\mathbf{R}-\frac{\mathbf{s}}{2}\right)\,e^{\frac{i}{\hbar}\mathbf{p}\cdot\mathbf{s}}\,. \tag{2.9}$$

where $\mathbf{R}$ represents center-of-mass coordinate, and $\mathbf{s}$ the distance between the two arguments in density matrix. For a uniform and isotropic system of volume V, where we assume that in the thermodynamic limit $N, V \to \infty$ the particle density is constant $n = N/V$, the one-body density matrix depends only on the distance

s, and not on the center-of-mass coordinate $\mathbf{R}$, i.e., $\rho\left(\mathbf{R}+\mathbf{s}/2, \mathbf{R}-\mathbf{s}/2\right) = \rho(s)$. Therefore, the above equation for the density yields

$$\rho(s) = \frac{1}{V}\int d\mathbf{p}\, n(\mathbf{p})\, e^{-\frac{i}{\hbar}\mathbf{p}\cdot\mathbf{s}}\,. \tag{2.10}$$

For a normal system with a smooth momentum distribution $n(\mathbf{p})$ at small momenta, the one-body density vanishes in the limit $s \to \infty$, due to oscillatory nature of the phase factor $e^{-\frac{i}{\hbar}\mathbf{p}\cdot\mathbf{s}}$. However, the condensed system, which contains a delta function at $\mathbf{p} = 0$ gives a surprising result that $\rho(s) \to N_0/N$ when $s \to \infty$. The fact that off-diagonal elements of the one-body density matrix do not vanish even in the limit $s \to \infty$, shows that the existence of the condensate leads to coherence in the system, i.e., the long-range order.

To study excitations of the system, we use eigenstates of the density matrix $\varphi_i(\mathbf{r})$, where we assume, for simplicity, that the spectrum is discrete. In this basis, the density matrix is expressed as

$$\rho(\mathbf{r}, \mathbf{r}') = N_0\varphi_0^*(\mathbf{r})\varphi_0(\mathbf{r}') + \sum_{i>0} N_i\varphi_i^*(\mathbf{r})\varphi_i(\mathbf{r}')\,. \tag{2.11}$$

Here φ_0 represents the single-particle state with the occupancy N_0, while N_i are occupancies of excited states. Note that the above equation leads to expression (2.8) for the density $n(\mathbf{p})$ using equation (2.9) and orthonormality of the eigenstates $\varphi_i(\mathbf{r})$. For a uniform system of non-interacting bosons, the eigenstates are plane waves $\varphi_{\mathbf{p}}(\mathbf{r}) = e^{i\mathbf{p}\cdot\mathbf{r}/\hbar}/\sqrt{V}$, while in a general case the functions φ_i have to be determined by solving the corresponding eigenproblem. Using this basis, the field operator can be expressed as

$$\hat{\Psi}(\mathbf{r}) = \sum_i \varphi_i\hat{a}_i\,. \tag{2.12}$$

where new bosonic operators $\hat{a}_i$ represent elementary excitations of the system and obey bosonic commutation relations

$$[\hat{a}_i\,, \hat{a}_j^\dagger] = \delta_{ij}\,, \quad [\hat{a}_i\,, \hat{a}_j] = 0\,, \quad [\hat{a}_i^\dagger\,, \hat{a}_j^\dagger] = 0\,. \tag{2.13}$$

If the system is well below the critical temperature for Bose-Einstein condensation, we can use a zero-temperature approximation and neglect thermal excitations. We

can also assume that practically all of the particles are in the ground state and that only a small fraction is excited, which corresponds to the following decomposition of the field operator

$$\hat{\Psi}(\mathbf{r}) = \Psi_0(\mathbf{r}) + \delta\hat{\Psi}(\mathbf{r})\,, \tag{2.14}$$

where $\Psi_0(\mathbf{r}) \equiv \varphi_0(\mathbf{r})\,\hat{a}_0 \approx \sqrt{N_0}\,\varphi_0$ is the wave function of the condensate and $\delta\hat{\Psi}(\mathbf{r}) = \sum_{i\neq 0}\varphi_i(\mathbf{r})\,\hat{a}_i$ represents excitations due to quantum fluctuation. Note that the ground-state operators $\hat{a}_0$ and $\hat{a}_0^\dagger$ can be replaced by a c-number $\sqrt{N_0}$ due to macroscopic occupation of the ground state, and the fact that Bose-Einstein condensation corresponds to breaking of the $U(1)$ symmetry associated with the phase of the wave function [8]. In other words, below the critical temperature the order parameter does not vanish,

$$\langle\hat{a}_0\rangle = \langle\hat{a}_0^\dagger\rangle = \sqrt{N_0} \neq 0\,. \tag{2.15}$$

The time evolution of the system is determined by $e^{-i\hat{H}t/\hbar}$, where $\hat{H}$ is the Hamiltonian of the system, so the evolution of the ground-state wave function of the condensate is given by

$$\Psi_0(\mathbf{r},t) = \Psi_0(\mathbf{r})e^{-i\mu t/\hbar}\,, \tag{2.16}$$

where

$$\mu = E(N_0) - E(N_0-1) = \frac{\partial E}{\partial N}\Big|_{N=N_0} \tag{2.17}$$

is the system's chemical potential.

2.1 Noninteracting Bose gas

Previously we have neglected the thermal excitations and have used the zero-temperature approximation. However, depending on the temperature, we may have to take into account thermal excitations. For a uniform noninteracting Bose gas in a box of volume V, the eigenstates are plain waves that satisfy the periodic boundary conditions and have a dispersion relation $\epsilon(\mathbf{p}) = p^2/2m$. According to the Bose-Einstein distribution function, the number of atoms in thermal (excited) states is

given by

$$N_{\rm th}(T) = \sum_{\mathbf{p}\neq 0} \frac{1}{e^{\beta(p^2/2m-\mu)}-1}\,, \tag{2.18}$$

where m is the mass of an atom. Using a semi-classical approximation and replacing the above sum with the integral, $\sum_{\mathbf{p}} \to V/(2\pi\hbar)^3 \int d\mathbf{p}$, we obtain

$$N_{\rm th}(T) = \frac{V}{\lambda_T^3}\frac{2}{\sqrt{\pi}}\int_0^\infty \frac{x^{1/2}\,dx}{e^{-\beta\mu}\,e^x-1} = \frac{V}{\lambda_T^3}\,g_{3/2}(e^{\beta\mu})\,, \tag{2.19}$$

where $\lambda_T = \sqrt{2\pi\hbar^2\beta/m}$ is the thermal wavelength and $g_p(z) = \sum_{l=1}^{\infty} z^l/l^p$ is Bose function. From the above equation we obtain the critical temperature T_c at which all atoms are in the thermal population, i.e., $N_{\rm th}(T_c) = N$. This leads to

$$k_B T_c = \frac{2\pi\hbar^2}{m}\left(\frac{n}{g_{3/2}(1)}\right)^{2/3}\,, \tag{2.20}$$

where $n = N/V$ is the density of the gas and $g_{3/2}(1) \approx 2.612$. Note that the chemical potential of a uniform system above the critical temperature can be taken to be zero due to the dispersion relation, such that $e^{\beta\mu} = 1$. Above the critical temperate all particles are in the thermal cloud, and we have $N = V g_{3/2}(1)/\lambda_{T_c}^3$, according to equation (2.19). On the other hand, below T_c the number of thermal atoms decreases, and we have $N_{\rm th}(T) = (T/T_c)^{3/2}N$, which is obtained by combining equations (2.19) and (2.20). Therefore, the number of particles in the condensate is given by

$$N_0(T) = N\left[1-\left(\frac{T}{T_c}\right)^{3/2}\right]\,, \tag{2.21}$$

and becomes macroscopic for $T < T_c$.

The situation changes in the presence of an external trapping potential. The most frequently encountered and experimentally used potential is a harmonic trap, given by

$$U(x,y,z) = \frac{m}{2}(\omega_x^2 x^2 + \omega_y^2 y^2 + \omega_z^2 z^2)\,, \tag{2.22}$$

where ω_i, $i \in \{x,y,z\}$, are the trapping frequencies. The temperature dependence of the number of atoms in the condensate is now different and reads

$$N_0(T) = N\left[1-\left(\frac{T}{T_c}\right)^{3}\right]\,. \tag{2.23}$$

This is illustrated in Figure 2.1, where the blue line represents the condensate fraction for a homogeneous system, and red line the condensate fraction in the presence of an external harmonic trap. Not only that temperature dependence is modified by the presence of the trap, but also the critical temperature changes, and is now defined as

$$k_B T_c = \hbar\omega \left(\frac{N}{\zeta(3)} \right)^{1/3}, \tag{2.24}$$

where $\omega = (\omega_x \omega_y \omega_z)^{1/3}$ is the geometric average of the trap frequencies, and $\zeta(3) = g_3(1) \approx 0.94$. Note that the energy scale for the critical temperature is now given by the trap energy $\hbar\omega$, and that T_c now depends on the number of particles as $N^{1/3}$, while for the uniform case it was $N^{2/3}$.

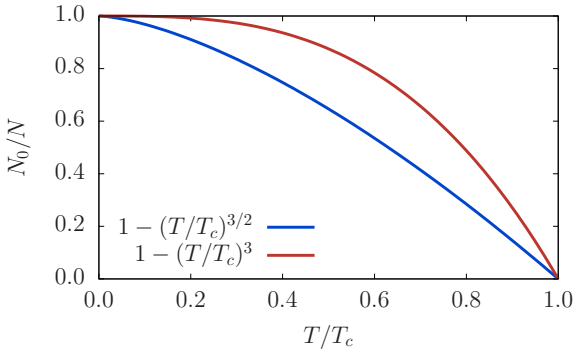

Figure 2.1: The condensate fraction N_0/N as a function of the temperature T/T_c for a noninteracting Bose gas: homogeneous case (blue line) and harmonically trapped case (red line).

2.2 Weakly-interacting Bose gas

The ground-state energy of an ideal Bose gas is equal to zero, this leads to zero pressure and infinite compressibility. However, the presence of interactions in the system, even the weak ones, dramatically changes this. Here we briefly outline the Bogoliubov theory to first order in the interaction strength, which is capable of describing a dilute Bose-Einstein-condensed gas. Precisely such systems were experimentally realized, and it was shown that only two-particle interactions significantly contribute to the energy of the systems, while interactions of three and more particles can be neglected. Also, due to large inter-particle distances, the details of the

two-body interactions can be neglected as well, i.e., they can be modeled just as s-wave scattering processes in a dilute Bose gas, described by the s-wave scattering length. The many-body Hamiltonian of such a system is given by

$$\hat{H} = \frac{\hbar^2}{2m} \int d\mathbf{r}\, \nabla\hat{\Psi}^\dagger(\mathbf{r}) \nabla\hat{\Psi}(\mathbf{r}) + \frac{1}{2} \int d\mathbf{r}\, d\mathbf{r}'\, \hat{\Psi}^\dagger(\mathbf{r}) \hat{\Psi}^\dagger(\mathbf{r}') U_c(\mathbf{r}-\mathbf{r}') \hat{\Psi}(\mathbf{r}') \hat{\Psi}(\mathbf{r})\,, \quad (2.25)$$

where $U_c(\mathbf{r})$ represents the model potential for the above-described contact interactions. The field operator in the case of a uniform gas and in the basis of plane waves reads $\hat{\Psi}(\mathbf{r}) = \sum_{\mathbf{p}} \hat{a}_{\mathbf{p}} e^{i\mathbf{p}\cdot\mathbf{r}/\hbar}/\sqrt{V}$, where $\hat{a}_{\mathbf{p}}$ is the operator annihilating a particle in the state with momentum $\mathbf{p}$. Inserting this into the above Hamiltonian, we obtain

$$\hat{H} = \sum_{\mathbf{p}} \frac{p^2}{2m} \hat{a}^\dagger_{\mathbf{p}} \hat{a}_{\mathbf{p}} + \frac{1}{2V} \sum_{\mathbf{q},\mathbf{p_1},\mathbf{p_2}} U_c(\mathbf{q})\, \hat{a}^\dagger_{\mathbf{p_1}+\mathbf{q}} \hat{a}^\dagger_{\mathbf{p_2}-\mathbf{q}} \hat{a}_{\mathbf{p_1}} \hat{a}_{\mathbf{p_2}}\,, \quad (2.26)$$

where $\mathbf{p_1}$ and $\mathbf{p_2}$ denote momenta of the interacting particles before the collision, $\mathbf{q}$ the exchanged momentum in the collision, while $U_c(\mathbf{q}) = \int U_c(\mathbf{r})\, e^{-i\,\mathbf{q}\cdot\mathbf{r}/\hbar} d\mathbf{r}$ is a Fourier transform of the interaction potential. For the temperatures below the critical one, the main contribution of the interaction to the Hamiltonian is due to the particles with small momenta, $\mathbf{q} \approx 0$. If we denote the zero-momentum component by $g \equiv U_c(\mathbf{q}=0)$, the Hamiltonian of the system can be rewritten as

$$\hat{H} = \sum_{\mathbf{p}} \frac{p^2}{2m} \hat{a}^\dagger_{\mathbf{p}} \hat{a}_{\mathbf{p}} + \frac{g}{2V} \sum_{\mathbf{p_1},\mathbf{p_2}} \hat{a}^\dagger_{\mathbf{p_1}} \hat{a}^\dagger_{\mathbf{p_2}} \hat{a}_{\mathbf{p_1}} \hat{a}_{\mathbf{p_2}}\,. \quad (2.27)$$

Note that the above approximation is mathematically equivalent to replacing the real inter-particle interaction potential with the modeled contact potential $U_c(\mathbf{r}-\mathbf{r}') = g\,\delta(\mathbf{r}-\mathbf{r}')$.

As we have seen, below the critical temperature the order parameter does not vanish and we can replace the operators $\hat{a}_0$ and $\hat{a}^\dagger_0$ by a c-number $\sqrt{N_0}$, where $N_0 = N$ at zero temperature, when all particles are condensed. If we restrict the sums in equation (2.27) to zero momentum contributions, which yield the ground state, we obtain for the ground-state energy

$$E_0 = \frac{gN^2}{2V} = \frac{1}{2} Nng\,. \quad (2.28)$$

The interaction coupling constant g can be expressed via s-wave scattering length a_s as $g = 4\pi\hbar^2 a_s/m$. Contrary to the noninteracting case, the pressure P of a condensed

weakly-interacting Bose gas does not vanish at zero temperature. Instead, it is given by $P = -\partial E_0/\partial V = gn^2/2$, and the compressibility is now finite, $\partial n/\partial P = 1/(gn)$. The compressibility is related to the speed of sound c by a relation $1/(mc^2) = \partial n/\partial P$. Using this, we can derive the sound velocity in the condensate and obtain $c = \sqrt{gn/m}$.

The above zeroth-order approximation is capable of providing us with the estimates for the ground-state energy, but not more than that. In order to describe the system in more detail, we have to go to the higher-order approximation such that we include the operators $\hat{a}_{\mathbf{p}}$ and $\hat{a}^\dagger_{\mathbf{p}}$ with $\mathbf{p} \neq 0$. The Hamiltonian does not contain the linear terms in $\hat{a}_{\mathbf{p}}$, and the first non-trivial approximation is quadratic,

$$\hat{H} = \frac{g}{2V}\,\hat{a}^\dagger_0\hat{a}^\dagger_0\hat{a}_0\hat{a}_0 + \sum_{\mathbf{p}} \frac{p^2}{2m}\,\hat{a}^\dagger_{\mathbf{p}}\hat{a}_{\mathbf{p}} + \frac{g}{2V}\sum_{\mathbf{p}\neq 0}\left(\hat{a}^\dagger_0\hat{a}^\dagger_{\mathbf{p}}\hat{a}_0\hat{a}_{\mathbf{p}} + \hat{a}^\dagger_{\mathbf{p}}\hat{a}^\dagger_{-\mathbf{p}}\hat{a}_0\hat{a}_0 + \hat{a}^\dagger_0\hat{a}^\dagger_0\hat{a}_{\mathbf{p}}\hat{a}_{-\mathbf{p}}\right). \tag{2.29}$$

Luckily, quadratic Hamiltonians can be explicitly diagonalized, which we do here following Bogoliubov prescription. As it was done in the zeroth-order approximation, in the terms in brackets of Equation (2.29) we replace the operators $\hat{a}_0$ and $\hat{a}^\dagger_0$ with $\sqrt{N}$, while for the first term we have to use a better approximation that is obtained from the normalization $\hat{a}^\dagger_0\hat{a}_0 + \sum_{\mathbf{p}\neq 0}\hat{a}^\dagger_{\mathbf{p}}\hat{a}_{\mathbf{p}} = N$, which leads to

$$\hat{a}^\dagger_0\hat{a}^\dagger_0\hat{a}_0\hat{a}_0 = N^2 - 2N\sum_{\mathbf{p}\neq 0}\hat{a}^\dagger_{\mathbf{p}}\hat{a}_{\mathbf{p}}\,, \tag{2.30}$$

up to terms quadratic in $\hat{a}_{\mathbf{p}}$. Note that the scattering theory [34], to the same approximation order, requires the renormalization of the interaction strength g

$$g \to g\left(1 + \frac{g}{V}\sum_{\mathbf{p}\neq 0}\frac{m}{p^2}\right). \tag{2.31}$$

By substituting Equations (2.30) and (2.31) into the Hamiltonian (2.29), we obtain

$$\hat{H} = g\frac{N^2}{2V} + \sum_{\mathbf{p}}\frac{p^2}{2m}\hat{a}^\dagger_{\mathbf{p}}\hat{a}_{\mathbf{p}} + \frac{1}{2}gn\sum_{\mathbf{p}\neq 0}\left(2\hat{a}^\dagger_{\mathbf{p}}\hat{a}_{\mathbf{p}} + \hat{a}^\dagger_{\mathbf{p}}\hat{a}^\dagger_{-\mathbf{p}} + \hat{a}_{\mathbf{p}}\hat{a}_{-\mathbf{p}} + \frac{mgn}{p^2}\right), \tag{2.32}$$

which can be diagonalized using the Bogoliubov transformation

$$\hat{a}_{\mathbf{p}} = u_{\mathbf{p}}\hat{b}_{\mathbf{p}} + v^*_{-\mathbf{p}}\hat{b}^\dagger_{-\mathbf{p}}\,, \quad \hat{a}^\dagger_{\mathbf{p}} = u^*_{\mathbf{p}}\hat{b}^\dagger_{\mathbf{p}} + v_{-\mathbf{p}}\hat{b}_{-\mathbf{p}}\,. \tag{2.33}$$

We require that new operators $\hat{b}_{\mathbf{p}}$ and $\hat{b}^{\dagger}_{\mathbf{p}}$ obey the same bosonic commutation relations as the operators $\hat{a}_{\mathbf{p}}$ and $\hat{a}^{\dagger}_{\mathbf{p}}$, which leads to the condition $|u_{\mathbf{p}}|^2 - |v_{-\mathbf{p}}|^2 = 1$. From this, we see that the coefficients u and v can be parametrized as follows

$$u_{\mathbf{p}} = \cosh \alpha_{\mathbf{p}} \,, \quad v_{-\mathbf{p}} = \sinh \alpha_{\mathbf{p}} \,. \tag{2.34}$$

In the above equation, the parameter $\alpha_{\mathbf{p}}$ has to be chosen such that non-diagonal elements of the Hamiltonian (2.32) vanish. For such $\alpha_{\mathbf{p}}$, the Hamiltonian becomes

$$\hat{H} = \tilde{E}_0 + \sum_{\mathbf{p}\neq 0} \epsilon(\mathbf{p})\, \hat{b}^{\dagger}_{\mathbf{p}} \hat{b}_{\mathbf{p}} \,, \tag{2.35}$$

where

$$\tilde{E}_0 = E_0 + \frac{1}{2} \sum_{\mathbf{p}\neq 0} \left[\epsilon(\mathbf{p}) - gn - \frac{p^2}{2m} + \frac{m(gn)^2}{p^2} \right] \,, \tag{2.36}$$

with $\epsilon(\mathbf{p})$ given by

$$\epsilon(\mathbf{p}) = \sqrt{\left(\frac{p^2}{2m} \right)^2 + c^2 p^2} \,, \tag{2.37}$$

which is known as the Bogoliubov dispersion law. Here c stands for the speed of sound $c = \sqrt{gn/m}$. The diagonalization of the system using the Bogoliubov transformation allows us to connect the system of interacting bosons with a noninteracting system of particles with the energy $\epsilon(\mathbf{p})$, whose annihilation and creation operators are $\hat{b}_{\mathbf{p}}$ and $\hat{b}^{\dagger}_{\mathbf{p}}$, respectively. Although this system is noninteracting, the dispersion is modified and is not given by a free particle expression $p^2/2m$. In the limit of small momenta $p \ll mc$, the dispersion (2.37) becomes $\epsilon(p) = cp$. From this, we see that elementary excitations of the system in the long-wavelength regime correspond to sound waves. From a symmetry point of view, these elementary excitations can be thought of as the Goldstone modes that correspond to breaking of the $U(1)$ symmetry of quantum mechanics due to the Bose-Einstein phase transition.

Note that the ground-state energy $\tilde{E}_0$ is given by

$$\tilde{E}_0 = E_0 \left(1 + \frac{128}{15\sqrt{\pi}} \sqrt{n a_s^3} \right) \,, \tag{2.38}$$

which is expressed in terms of the perturbation parameter na_s^3. Therefore, we see that the Bogoliubov theory is valid if the previously introduced criterion (1.1) is satisfied, such that the correction to the energy, given in brackets of Equation (2.38) is small.

2.3 Mean-field theory for dipolar Bose gas in a trap

Bose-Einstein condensation is experimentally realized with a dilute Bose gas trapped in the external potential. Such a setup produces a nonuniform system, which is experimentally necessary to provide confinement of the system. However, this changes the properties of the system and is responsible for new phenomena, such as collective oscillations. Here we briefly outline the mean-field theory for a nonuniform Bose gas in the external potential $U(\mathbf{r}, t)$, both for stationary and non-stationary systems. However, as outlined in Chapter 1, in this thesis, we consider not only the short-range contact interaction $U_c(\mathbf{r} - \mathbf{r}') = g\,\delta(\mathbf{r} - \mathbf{r}')$, but also the long-range dipole-dipole interaction

$$U_{\rm dd}(\mathbf{r}) = \frac{\mu_0}{4\pi}\,\frac{\mathbf{d}^2\mathbf{r}^2 - 3\,(\mathbf{r}\cdot\mathbf{d})^2}{r^5}\,, \tag{2.39}$$

where μ_0 is the vacuum permeability and $\mathbf{d}$ is the magnetic dipole moment. We assume that all dipoles are oriented in the same direction, as in experiments where, due to the present magnetic fields, this is always the case. If the dipoles are oriented in the z direction of the Cartesian coordinate system, the potential has the form

$$U_{\rm dd}(\mathbf{r}) = \frac{\mu_0\mu_{\rm d}^2}{4\pi}\,\frac{1 - 3\cos^2\theta}{r^3}\,, \tag{2.40}$$

where θ is the angle made by the vector $\mathbf{r}$ and the polarization direction z. The angle θ determines if DDI is attractive or repulsive. For instance, for $\theta = 0$ we have an attractive DDI, while for $\theta = \pi/2$ the interaction is repulsive, as illustrated in Figure 2.2. Note that the strength of the DDI is usually defined by the dipolar length

$$a_{\rm dd} = \frac{\mu_0\mu_{\rm d}^2 m}{12\pi\hbar^2}\,. \tag{2.41}$$

This is convenient since it allows us to express the DDI in a similar way as the contact interaction strength is expressed in terms of the s-wave scattering length.

With all these ingredients, the Hamiltonian of the system in the Heisenberg picture is given by

$$\begin{aligned}\hat{H} = \frac{\hbar^2}{2m}\int d\mathbf{r}\,\nabla\hat{\Psi}^\dagger(\mathbf{r},t)\,\nabla\hat{\Psi}(\mathbf{r},t) + \int d\mathbf{r}\,\hat{\Psi}^\dagger(\mathbf{r},t)\,U(\mathbf{r},t)\,\hat{\Psi}^\dagger(\mathbf{r}',t)\\ +\frac{1}{2}\int d\mathbf{r}\,d\mathbf{r}'\,\hat{\Psi}^\dagger(\mathbf{r},t)\hat{\Psi}^\dagger(\mathbf{r}',t)\,U_{\rm int}(\mathbf{r}-\mathbf{r}')\,\hat{\Psi}(\mathbf{r}',t)\hat{\Psi}(\mathbf{r},t)\,,\end{aligned} \tag{2.42}$$

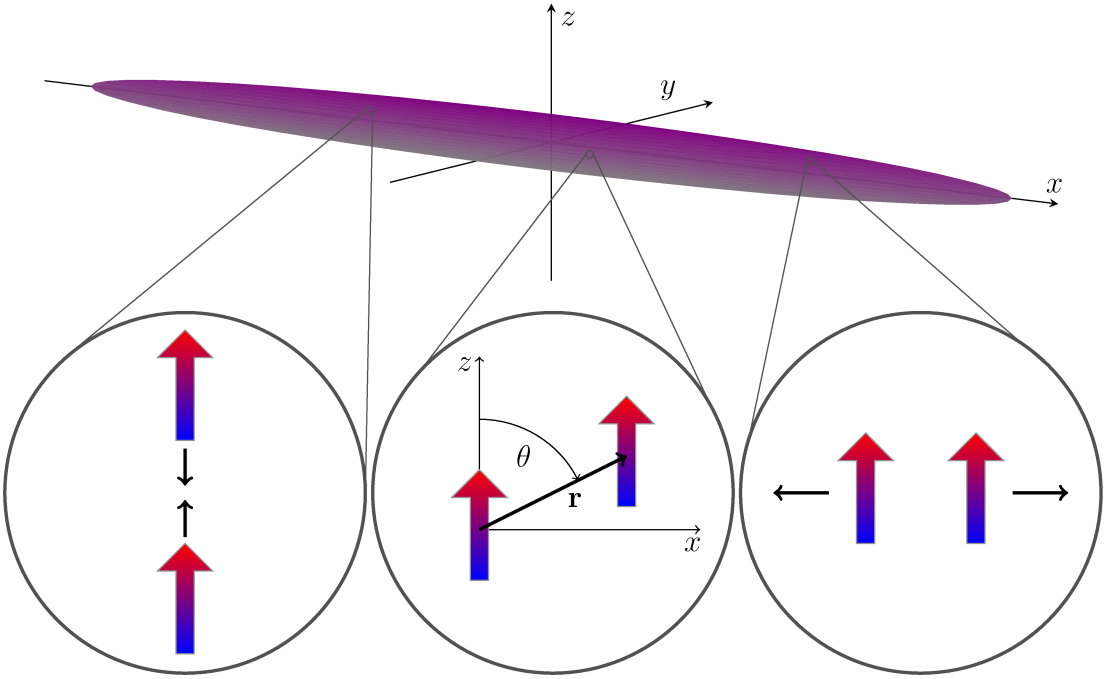

Figure 2.2: Illustration of dipole-dipole interactions of atoms whose dipole moments are polarized along the z axis. In the middle, we have a generic case determined by relative position between atoms $\mathbf{r}$ and angle between the polarization axis z and vector $\mathbf{r}$. On the left-hand side is a special case $\theta = 0$, which is usually called head-to-tail configuration, when the dipoles attract each other. On the right-hand side is another special case, corresponding to $\theta = \pi/2$, when the dipoles repel. This configuration is usually called side-by-side.

where $U_{\rm int}(\mathbf{r}) = U_{\rm c}(\mathbf{r}) + U_{\rm dd}(\mathbf{r})$. The dynamics of the system is governed by the Heisenberg equation

$$i\hbar \frac{\partial}{\partial t}\hat{\Psi}(\mathbf{r},t) = \left[\hat{\Psi}(\mathbf{r},t), \hat{H}\right] . \tag{2.43}$$

For the Hamiltonian (2.42), the above commutator can be readily calculated, and we obtain the equation of motion as follows

$$i\hbar \frac{\partial}{\partial t}\hat{\Psi}(\mathbf{r},t) = \left[-\frac{\hbar^2}{2m}\nabla^2 + U(\mathbf{r},t) + \int d\mathbf{r}'\, \hat{\Psi}^\dagger(\mathbf{r}',t)\, U_{\rm int}(\mathbf{r}-\mathbf{r}')\, \hat{\Psi}(\mathbf{r}',t)\right]\hat{\Psi}(\mathbf{r},t) . \tag{2.44}$$

The mean-field theory is obtained, according to (2.14), when we replace the field operator with the wave function of the condensate $\hat{\Psi}(\mathbf{r},t) = \psi(\mathbf{r},t)$ and neglect

quantum fluctuations, yielding the dipolar GPE in the form

$$i\hbar\frac{\partial}{\partial t}\psi(\mathbf{r},t) = \Bigg[-\frac{\hbar^2}{2m}\nabla^2 + U(\mathbf{r},t) + g|\psi(\mathbf{r},t)|^2 + \int d\mathbf{r}'\,\psi^*(\mathbf{r}',t)U_{\rm dd}(\mathbf{r}-\mathbf{r}',t)\psi(\mathbf{r}',t)\Bigg]\psi(\mathbf{r},t)\,. \tag{2.45}$$

The above equation is also called the nonlinear Schrödinger equation, where two types of nonlinearities are present due to the two types of interactions, namely the contact interaction and the DDI.

The dipolar GPE can be cast into a dimensionless form, which is useful for analytical and numerical considerations. This is done by choosing a reference frequency ω_r, and by expressing all other physical variables in units defined by it, i.e., lengths in units of harmonic oscillator length $l = \sqrt{\hbar/(m\omega_r)}$, time in units of $1/\omega_r$, and energy in units of $\hbar\omega_r$. This leads to dimensionless variables

$$\begin{aligned} &x \to \frac{x}{l}\,, \quad y \to \frac{y}{l}\,, \quad z \to \frac{z}{l}\,, \quad a_s \to \frac{a_s}{l}\,, \quad a_{\rm dd} \to \frac{a_{\rm dd}}{l}, \quad t \to \omega_r t\,, \\ &\psi(\mathbf{r},t) \to l^{3/2}\,\psi(\mathbf{r},t)\,, \quad U(\mathbf{r},t) \to \frac{1}{\hbar\omega_r}U(\mathbf{r},t)\,, \quad U_{\rm dd}(\mathbf{r},t) \to \frac{1}{\hbar\omega_r}U_{\rm dd}(\mathbf{r},t)\,. \end{aligned} \tag{2.46}$$

This rescales the harmonic trapping potential to the form

$$U(\mathbf{r},t) = \frac{1}{2}\left(\gamma^2x^2 + \nu^2y^2 + \lambda^2z^2\right)\,, \tag{2.47}$$

where $\gamma = \omega_x/\omega_r$, $\nu = \omega_y/\omega_r$, and $\lambda = \omega_z/\omega_r$ are the trap aspect ratios, which may be time-dependent. Taking all this into account, the dimensionless dipolar GPE reads

$$i\,\frac{\partial\psi(\mathbf{r},t)}{\partial t} = \Bigg[-\frac{1}{2}\nabla^2 + \frac{1}{2}\left(\gamma^2x^2 + \nu^2y^2 + \lambda^2z^2\right) + 4\pi N a_s\,|\psi(\mathbf{r},t)|^2 + 3Na_{\rm dd}\int d\mathbf{r}'\,\frac{1-3\cos^2\theta}{|\mathbf{r}-\mathbf{r}'|^3}\,|\psi(\mathbf{r}',t)|^2\Bigg]\psi(\mathbf{r},t)\,, \tag{2.48}$$

where θ is the angle between the vector $\mathbf{r}-\mathbf{r}'$ and z axis. The wave function here is normalized to unity $\int d\mathbf{r}\,|\psi(\mathbf{r},t)|^2 = 1$, and the density profile is given by $n(\mathbf{r},t) = N\,|\psi(\mathbf{r},t)|^2$. In the mean-field approximation, the many-body wave function can be written as

$$\Psi(\mathbf{r}_1,\ldots,\mathbf{r}_N,t) \approx \prod_{i=1}^{N}\frac{1}{\sqrt{N}}\,\psi(\mathbf{r}_i,t)\,. \tag{2.49}$$

The above time-dependent dipolar GPE describes the dynamics of the system. Since the ground state wave function has a common phase, it can be chosen to be zero, thus making the wave function real. The time-independent ground state wave function $\psi_0(\mathbf{r})$ satisfies the time-independent GPE, or the eigenequation

$$\begin{aligned}\mu\,\psi_0(\mathbf{r}) = \Bigg[-\frac{1}{2}\nabla^2 + \frac{1}{2}\left(\gamma^2x^2+\nu^2y^2+\lambda^2z^2\right) + 4\pi N a_s\left|\psi(\mathbf{r})\right|^2 \\ + 3Na_{\rm dd}\int d\mathbf{r}'\,\frac{1-3\cos^2\theta}{|\mathbf{r}-\mathbf{r}'|^3}\left|\psi(\mathbf{r}')\right|^2\Bigg]\psi(\mathbf{r})\,,\end{aligned} \tag{2.50}$$

where the chemical potential μ is the corresponding eigenvalue. Both the time-dependent and time-independent dipolar GPE can be exactly solved only numerically. In this thesis, we do so using the Crank-Nicolson split-step semi-implicit method [35–37]. From the analytic point of view, we use the variational approach, which is presented in the next section.

2.4 Variational approach

The dipolar GPE equation can be written as the Euler-Lagrange equation for the following Lagrangian density

$$\begin{aligned}\mathcal{L}(\psi,\psi^*) = \frac{i}{2}\left(\psi^*\dot{\psi}-\psi\dot{\psi}^*\right) + \frac{1}{2}\psi^*\nabla^2\psi - U\left|\psi\right|^2 - 2\pi N a_s\left|\psi\right|^4 \\ - \frac{3Na_{\rm dd}}{2}\left|\psi\right|^2\int d\mathbf{r}'\,\frac{1-3\cos^2\theta}{|\mathbf{r}-\mathbf{r}'|^3}\left|\psi(\mathbf{r}')\right|^2\,,\end{aligned} \tag{2.51}$$

where the wave function of the condensate is a function of space and time variables $\psi \equiv \psi(\mathbf{r},t)$, and the trap potential $U \equiv U(\mathbf{r},t)$ is given by Equation (2.47). The GPE (2.48) is obtained as the Euler-Lagrange equation with respect to ψ^*, or as the complex-conjugate of the Euler-Lagrange equation with respect to ψ. The above Lagrangian can be used as a starting point for a variational description of the ground state and the dynamics of a BEC. This is done by selecting a suitable ansatz for the wave function, calculating the Lagrangian of the system $L(t) = \int d\mathbf{r}\,\mathcal{L}$, and deriving the equations of motion for the variational parameters present in the wave function ansatz. The variational approach is a valuable method to study the behavior and properties of BECs and we use it to investigate the collective modes and density waves.

For the variational study, we use the Gaussian ansatz [38–41]

$$\psi(x,y,z,t) = \frac{1}{\pi^{3/4}\sqrt{u_x u_y u_z}}\, e^{-\frac{x^2}{2u_x^2}-\frac{y^2}{2u_y^2}-\frac{z^2}{2u_z^2}+ix^2\phi_x+iy^2\phi_y+iz^2\phi_z}\,, \tag{2.52}$$

where the six variational parameters $\{u_i, \phi_i\}$ are functions of time and represent the condensate widths and conjugated phases, respectively. If only the ground state is studied, then the phases ϕ_i can be omitted, and the condensate widths can be assumed to be constant. However, if we want to study the system's dynamics, then the phases are necessary, and therefore we take them into account. The coefficient in front of the exponent function is chosen so as to keep the wave function normalized to unity.

Using the Lagrangian density (2.51) and ansatz function (2.52), by integration we calculate Lagrangian of the system, consisting of five terms

$$L(t) = L_1(t) + L_2(t) + L_3(t) + L_4(t) + L_5(t)\,. \tag{2.53}$$

We calculate all term independently. The first one reads

$$L_1(t) = \frac{i}{2}\int d\mathbf{r}\,\left(\psi^*\dot{\psi} - \psi\dot{\psi}^*\right) = -\frac{1}{2}\left(u_x^2\dot{\phi}_x + u_y^2\dot{\phi}_y + u_z^2\dot{\phi}_z\right)\,, \tag{2.54}$$

while the kinetic energy term gives

$$L_2(t) = \frac{1}{2}\int d\mathbf{r}\,\psi^*\nabla^2\psi = -\frac{1}{4}\left(\frac{1}{u_x^2}+\frac{1}{u_y^2}+\frac{1}{u_z^2}+4u_x^2\phi_x^2+4u_y^2\phi_y^2+4u_z^2\phi_z^2\right)\,. \tag{2.55}$$

The term corresponding to the potential energy yield

$$L_3(t) = -\int d\mathbf{r}\,U\,|\psi|^2 = -\frac{1}{4}\left(\gamma^2u_x^2+\nu^2u_y^2+\lambda^2u_z^2\right)\,, \tag{2.56}$$

and the contact interaction term gives

$$L_4(t) = -2\pi N a_s\int d\mathbf{r}\,|\psi|^4 = -\frac{Na_s}{\sqrt{2\pi}\,u_x u_y u_z}\,. \tag{2.57}$$

The DDI term is more complex to calculate. It reads

$$L_5(t) = -\frac{3Na_{\rm dd}}{2}\int d\mathbf{r}\,|\psi(\mathbf{r})|^2\int d\mathbf{r}'\,U_{\rm dd}(\mathbf{r}-\mathbf{r}')\,|\psi(\mathbf{r}')|^2\,, \tag{2.58}$$

where, in the rescaled units, the dipolar potential is given by

$$U_{\rm dd}(\mathbf{r}) = \frac{1-3\cos^2\theta}{r^3}\,. \tag{2.59}$$

The $\mathbf{r}'$ integral can be calculated using the convolution theorem,

$$L_5(t) = -\frac{3Na_{\rm dd}}{2}\int d\mathbf{r}\,|\psi(\mathbf{r})|^2\,\mathcal{F}^{-1}\left\{\mathcal{F}\left[U_{\rm dd}\right](\mathbf{k})\,\mathcal{F}\left[|\psi|^2\right](\mathbf{k})\right\}(\mathbf{r})\,. \tag{2.60}$$

where $\mathcal{F}$ stands for the direct and $\mathcal{F}^{-1}$ for the inverse Fourier transform. The above expression can be further simplified if we explicitly write the inverse Fourier transform,

$$L_5(t) = -\frac{3Na_{\rm dd}}{2\,(2\pi)^3}\int d\mathbf{k}\,\mathcal{F}\left[U_{\rm dd}\right](\mathbf{k})\,\mathcal{F}\left[|\psi|^2\right](\mathbf{k})\int d\mathbf{r}\,|\psi(\mathbf{r})|^2\,e^{i\,\mathbf{k}\cdot\mathbf{r}}\,. \tag{2.61}$$

The last integral is equal to $\mathcal{F}\left[|\psi|^2\right]$, which can be readily calculated,

$$\mathcal{F}\left[|\psi|^2\right](\mathbf{k}) = e^{-\frac{1}{4}(k_x^2u_x^2+k_y^2u_y^2+k_z^2u_z^2)}\,. \tag{2.62}$$

The Fourier transform of the dipolar potential $\mathcal{F}\left[U_{\rm dd}\right](\mathbf{k})$ is calculated in Appendix A and reads

$$\mathcal{F}\left[U_{\rm dd}\right](\mathbf{k}) = \frac{4\pi}{3}\left(3\cos^2\theta - 1\right) = \frac{4\pi}{3}\left(\frac{3\,k_z^2}{k^2} - 1\right)\,. \tag{2.63}$$

If we put all these elements together, the DDI term of the Lagrangian is given by

$$L_5(t) = -\frac{3Na_{\rm dd}}{(2\pi)^2}\int d\mathbf{k}\,\left(3\,\frac{k_z^2}{k_z^2+k_y^2+k_z^2} - 1\right)e^{-\frac{1}{2}(k_x^2u_x^2+k_y^2u_y^2+k_z^2u_z^2)}\,, \tag{2.64}$$

and, as shown in Appendix B, can be expressed in terms of the anisotropy function f,

$$L_5(t) = \frac{Na_{\rm dd}}{\sqrt{2\pi}\,u_xu_yu_z}f\left(\frac{u_x}{u_z},\frac{u_y}{u_z}\right)\,. \tag{2.65}$$

The anisotropy function [42] is defined as

$$f(x,y) = -\frac{1}{4\pi}\int_0^{2\pi}d\varphi\int_0^{\pi}d\theta\,\sin\theta\left(\frac{3\,x^2y^2\cos^2\theta}{(x^2\sin^2\varphi + y^2\cos^2\varphi)\sin^2\theta + x^2y^2\cos^2\theta} - 1\right)\,, \tag{2.66}$$

and its solution can be expressed via elliptic integrals [43] of the first and the second kind. Details on the anisotropy function and how it can be expressed for different values of the arguments x and y are given in Appendix C. Now that we have calculated the Lagrangian of the system, we derive the Euler-Lagrange equations for the variational parameters,

$$\frac{d}{dt}\left(\frac{\partial L}{\partial\dot{q}_i}\right) - \frac{\partial L}{\partial q_i} = 0\,, \quad q_i \in \{u_x, u_y, u_z, \phi_x, \phi_y, \phi_z\}\,, \tag{2.67}$$

that describe the time evolution of the parameters. We first proceed with the equations for the phases ϕ_i, which turn out to be

$$\phi_i = \frac{\dot{u}_i}{2u_i}\,. \tag{2.68}$$

The Euler-Lagrange equations for the condensate widths u_i contain the phases ϕ_i and their derivatives, which can be eliminated using the above equations. This leads to the second-order differential equations for the parameters u_i in the form

$$\ddot{u}_x + \gamma^2 u_x - \frac{1}{u_x^3} - \sqrt{\frac{2}{\pi}}\frac{N}{u_x^2 u_y u_z}\left[a_s - a_{\mathrm{dd}} f\left(\frac{u_x}{u_z}, \frac{u_y}{u_z}\right) + a_{\mathrm{dd}}\frac{u_x}{u_z} f_1\left(\frac{u_x}{u_z}, \frac{u_y}{u_z}\right)\right] = 0 \tag{2.69}$$

$$\ddot{u}_y + \nu^2 u_y - \frac{1}{u_y^3} - \sqrt{\frac{2}{\pi}}\frac{N}{u_x u_y^2 u_z}\left[a_s - a_{\mathrm{dd}} f\left(\frac{u_x}{u_z}, \frac{u_y}{u_z}\right) + a_{\mathrm{dd}}\frac{u_y}{u_z} f_2\left(\frac{u_x}{u_z}, \frac{u_y}{u_z}\right)\right] = 0 \tag{2.70}$$

$$\begin{aligned}\ddot{u}_z + \lambda^2 u_z - \frac{1}{u_z^3} - \sqrt{\frac{2}{\pi}}\frac{N}{u_x u_y u_z^2}\Bigg[a_s - a_{\mathrm{dd}} f\left(\frac{u_x}{u_z}, \frac{u_y}{u_z}\right) - a_{\mathrm{dd}}\frac{u_x}{u_z} f_1\left(\frac{u_x}{u_z}, \frac{u_y}{u_z}\right) \\ - a_{\mathrm{dd}}\frac{u_y}{u_z} f_2\left(\frac{u_x}{u_z}, \frac{u_y}{u_z}\right)\Bigg] = 0\end{aligned} \tag{2.71}$$

where f_1 and f_2 are partial derivatives of the anisotropy function with respect to the first and the second argument. More details on these derivatives are given in Appendix C.

The above equations are used to variationally study the dipolar BEC dynamics, as well as the corresponding ground state. The algebraic equations determining the ground state are obtained by assuming that the condensate widths are constant, thus removing their second derivatives from the equations of motion.

3 Ground-state properties

In the previous section, we have seen that the condensation corresponds to the accumulation of a macroscopic number of particles in the ground state. In the mean-field theory at zero temperature, all atoms are condensed in the lowest single-particle quantum state, while the ground-state wave function $|\psi(\mathbf{r})|^2 = n(\mathbf{r})$ determines the density distribution of atoms. The wave function is a complex quantity, whose square of the modulus describes the contribution of the condensate to the diagonal elements of the density matrix ρ, and whose phase has a role in the coherence characterization. The wave function is defined up to a constant phase factor, reflecting the $U(1)$ symmetry of quantum mechanics. For a system with a time-independent Hamiltonian, the condensation leads to a symmetry breaking, such that the whole condensate is described by a constant phase, which can be set to zero. This can be also seen as a consequence of the off-diagonal long-range order discussed earlier. Since its phase can be set to zero, the wave function of the ground state can be always taken to be real-valued. In BEC experiments, the ground state usually represents the first step and is achieved by cooling an atomic or molecular sample using a variety of techniques. The ground state can be reliably described by the GPE [7,8], as discussed previously. In typical experiments, the dynamics of the system is induced from the ground state by perturbing the system or changing some of the system parameters, such as the interaction strength or the trap geometry. The behavior of the system is then observed using the time-of-flight imaging technique or *in-situ* types of measurements.

For a noninteracting system, the GPE reduces to a Schrödinger equation with a

given trap potential. In case of a harmonic potential (2.22), the ground state of a noninteracting bosonic system is determined by the lowest single-particle quantum state, which is given by the Gaussian function

$$\psi(x,y,z) = \left(\frac{m}{\pi\hbar}\right)^{3/4} (\omega_x\,\omega_y\,\omega_z)^{1/4}\, e^{-\frac{m}{2\hbar}(\omega_x x^2+\omega_y y^2+\omega_z z^2)}\,. \tag{3.1}$$

Therefore, in the weak-interaction limit a Gaussian function represents a good choice for a perturbative or variational treatment of the system. In the other limiting case, when the interaction is strong such that the kinetic energy term can be neglected, one can use the inverted parabola of the Thomas-Fermi approximation as a starting point for various analytic approaches.

3.1 Variational description of the ground state

To describe the ground state variationally, we rely on the Gaussian ansatz (2.52). In the static case, the dynamical equations of motion (2.69) - (2.71) have the following form

$$\gamma^2 u_x - \frac{1}{u_x^3} - \sqrt{\frac{2}{\pi}}\frac{Na_s}{u_x^2 u_y u_z} + \sqrt{\frac{2}{\pi}}\frac{Na_{\rm dd}}{u_x^2 u_y u_z} f\left(\frac{u_x}{u_z},\frac{u_y}{u_z}\right) - \sqrt{\frac{2}{\pi}}\frac{Na_{\rm dd}}{u_x u_y u_z^2} f_1\left(\frac{u_x}{u_z},\frac{u_y}{u_z}\right) = 0\,, \tag{3.2}$$

$$\nu^2 u_y - \frac{1}{u_y^3} - \sqrt{\frac{2}{\pi}}\frac{Na_s}{u_x u_y^2 u_z} + \sqrt{\frac{2}{\pi}}\frac{Na_{\rm dd}}{u_x u_y^2 u_z} f\left(\frac{u_x}{u_z},\frac{u_y}{u_z}\right) - \sqrt{\frac{2}{\pi}}\frac{Na_{\rm dd}}{u_x u_y u_z^2} f_2\left(\frac{u_x}{u_z},\frac{u_y}{u_z}\right) = 0\,, \tag{3.3}$$

$$\lambda^2 u_z - \frac{1}{u_z^3} - \sqrt{\frac{2}{\pi}}\frac{Na_s}{u_x u_y u_z^2} + \sqrt{\frac{2}{\pi}}\frac{Na_{\rm dd}}{u_x u_y u_z^2} f\left(\frac{u_x}{u_z},\frac{u_y}{u_z}\right) + \sqrt{\frac{2}{\pi}}\frac{Na_{\rm dd}}{u_y u_z^3} f_1\left(\frac{u_x}{u_z},\frac{u_y}{u_z}\right) + \sqrt{\frac{2}{\pi}}\frac{Na_{\rm dd}}{u_x u_z^3} f_2\left(\frac{u_x}{u_z},\frac{u_y}{u_z}\right) = 0\,. \tag{3.4}$$

The ground state of the system is characterized by the constant condensate widths u_i, $i \in \{x,y,z\}$. Solving the above system of nonlinear algebraic equations we directly obtain the widths of the condensate. In some special cases, this can be done analytically. For example, if we neglect the dipole-dipole interaction by setting $a_{\rm dd} = 0$, and if the system is cylindrically symmetric, such that $u_y = u_z = u_\rho$, the

variational equations reduce to

$$\gamma^2 u_x^4 = 1 + \sqrt{\frac{2}{\pi}} \frac{N a_s u_x}{u_\rho^2} \,, \tag{3.5}$$

$$u_\rho^4 = 1 + \sqrt{\frac{2}{\pi}} \frac{N a_s}{u_x} \,. \tag{3.6}$$

Because the number of atoms in the system is much larger than 1, the first term in the above equations can be neglected and the widths of the condensate can be expressed as

$$u_x \approx \left(\sqrt{\frac{2}{\pi}} \frac{N a_s}{\gamma^4} \right)^{1/5} , \quad u_\rho \approx \left(\sqrt{\frac{2}{\pi}} N a_s \gamma \right)^{1/5} . \tag{3.7}$$

As we can see, if we have only the contact interaction, the size of the condensate increases in all directions with the increase of the interaction strength as $a_s^{1/5}$. We also see that the condensate width u_x in the direction of weak confinement is always larger than u_ρ, since $u_x/u_\rho = 1/\gamma \gg 1$.

If we now take into account the dipole-dipole interaction, the system of equations (3.2) - (3.4) cannot be analytically solved anymore. However, it can be simplified when the direction of weak confinement matches the direction of the dipoles' polarization. Assuming cylindrical symmetry of the trap, the anisotropy function satisfies the following limit

$$\lim_{y \to x} x\, f_1(x, y) = \lim_{y \to x} y\, f_2(x, y) = \frac{(2 + x^2) f_s(x)}{2(1 - x^2)} - 1 \,, \tag{3.8}$$

where $f_s(x) = f(x, x)$ is the cylindrically symmetric anisotropy function which is defined in Appendix C. Using this the variational equations (3.2) - (3.4) lead to the system

$$\gamma^2 u_x^4 = 1 + \sqrt{\frac{2}{\pi}} \frac{N u_x}{u_\rho^2} \left[a_s - a_{\rm dd}\, A_x(\kappa) \right] , \tag{3.9}$$

$$u_\rho^4 = 1 + \sqrt{\frac{2}{\pi}} \frac{N}{u_x} \left[a_s - a_{\rm dd}\, A_\rho(\kappa) \right] , \tag{3.10}$$

where $\kappa = u_\rho/u_x$, while functions $A_x(\kappa)$ and $A_\rho(\kappa)$ are defined by

$$A_x(\kappa) = \frac{2 - 7\kappa^2 - 4\kappa^4 + 9\kappa^4\, d(\kappa)}{2\,(1 - \kappa^2)^2} \,, \tag{3.11}$$

$$A_\rho(\kappa) = \frac{1 + 10\kappa^2 - 9\kappa^2\, d(\kappa) - 2\kappa^4}{(1-\kappa^2)^2}\,, \tag{3.12}$$

with

$$d(\kappa) = \frac{\tanh^{-1}\sqrt{1-\kappa^2}}{\sqrt{1-\kappa^2}}\,. \tag{3.13}$$

In the limit of small κ, the above functions have limits $A_x(\kappa) \to 1$, $A_\rho(\kappa) \to 1$, with $\kappa^2 d(\kappa) \to 0$. If we again neglect the first term in Equations (3.9) and (3.10) due to $N \gg 1$, this system can be solved analytically in the zeroth-order in κ. The solutions are the same as (3.7), with a_s replaced by $\tilde{a}_s = a_s - a_{\rm dd}$. However, depending on the value of κ, the corrections of the order κ and higher could be important, such that the system (3.9) and (3.10) has to be solved without applying $\kappa \to 0$ approximation. In this case, the above equations cannot be solved analytically and the numerical approach is necessary. As we are considering a case when the dipoles are oriented in the z direction and the cylindrical symmetry is not present anymore, we have to use the full set of variational equations (3.2) - (3.4) in order to determine the ground state widths.

Note that the above equations for the ground state widths, with or without cylindrical symmetry, can be used to assess the stability of the system as well. Namely, we know that even in the absence of the dipole-dipole interaction the system can become unstable if the contact interaction is attractive ($a_s < 0$). This happens if the number of atoms is sufficiently large, such that the right-hand sides of equations (3.2) - (3.4) become negative. The situation is more complex in the presence of the dipole-dipole interaction, which is anisotropic and can lead to instability due to the trap geometry, even for a large and positive contact interaction. The numerical appearance of negative condensate widths can be used to detect the onset of instability in the solutions of the above equations.

3.2 Ground state of ^{52}Cr, ^{168}Er and ^{164}Dy BECs

Now we will explore how the ground state looks like for condensates of atomic chromium ^{52}Cr, erbium ^{168}Er, and dysprosium ^{164}Dy, using a numeric and a varia-

tional approach for the system which parameters are given in detail in Appendix D. As outlined in Chapter 6, the numerical calculation of the ground state relies on the imaginary-time propagation. As a starting point we always use a Gaussian wave function that corresponds to the noninteracting case (3.1), i.e., the variational ansatz (2.52) with $u_i = 1/\sqrt{\omega_i/\omega_r}$ and $\phi_i = 0$, given by Equation D.3. Starting from such a state, depending on how far from the ground state it is, the imaginary-time propagation evolves it exponentially fast to the ground state. Figure 3.1 shows the ground-state condensate density for $N = 10^4$ atoms of the considered atomic species, together with the chosen Gaussian initial state. We plot the corresponding integrated densities

$$n(x) = \iint dy\, dz\, |\psi(x,y,z)|^2\,, \tag{3.14}$$

$$n(y) = \iint dz\, dx\, |\psi(x,y,z)|^2\,, \tag{3.15}$$

$$n(z) = \iint dx\, dy\, |\psi(x,y,z)|^2\,, \tag{3.16}$$

where blue line represents the corresponding initial, Gaussian state density n_i, and red line the numerically obtained ground state density n_f. The trap weakly confines the atoms in the x direction, and therefore the condensate density $n_f(x)$ is much more elongated than the other two densities. This can be seen in Figure 3.1 for all species, with the corresponding width for ^{52}Cr of around 35.706 μm, while for ^{168}Er and ^{164}Dy the widths are around 23.201 μm and 23.339 μm, respectively. Here the widths w_i, $i \in \{x, y, z\}$ are defined as two times the root-mean-square of the corresponding coordinate, i.e., $2\sqrt{\langle x^2\rangle}$, $2\sqrt{\langle y^2\rangle}$, $2\sqrt{\langle z^2\rangle}$. Note that for the initial states we have $w_i = 2\,u_i = 2/\sqrt{\omega_i/\omega_r}$. The differences in the numerically obtained values of w_x are mainly the result of the contact interaction, i.e., a combination of the s-wave scattering lengths and masses of atoms. The values of a_s for all three species are quite similar, and therefore the main difference in the ground state widths comes from the mass difference, while the dipole-dipole effects are very small due to the small density $n(x)$. It is one order of magnitude smaller than the densities in other directions, as can be seen from Figure 3.1. However, the dipole-dipole interaction significantly changes the densities in the $y - z$ plane. Although the trap is cylindrically symmetric in that plane, the dipole-dipole interaction breaks

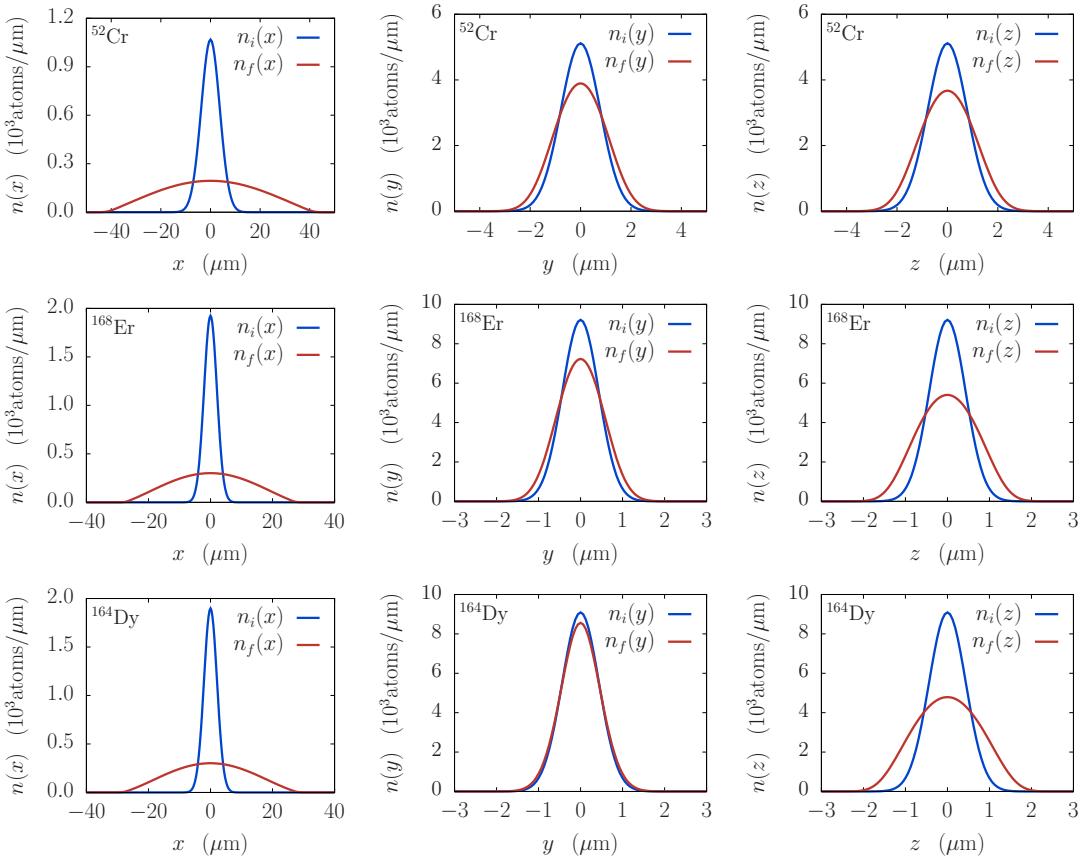

Figure 3.1: Integrated ground-state densities (red lines) of BEC of $N = 10^4$ atoms of chromium ^{52}Cr (first row), erbium ^{168}Er (second row), and dysprosium ^{164}Dy (third row). The initial Gaussian wave function that corresponds to the noninteracting case (blue) is propagated in the imaginary time for 100 ms to obtain the ground state (red line). The first, second, and third column give the corresponding integrated densities in x, y, and z direction, respectively. The observed significant elongation of the condensate in the x direction is due to the trap geometry defined in Appendix D.

this symmetry, which can be seen by comparing the middle and the right-hand side column in Figure 3.1.

In recent experiments it was demonstrated that the strength of the dipole-dipole interaction can be tuned by applying a fast-rotating magnetic field, or for electric dipoles, a fast-rotating electric field [24, 25]. In our description, this corresponds to changing the value of the parameter $a_{\rm dd}$. If we set $a_{\rm dd} = 0$, then the system is reduced to a BEC with only the contact interaction. Note that this can be effectively achieved if the external field that orders the dipoles is switched off. To compare how

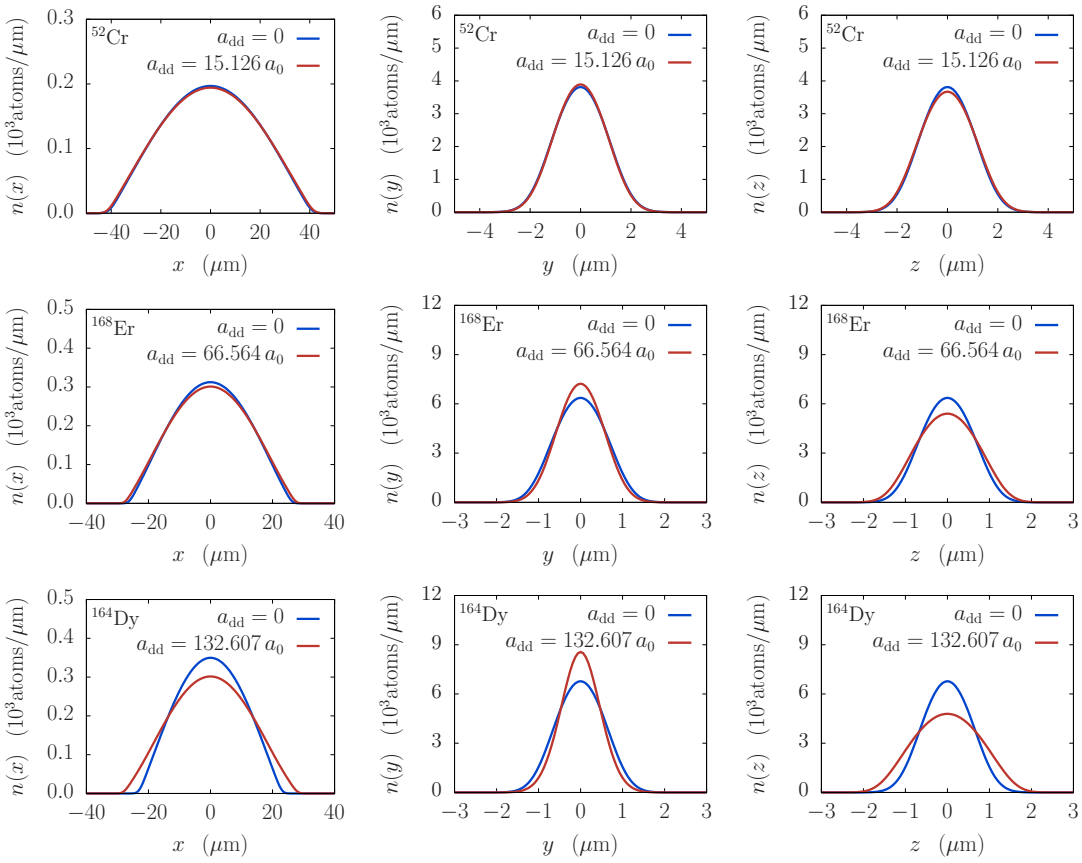

Figure 3.2: Integrated ground-state densities of BEC of $N = 10^4$ atoms of chromium ^{52}Cr (first row), erbium ^{168}Er (second row), and dysprosium ^{164}Dy (third row). Red lines correspond to the densities obtained by taking into account the dipole-dipole interaction, while blue lines are obtained for $a_{dd} = 0$. The first, second, and third column give the corresponding integrated densities in x, y, and z direction, respectively. Table 1 gives relative differences in the condensate widths due to dipolar effects.

the dipole-dipole interaction contributes to the ground state properties, Figure 3.2 gives the corresponding results for chromium ^{52}Cr (first row), erbium ^{168}Er (second row), and dysprosium ^{164}Dy (third row), with (red) and without (blue lines) the dipole-dipole interaction. As expected, the figure shows cylindrical symmetry in the $y-z$ plane when the dipolar effects are neglected, while the asymmetry grows when they are taken into account, from chromium to dysprosium, as the dipole moment increases. Table 1 gives relative differences of the condensate widths due to the dipole-dipole interaction, $\Delta w_i/w_i = 1 - w_i(0)/w_i(a_{dd})$. Positive values correspond

Table 1: Relative differences of the ground-state condensate widths due to the dipole-dipole interaction. The values correspond to the integrated densities from Figure 3.2 for a BEC of $N = 10^4$ atoms. The differences are calculated as $\Delta w_i/w_i = 1 - w_i(0)/w_i(a_{\mathrm{dd}})$, $i \in \{x, y, z\}$. A positive value represents an increase of the width, and negative the opposite.

Species	a_{dd} (a_0)	$\Delta w_x/w_x$ (%)	$\Delta w_y/w_y$ (%)	$\Delta w_z/w_z$ (%)
^{52}Cr	15.126	0.959	-1.055	2.044
^{168}Er	66.564	4.009	-10.987	13.469
^{164}Dy	132.607	3.624	-25.457	20.748

to the increase of the width due to dipolar effects, and negative values the opposite. As expected, the condensate elongates in the direction of the dipoles, while due to the interplay of geometry and interaction effects, its width increases in the x and decreases in the y direction. As noted earlier, the relative change in the x direction is negligible, while in other directions it is quite significant for species with large dipole moments.

As mentioned earlier, propagation in imaginary-time is used to calculate the true ground state of the system starting from any initial state (provided that it is not orthogonal to the ground state). The convergence to the ground state can be detected by the convergence of all physical quantities that describe the system, in

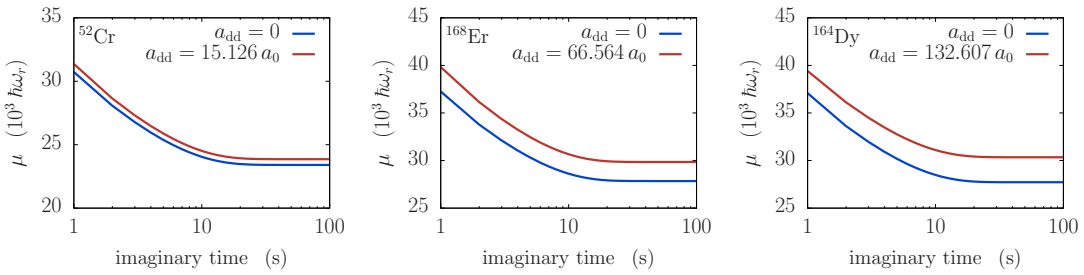

Figure 3.3: Convergence of the chemical potential of a BEC of $N = 10^4$ atoms of chromium ^{52}Cr (left), erbium ^{168}Er (middle), and dysprosium ^{164}Dy (right) during imaginary-time propagation, with (red) and without (blue line) the dipole-dipole interaction for the system parameters given in Appendix D.

particular, its chemical potential, energy, and the expectation value of the system's size. Therefore, the convergence of these quantities is used as a criterion in numerical simulations, which is illustrated in Figure 3.3. In the left panel we can see the decrease of the chemical potential for chromium ^{52}Cr, in the middle panel for erbium ^{168}Er, and in the right panel for dysprosium ^{164}Dy, both with and without dipole-dipole interaction. The chemical potential is expressed in units of $\hbar\omega_{\mathrm{r}}$, where $\omega_r = 160.5 \times 2\pi$ Hz is rescaling frequency. From Figure 3.3, we observe that the dipole-dipole interaction increases the energy of the system. Furthermore, this energy difference increases with the strength of the interaction a_{dd}, and reads $306\,\hbar\omega_{\mathrm{r}}$, $1444\,\hbar\omega_{\mathrm{r}}$, and $2101\,\hbar\omega_{\mathrm{r}}$, respectively for the listed atoms.

3.3 Interaction effects on the ground state

In this section, we study the influence of the short-range contact interaction on the ground state properties of dipolar condensates. For the first experimental realization of BEC, it was possible to tune the strength of contact interactions over a wide range using the Feshbach resonance technique [9]. By adjusting the external magnetic field close to a Feshbach resonance, the contact interaction strength can be tuned from large positive to large negative values, i.e., it is even possible to switch between repulsive and attractive interactions. To model this, we keep fixed the dipole-dipole interaction strength to experimentally measured values listed in Appendix D for each species, and investigate the ground state properties when the contact interaction parameter is varied in the interval from $a_s = 10\,a_0$ to $a_s = 200\,a_0$ for the condensate of $N = 10^4$ atoms. It turns out that erbium ^{168}Er BEC is unstable for low values of a_s, so we use the region from $a_s = 40\,a_0$ to $a_s = 200\,a_0$ in this case. Similarly, for dysprosium ^{164}Dy we use the interval from $a_s = 90\,a_0$ to $a_s = 200\,a_0$. Figure 3.4 illustrates the contact interaction strength dependence of the condensate widths in x, y, and z direction obtained from the numerical simulations (red) and variational calculation (blue line). As expected, the increase of the repulsive contact interaction leads to the increase of condensate widths in all directions. Results of numerical simulations agree with the results of the variational analysis with the relative error

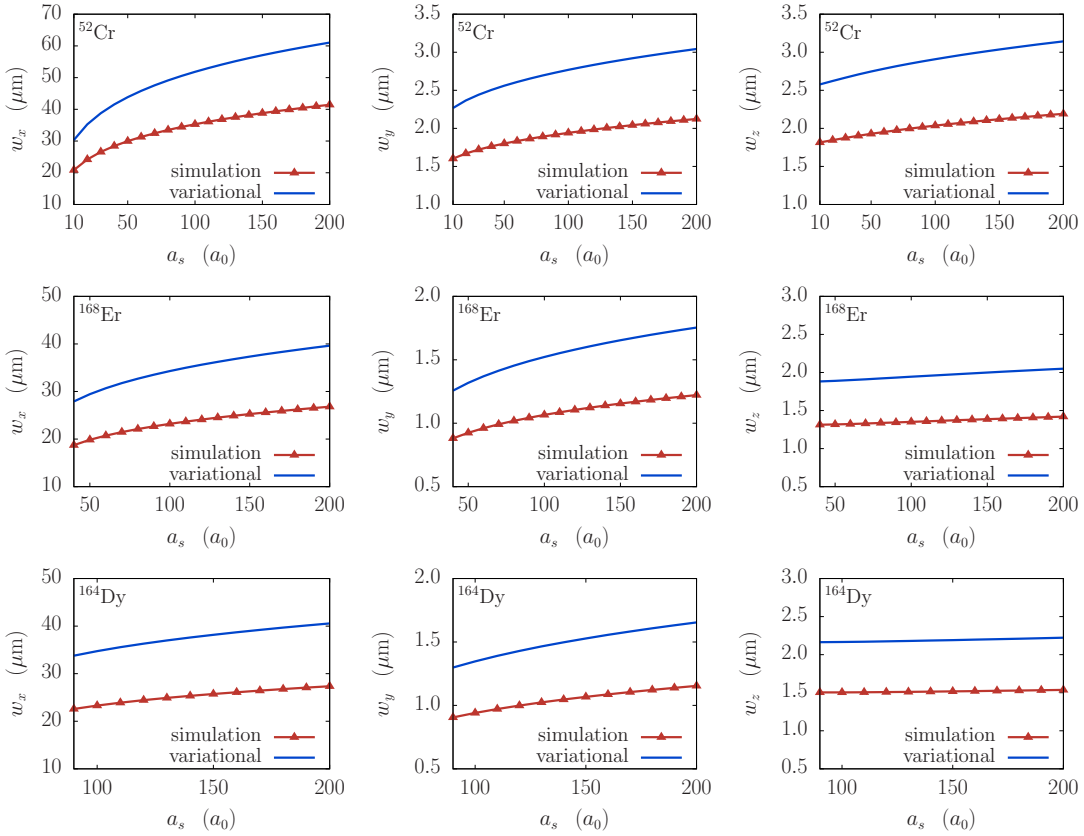

Figure 3.4: Condensate widths as functions of the contact interaction strength for a BEC of $N = 10^4$ atoms of chromium ^{52}Cr (first row), erbium ^{168}Er (second row), and dysprosium ^{164}Dy (third row). Results are obtained for fixed dipole-dipole interaction strengths given in Table 2. Red lines represent numerically obtained widths, and blue lines the variational ones.

of around 30%. As we can see from Table 2, which lists relative differences of the ground-state condensate widths for two values of the contact interaction strength, $a_s = 90\,a_0$ and $a_s = 200\,a_0$, the increase of the repulsive contact interaction increases the condensate width in all directions and for all species. We also observe that the dipole-dipole interaction suppresses elongation of the condensate in z direction, where it is attractive.

Although more difficult, it is also possible to tune-down the strength of the dipole-dipole interaction for magnetic atomic species using a fast-rotating magnetic field [24, 25]. The maximal possible values are defined by the permanent magnetic moment of the corresponding species. To investigate the effects of the dipole-dipole

Table 2: Relative differences of the ground-state condensate widths due to the contact interaction. The values correspond to the condensate widths from Figure 3.4 for a BEC of $N = 10^4$ atoms. The differences are calculated as $\Delta w_i/w_i = w_i(200\,a_0)/w_i(90\,a_0) - 1$, $i \in \{x, y, z\}$.

Species	a_{dd} (a_0)	$\Delta w_x/w_x$ (%)	$\Delta w_y/w_y$ (%)	$\Delta w_z/w_z$ (%)
^{52}Cr	15.126	16.917	9.748	7.957
^{168}Er	66.564	15.361	14.612	5.353
^{164}Dy	132.607	17.446	21.554	2.139

interaction on the ground-state properties, we numerically and variationally calculate the condensate widths of chromium ^{52}Cr, erbium ^{168}Er, and dysprosium ^{164}Dy in the interval from $a_{\mathrm{dd}} = 0\,a_0$ to $a_{\mathrm{dd}} = 170\,a_0$, keeping the contact interaction strength fixed. Due to the instability of erbium and dysprosium condensates for large values of a_{dd}, we have used the interval from $a_{\mathrm{dd}} = 0\,a_0$ to $a_{\mathrm{dd}} = 140\,a_0$ for those two species. Figure 3.5 illustrates the striking effect of the dipole-dipole interaction which has a non-monotonous behavior of the condensate width in x direction, causes a decrease in y direction and increase in z direction. The agreement between numerical and variational results as quite reasonable, with the error of around 30%. Table 3 gives relative differences of the ground-state condensate widths for $a_{\mathrm{dd}} = 0$ and $a_{\mathrm{dd}} = 100\,a_0$. As we see, the change is most prominent in y and z direc-

Table 3: Relative differences of the ground-state condensate widths due to the dipole-dipole interaction. The values correspond to the condensate widths from Figure 3.5 for a BEC of $N = 10^4$ atoms. The differences are calculated as $\Delta w_i/w_i = 1 - w_i(100\,a_0)/w_i(0)$, $i \in \{x, y, z\}$. A positive value represents an increase of the width, and negative the opposite.

Species	a_s (a_0)	$\Delta w_x/w_x$ (%)	$\Delta w_y/w_y$ (%)	$\Delta w_z/w_z$ (%)
^{52}Cr	105	5.004	-12.180	14.676
^{168}Er	100	4.290	-17.326	17.388
^{164}Dy	100	4.308	-17.205	17.336

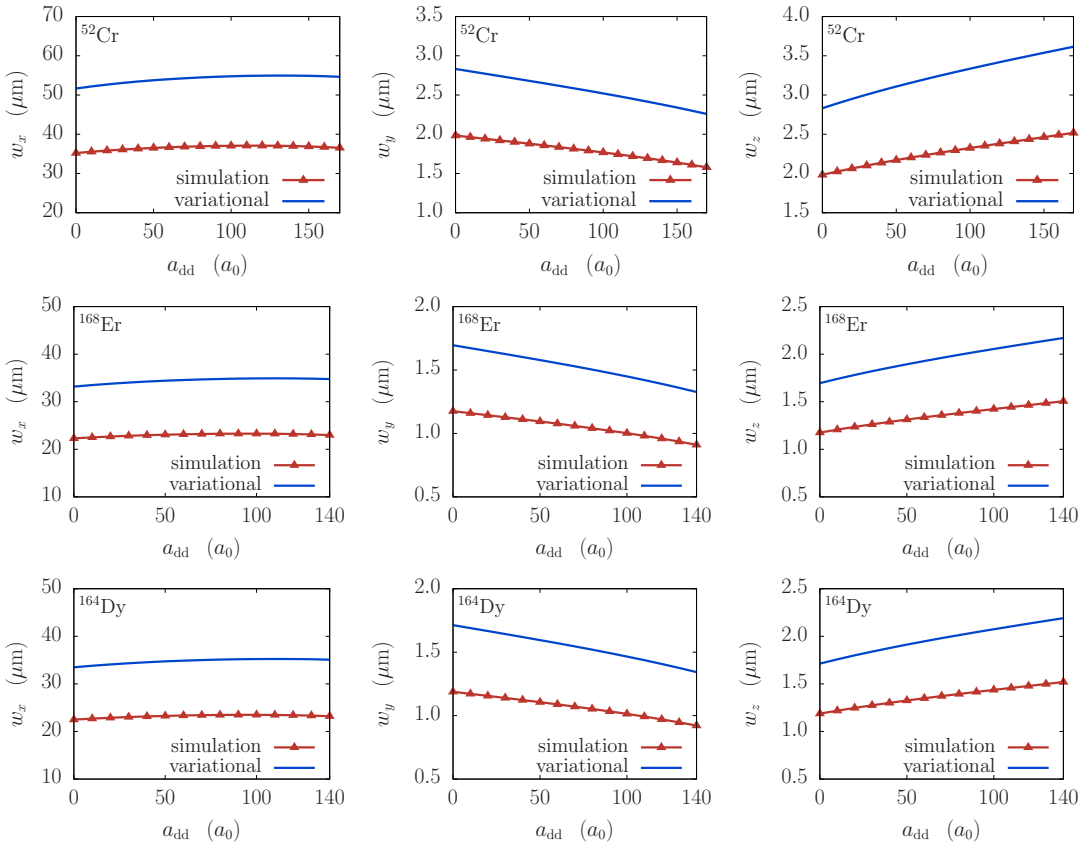

Figure 3.5: Condensate widths as functions of the dipole-dipole interaction strength for a BEC of $N = 10^4$ atoms of chromium ^{52}Cr (first row), erbium ^{168}Er (second row), and dysprosium ^{164}Dy (third row). Results are obtained for fixed contact interaction strengths given in Table 3. Red lines represent numerically obtained widths, and blue lines the variational ones.

tion. With an increase of the dipole-dipole interaction, the size of the condensate increases in z direction, and decreases in y direction. This is expected since it is well known that the condensate elongates along the direction of maximal attraction of the dipole-dipole interaction. On the other hand, the increase of the size in x direction is also observed but is much smaller.

4 Collective oscillation modes

Calculation of the system's ground state is usually the first step in analytical and numerical approaches. The same applies to the experimental studies, where obtaining and characterizing the ground state represents the first and necessary step before proceeding to further measurements. The characterization of the ground state includes measurement of its density profile and condensate widths, as we have seen in the previous section. In addition to these static properties, an important way to probe the system is to study its low-lying excitations or collective modes. Such excitations can be generated from the ground state by a small perturbation of the system's parameters. This results in small oscillations of the condensate density and its widths, which can be experimentally observed using the time-of-flight imaging or some of the *in-situ* techniques. The analysis of experimental results, as well as the results obtained in numerical simulations, includes the Fourier analysis of condensate widths, which yields the frequencies of the collective modes [44–46].

It is well known that the collective oscillation modes of a noninteracting Bose gas are disentangled, i.e., independent in each spatial direction, with the frequency equal to twice the corresponding trap frequency. The presence of interactions in the system couples different modes, which results in the appearance of the breathing mode, quadrupole mode, radial-quadrupole mode, dipole mode, etc. Their frequencies are shifted with respect to the noninteracting case, and the study of these interaction-induced frequency shifts represents one of the important characterization methods used to describe the ground-state properties. From the experimental point of view, probing of the collective excitations is one of the most accurate measurements that

can be performed in ultracold atom systems, with the precision of the order of one per mille. Therefore, a comparison of numerically or analytically obtained estimates for the frequencies of collective modes is an excellent method to check the validity and level of confidence of the models used. As in our case, there are two types of interaction in the system, and both of them independently affect the collective modes and their frequencies, which we study in this section.

In the case of externally driven systems, which is necessary to generate the density excitations, such as Faraday waves, one can expect the appearance of resonances in the system. This usually happens when the driving frequency is close to one of the frequencies of the collective modes, or their linear combination. In some cases, this leads to the emergence of the Faraday waves, while sometimes resonant waves appear, as we show in Chapter 5. Therefore, it is essential to understand well the collective modes of the system, to either avoid resonant behavior or to induce it when necessary.

4.1 Variational description of collective modes

For the variational study of the collective modes, we use the Gaussian variational ansatz (2.52), and equations of motion (2.69) - (2.71) derived in Section (2.4). The system is perturbed from the ground state by a small change of one of its parameters, such that the condensate widths become time-dependent,

$$u_i(t) = u_{i0} + \delta u_i(t)\,, \quad i \in \{x, y, z\}\,, \tag{4.1}$$

where u_{i0} are the constant ground-state widths, and $\delta u_i(t)$ are small oscillation amplitudes, $|\delta u_i(t)| \ll u_{i0}$. If we insert the expression (4.1) for the condensate widths into the equations of motion (2.69) - (2.71), and linearize the system by expanding it in the small parameters $\delta u_i(t)$ and keeping only the terms of the first order, we obtain a coupled system of ordinary linear differential equations of the second order, which can be expressed in the matrix form as

$$\delta\ddot{\mathbf{u}}(t) + M\,\delta\mathbf{u}(t) = 0\,. \tag{4.2}$$

Here $\delta\mathbf{u}(t)$ is a vector $[\delta u_x(t)\ \delta u_y(t)\ \delta u_z(t)]^T$, and elements of the matrix M are calculated from the Lagrangian of the system (2.53),

$$M_{ij} = -2\,\frac{\partial^2 L(\mathbf{u})}{\partial u_i\,\partial u_j}\bigg|_{\mathbf{u}=\mathbf{u_0}}\,, \quad i,j \in \{x,y,z\}\,. \tag{4.3}$$

To calculate the frequencies of the oscillations induced in the system, we write the solution of equation (4.2) in the following form

$$\delta\mathbf{u}(t) = \delta\mathbf{u}\,e^{i\omega t}\,, \tag{4.4}$$

where $\delta\mathbf{u}$ is a constant vector, and ω denotes a collective mode frequency. If we insert this into the matrix equation (4.2), the collective mode frequencies are eigenvalues of the matrix M, i.e., solution of the following eigenproblem

$$\det(M - \omega^2 I) = 0\,. \tag{4.5}$$

The above eigenproblem can be analytically solved in a simple way in some special cases. For example, if the system is cylindrically symmetric, such that $u_y = u_z \equiv u_\rho$, the problem is essentially two dimensional leading to additional symmetry in the matrix M, which now has the form

$$M = \begin{bmatrix} m_1 & m_4 & m_4 \\ m_4 & m_2 & m_3 \\ m_4 & m_3 & m_2 \end{bmatrix}\,. \tag{4.6}$$

Due to this, the corresponding eigenproblem can be fully solved in a closed form. The frequencies of the collective modes in this case are

$$\omega_B^2 = \frac{m_1 + m_2 + m_3 + \sqrt{(m_3 + m_2 - m_1)^2 + 8m_4^2}}{2}\,, \tag{4.7}$$

$$\omega_Q^2 = \frac{m_1 + m_2 + m_3 - \sqrt{(m_3 + m_2 - m_1)^2 + 8m_4^2}}{2}\,, \tag{4.8}$$

$$\omega_{RQ}^2 = m_2 - m_3\,, \tag{4.9}$$

with the corresponding eigenvectors

$$\mathbf{u}_B = \begin{bmatrix} \frac{m_1 - m_2 - m_3 + \sqrt{(m_3+m_2-m_1)^2+8m_4^2}}{2m_4} & 1 & 1 \end{bmatrix}^T\,, \tag{4.10}$$

$$\mathbf{u}_Q = \begin{bmatrix} \frac{m_1 - m_2 - m_3 - \sqrt{(m_3+m_2-m_1)^2+8m_4^2}}{2m_4} & 1 & 1 \end{bmatrix}^T\,, \tag{4.11}$$

$$\mathbf{u}_{RQ} = \frac{1}{\sqrt{2}}\begin{bmatrix} 0 & -1 & 1 \end{bmatrix}^T\,. \tag{4.12}$$

In the above expressions, index B denotes the breathing mode, Q the quadrupole mode and RQ the radial-quadrupole mode. The modes can be identified by analyzing the corresponding eigenvectors. In the first case, all three components of $\mathbf{u}_B$ are positive, which means that it corresponds to the breathing mode. In the second case, the longitudinal component of $\mathbf{u}_Q$ is of the opposite sign of the radial components, thus it represents the quadrupole mode, and in the third case, the longitudinal component of $\mathbf{u}_{RQ}$ is zero, while the two radial components are of the opposite sign, which means that this mode can be identified with the radial-quadrupole mode.

Next, we consider the system with contact interaction only. If we set $a_{\rm dd} = 0$, the derivatives (4.3) of Lagrangian (2.53) yield the following elements of matrix M

$$m_1 = \gamma^2 + \frac{3}{u_{x0}^4} + 2\sqrt{\frac{2}{\pi}}\frac{Na_s}{u_{x0}^3 u_{\rho 0}^2}\,, \tag{4.13}$$

$$m_2 = 1 + \frac{3}{u_{\rho 0}^4} + 2\sqrt{\frac{2}{\pi}}\frac{Na_s}{u_{x0} u_{\rho 0}^4}\,, \tag{4.14}$$

$$m_3 = \sqrt{\frac{2}{\pi}}\frac{Na_s}{u_{x0} u_{\rho 0}^4}\,, \tag{4.15}$$

$$m_4 = \sqrt{\frac{2}{\pi}}\frac{Na_s}{u_{x0}^2 u_{\rho 0}^3}\,, \tag{4.16}$$

where u_{i0}, $i \in \{x, \rho\}$ are the ground-state condensate widths given by equations (3.5) and (3.6). Using the above expressions in (4.7) - (4.9), we can calculate the frequencies of the collective modes as functions of the contact interaction strength a_s, the number of particles N, and the trap aspect ratio γ. For the noninteracting system, in the limit $a_s \to 0$, we obtain for the collective mode frequencies $\omega_B = 2$, $\omega_Q = 2\,\gamma$, and $\omega_{RQ} = 2$. These frequencies are given in dimensionless units, while the physical values are obtained by multiplying them with the referent frequency $\omega_r = \omega_y = \omega_z$, such that $\omega_B = 2\,\omega_r$, $\omega_Q = 2\,\omega_x$, and $\omega_{RQ} = 2\,\omega_r$. As mentioned earlier, in this special case we obtain the collective mode frequencies equal to twice the trap frequencies.

If the contact interaction is present in the system, then the collective mode frequencies depend on its strength a_s. Figure 4.1 shows this dependence, obtained from the variational approach for a BEC of $N = 10^4$ atoms of chromium ^{52}Cr, where the

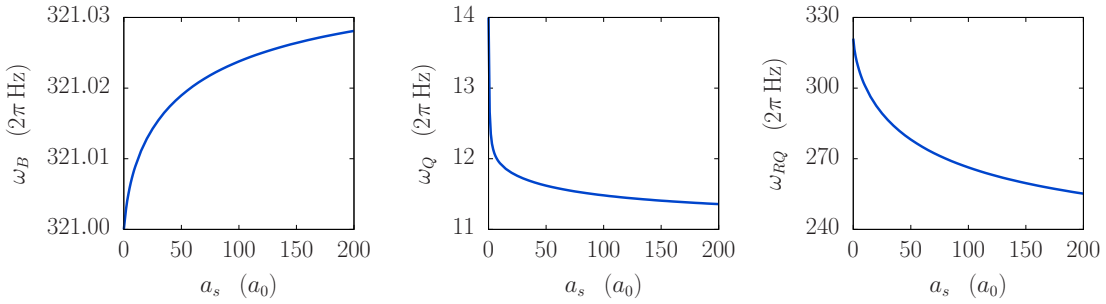

Figure 4.1: Frequencies of the breathing (left), quadrupole (middle), and radial-quadrupole (right) collective mode as functions of the contact interaction strength for a BEC of $N = 10^4$ atoms of chromium ^{52}Cr. Results are obtained using the variational approach, and neglecting the dipole-dipole interactions.

dipole-dipole interaction is neglected. As we can see, when the contact interaction parameter is varied in the interval from $a_s = 0$ to $a_s = 200\,a_0$, the frequency of the breathing mode slowly increases, while the frequency of the quadrupole mode slowly decreases. The decrease in the frequency of the radial-quadrupole mode is more prominent than in the case of the quadrupole mode. On this figure we also observe that in the noninteracting limit ω_B and ω_{RQ} tend to $321 \times 2\pi$ Hz $= 2 \times 160.5 \times 2\pi$ Hz, and that ω_Q tends to $14 \times 2\pi$ Hz $= 2 \times 7 \times 2\pi$ Hz.

In order to compare the variational results with experiments, we use the values obtained in Reference [44] for a BEC of $N = 1.5 \times 10^7$ atoms of ^{23}Na. For a trap with the frequencies $16.93(2) \times 2\pi$ Hz and $\omega_\rho = 230(20) \times 2\pi$ Hz, the experimentally measured value of the quadrupole mode frequency was $\omega_Q = 1.569(4)\,\omega_x$, which in excellent agreement with our variationally result $\omega_Q = 1.581\,\omega_x$. For the same parameters, the results of numerical simulations yield the frequency $\omega_Q = 1.575\,\omega_x$, which is in even better agreement with the experimental value. Therefore, we conclude that the above variational and numerical approach can be reliably applied to study ultracold atomic systems.

While it is still justified to neglect the dipole-dipole interaction for atomic species such as ^{52}Cr, for species with larger values of the dipole moment it is necessary to take it into account. We now present the variational calculation of the collective mode frequencies for the case of a cylindrically symmetric system with the dipoles

oriented in the direction of weak confinement. In this case, the elements of matrix M again have the form given by Equation (4.6). We have calculated the ground-state widths (3.9) and (3.10) for such a system in the previous section, which allows us to calculate the elements of matrix M as follows

$$m_1 = \gamma^2 + \frac{3}{u_{x0}^4} + 2\sqrt{\frac{2}{\pi}}\frac{N}{u_{x0}^3 u_{\rho 0}^2}\left(a_s - a_{dd}A_{xx}(\kappa)\right) , \tag{4.17}$$

$$m_2 = 1 + \frac{3}{u_{\rho 0}^4} + 2\sqrt{\frac{2}{\pi}}\frac{N}{u_{x0} u_{\rho 0}^4}\left(a_s - a_{dd}A_{\rho\rho}(\kappa)\right) , \tag{4.18}$$

$$m_3 = \sqrt{\frac{2}{\pi}}\frac{N}{u_{x0} u_{\rho 0}^4}\left(a_s - a_{dd}A_{x\rho}(\kappa)\right) , \tag{4.19}$$

$$m_4 = \sqrt{\frac{2}{\pi}}\frac{N}{u_{x0}^2 u_{\rho 0}^3}\left(a_s - a_{dd}A_{\rho x}(\kappa)\right) , \tag{4.20}$$

where $\kappa = u_{\rho 0}/u_{x0}$, and functions $A_{ij}(\kappa)$, $i, j \in \{x, \rho\}$ are defined by

$$A_{xx}(\kappa) = \frac{4\kappa^6 - 12\kappa^4 - 9\kappa^4 d(\kappa) + 51\kappa^2 - 36\kappa^2 d(\kappa) + 2}{2\left(1-\kappa^2\right)^3} , \tag{4.21}$$

$$A_{\rho\rho}(\kappa) = \frac{32\kappa^6 - 99\kappa^6 d(\kappa) + 141\kappa^4 - 36\kappa^4 d(\kappa) - 54\kappa^2 + 16}{16\left(1-\kappa^2\right)^3} , \tag{4.22}$$

$$A_{x\rho}(\kappa) = \frac{16\kappa^6 - 45\kappa^6\, d(\kappa) + 51\kappa^4 - 30\kappa^2 + 8}{8\left(1-\kappa^2\right)^3} , \tag{4.23}$$

$$A_{\rho x}(\kappa) = \frac{4\kappa^6 - 36\kappa^4 + 45\kappa^4\, d(\kappa) - 15\kappa^2 + 2}{2\left(1-\kappa^2\right)^3} , \tag{4.24}$$

with

$$d(\kappa) = \frac{\tanh^{-1}\sqrt{1-\kappa^2}}{\sqrt{1-\kappa^2}} . \tag{4.25}$$

During the calculation of the matrix elements (4.21) - (4.24), in addition to (3.8), we have used the following identities satisfied by the anisotropy function

$$\lim_{y\to x} f_{11}(x,y) = \lim_{y\to x} f_{22}(x,y) = \frac{9\left[\left(4+x^2\right) f_s(x) - 2\left(1-x^2\right)\right]}{8\left(1-x^2\right)^2} , \tag{4.26}$$

$$\lim_{y\to x} f_{12}(x,y) = \lim_{y\to x} f_{21}(x,y) = \frac{\left(8+8x^2-x^4\right) f_s(x) - 2\left(4-5x^2+x^4\right)}{8x^2\left(1-x^2\right)^2} , \tag{4.27}$$

where $f_s(x) \equiv f(x,x)$ is the cylindrically symmetric anisotropy function, and f_{ij} are second partial derivatives,

$$f_{ij}(x_1,x_2) = \frac{\partial^2}{\partial x_i\, \partial x_j} f(x_1,x_2) . \tag{4.28}$$

In the limit of small κ, which corresponds to the cigar-shaped trap geometry that we consider ($\gamma \ll 1$), the above functions can be approximated in the zeroth

order by $A_{xx}(\kappa) = A_{\rho\rho}(\kappa) = A_{x\rho}(\kappa) = A_{\rho x}(\kappa) \to 1$, with $\kappa^2 d(\kappa) \to 0$. In this approximation, the matrix elements can be cast in the same form as Equations (4.13) - (4.16), just with a_s replaced by $\tilde{a}_s = a_s - a_{\rm dd}$. The corresponding collective mode frequencies are given again by Equations (4.7) - (4.9), which are evaluated using the above-approximated values of m_i.

We now consider the experimentally relevant system when the dipoles are oriented in the z direction, such that the cylindrical symmetry is not present anymore, although the trap remains cylindrically symmetric. In this case, the matrix M is just a symmetric matrix, without the additional symmetry we had before. After a lengthy, but straightforward calculation, we obtain

$$M_{11} = \gamma^2 + \frac{3}{u_{x0}^4} + 2\sqrt{\frac{2}{\pi}}\frac{N}{u_{x0}^3 u_{y0} u_{z0}}\left[a_s - a_{\rm dd}\left(f - \kappa_{xz} f_1 + \frac{\kappa_{xz}^2}{2} f_{11}\right)\right], \tag{4.29}$$

$$M_{22} = 1 + \frac{3}{u_{y0}^4} + 2\sqrt{\frac{2}{\pi}}\frac{N}{u_{x0} u_{y0}^3 u_{z0}}\left[a_s - a_{\rm dd}\left(f - \kappa_{yz} f_2 + \frac{\kappa_{yz}^2}{2} f_{22}\right)\right], \tag{4.30}$$

$$M_{33} = 1 + \frac{3}{u_{z0}^4} + 2\sqrt{\frac{2}{\pi}}\frac{N}{u_{x0} u_{y0} u_{z0}^3}\Big[a_s - a_{\rm dd}\Big(f + 2\kappa_{xz} f_1 + 2\kappa_{yz} f_2 + \tag{4.31}$$

$$\kappa_{xz}\kappa_{yz} f_{12} + \frac{\kappa_{xz}^2}{2} f_{11} + \frac{\kappa_{yz}^2}{2} f_{22}\Big)\Big], \tag{4.32}$$

$$M_{12} = \sqrt{\frac{2}{\pi}}\frac{N}{u_{x0}^2 u_{y0}^2 u_{z0}}\left[a_s - a_{\rm dd}\left(f - \kappa_{xz} f_1 - \kappa_{yz} f_2 + \kappa_{xz}\kappa_{yz} f_{12}\right)\right], \tag{4.33}$$

$$M_{13} = \sqrt{\frac{2}{\pi}}\frac{N}{u_{x0}^2 u_{y0} u_{z0}^2}\left[a_s - a_{\rm dd}\left(f - \kappa_{xz} f_1 + \kappa_{yz} f_2 - \kappa_{xz}\kappa_{yz} f_{12} - \kappa_{xz}^2 f_{11}\right)\right], \tag{4.34}$$

$$M_{23} = \sqrt{\frac{2}{\pi}}\frac{N}{u_{x0} u_{y0}^2 u_{z0}^2}\left[a_s - a_{\rm dd}\left(f + \kappa_{xz} f_1 - \kappa_{yz} f_2 - \kappa_{xz}\kappa_{yz} f_{12} - \kappa_{yz}^2 f_{22}\right)\right], \tag{4.35}$$

where we have used abbreviations $\kappa_{ij} = u_{i0}/u_{j0}$, $f \equiv f(\kappa_{xz}, \kappa_{yz})$, and

$$f_i = \frac{\partial}{\partial \kappa_{iz}} f(\kappa_{xz}, \kappa_{yz}), \quad f_{ij} = \frac{\partial^2}{\partial \kappa_{iz}\, \partial \kappa_{jz}} f(\kappa_{xz}, \kappa_{yz}). \tag{4.36}$$

4.2 Interaction effects and the collective modes

The usual low-lying collective oscillation modes, such as the breathing, quadrupole, and radial-quadrupole mode, are direct consequences of the existence of interactions in the system. In the absence of interactions, the many-body physics is reduced to a

one-body problem, and for bosons this amounts to simple disentangled oscillations along the trap axes as the normal modes, with the frequencies equal to twice the corresponding trap frequencies. In this noninteracting case, although each atom would oscillate independently with the corresponding frequency even if no other atoms are present, the fact that the atoms are identical and that all of them would perform the same type of oscillations makes their dynamics practically a collective mode.

The presence of interactions, even if quite weak, changes the situation dramatically and allows the emergence of the well-known collective modes [44]. In the previous section, we have derived the variational expressions for the frequencies of those collective modes and we now study how they are affected by the strength of the contact and the dipole-dipole interaction. We have already seen in Figure 4.1, where the frequencies of the collective modes are calculated variationally as functions of the contact interaction strength by neglecting the DDI, that the breathing and the quadrupole mode frequencies depend very weakly on a_s, while the radial-quadrupole mode is more sensitive. Figure 4.2 presents numerical and variational results for all three atomic species, where we take into account the DDI, both numerically when solving the dipolar GPE and variationally, using the expressions derived in Section 4.1. Not surprisingly, the breathing and the quadrupole mode frequencies still exhibit the flat behavior, while the radial-quadrupole mode shows a significant dependence on a_s. Therefore, the contact interaction strength, which can be tuned in experiments in a very broad range, can be considered as a control parameter only for the radial-quadrupole mode, whose frequency can be adjusted this way, although in a limited range.

From Figure 4.2, we see that our variational approach properly captures the functional behavior of all the modes and gives frequency values, which are in very good agreement with the numerical ones. The absolute errors are of the order of few Hz, which makes them practically negligible for the breathing and the radial-quadrupole mode, while in the case of the quadrupole mode, due to its low value of around 12 Hz, the relative error amounts to 10%.

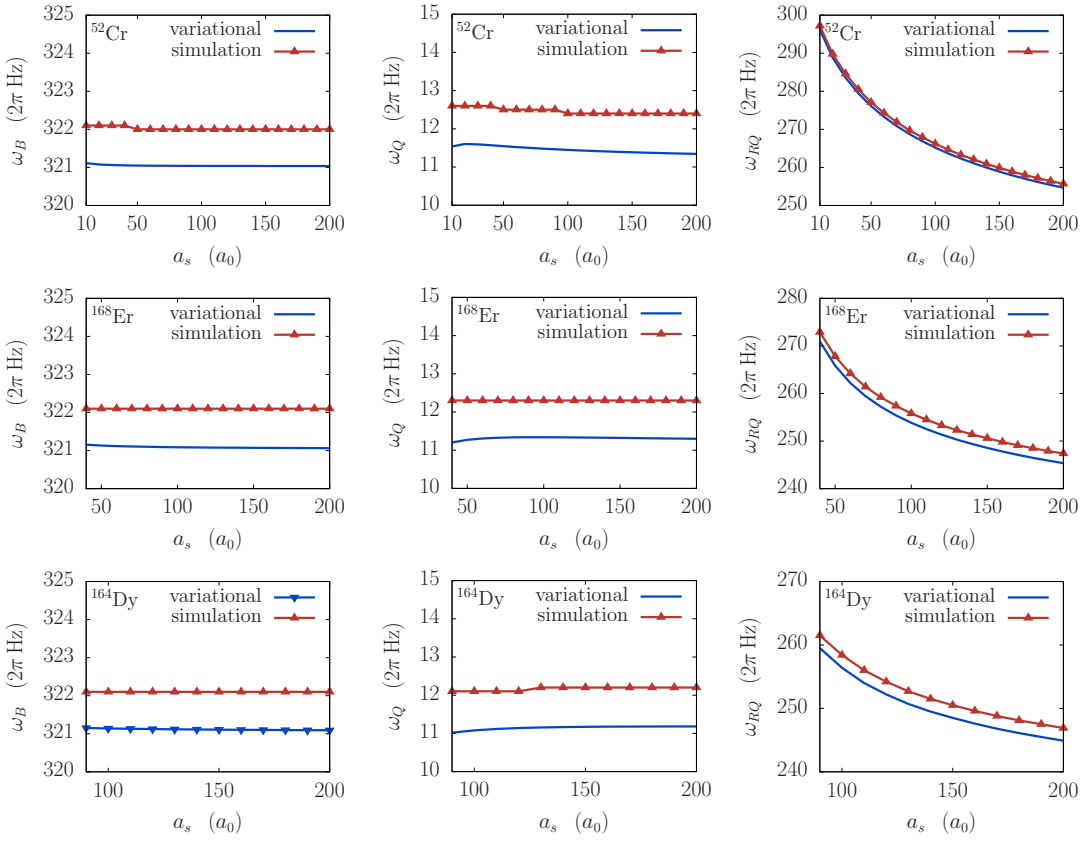

Figure 4.2: Effects of the contact interaction on frequencies of collective oscillation modes: the breathing mode (left column), the quadrupole mode (middle column), the radial-quadrupole mode (right column), for a BEC of $N = 10^4$ atoms of chromium ^{52}Cr (top row), ^{168}Er (middle row), and ^{164}Dy (bottom row), for a fixed dipole-dipole interaction strength given in Appendix D. Red upper triangles are numerically obtained values using the FFT analysis, and blue lines are variational results from Section 4.1.

Next, we focus on the effects of the dipole-dipole interaction strength, presented in Figure 4.3. The results for the breathing and the quadrupole mode are quite similar, although one can see a slight increase in the breathing mode frequency and a slight decrease in the quadrupole mode frequency as a_{dd} increases. However, the radial-quadrupole mode frequency shows a nonmonotonous behavior, albeit in an even more limited range. The variational approach works equally well here as in the case of the contact interaction, and, in particular, it properly describes the nonmonotonous behavior of the radial-quadrupole mode.

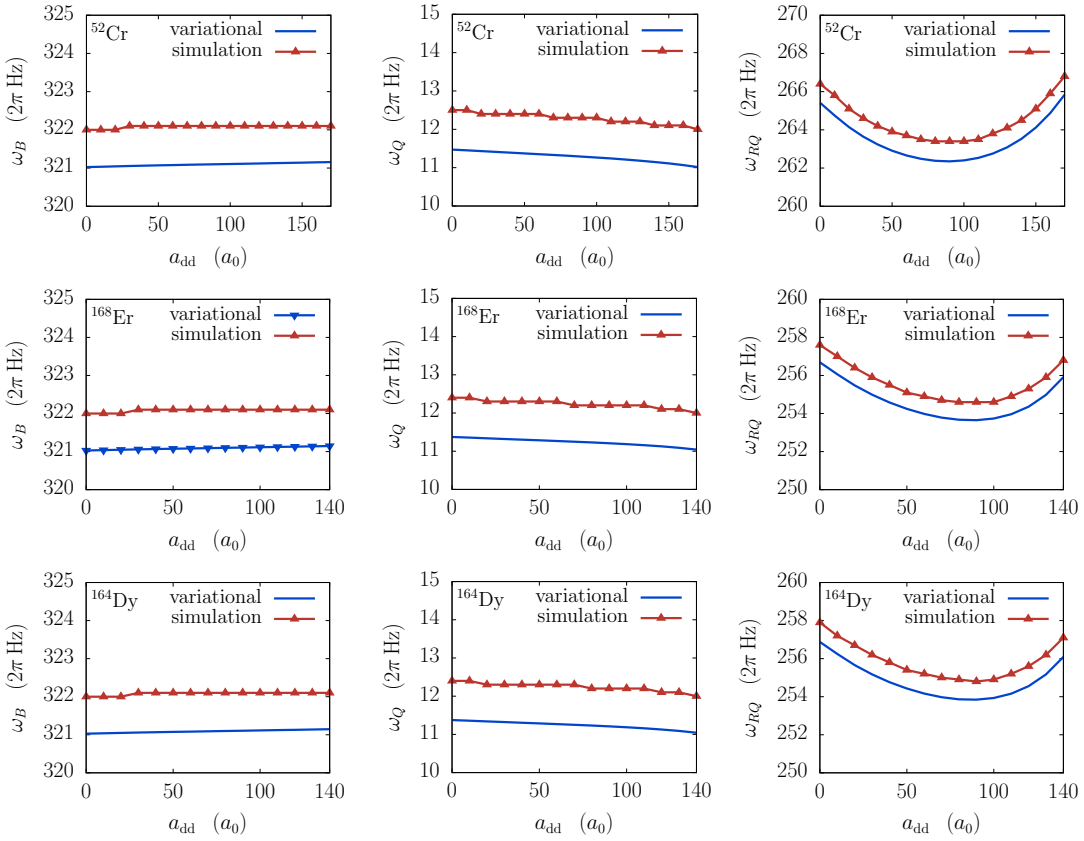

Figure 4.3: Effects of the dipole-dipole interaction on frequencies of collective oscillation modes: the breathing mode (left column), the quadrupole mode (middle column), the radial-quadrupole mode (right column), for a BEC of $N = 10^4$ atoms of chromium ^{52}Cr (top row), ^{168}Er (middle row), and ^{164}Dy (bottom row), for a fixed contact interaction strength given in Appendix D. Red upper triangles are numerically obtained values using the FFT analysis, and blue lines are variational results from Section 4.1.

The precise knowledge of the collective oscillation mode frequencies is essential not only for comparison with the experiments, where measurements of these frequencies are the most precise and can be used for testing of various theoretical and numerical approaches, but also for a deeper understanding of the dynamical response of the system in many experimental situations. This is of particular interest for driven systems, where resonances may appear close to frequencies of collective oscillation modes. This is also relevant for the study of Faraday waves, which can be generated only by modulating the system at non-resonant frequencies, as we will see in Chapter 5.

5 Faraday and resonant waves

In the previous section, we have seen that a small perturbation of one of the system parameters generates collective oscillation modes, which we have analyzed using the spectral analysis of the condensate widths. We demonstrated that frequencies of the collective modes depend on the geometry of the system, as well as on the strength of the contact and the dipole-dipole interactions, but we did not discuss the spatial period of the induced waves since it was much larger than the size of condensate. Therefore, one can assume that the condensate density is only slightly spatially modulated in the presence of collective modes. However, if the perturbation is performed periodically, i.e., if one of the system parameters is harmonically modulated in time, the spatial period can become small enough to produce observable density patterns in the condensate. The classical phenomenon of Faraday waves inspired this line of research [28], and although oscillations of a shallow layer of liquid generate surface waves, while periodic modulation of one of the system parameters of a quantum fluid produces density waves, both share the common name in the literature – Faraday waves.

Bose-Einstein condensates are usually termed quantum fluids, which encompasses a broader range of physical systems where quantum effects are either dominant or very much pronounced. Despite their name, some of quantum fluids do not share the trademark property of classical fluids, incompressibility. In fact, the BECs are made of rarefied gases, but their fluid-like behavior stems from the quantum coherence of such systems. Therefore, while in classical fluids density modulations can be excited only under extreme conditions, in quantum fluids the density waves

represent one of the natural collective excitations. Parametric driving of system parameters can lead to pattern formation not only in BECs, where Faraday waves are experimentally observed in cigar-shaped rubidium [30] and lithium [47] condensates, but also in helium cells [48]. The actual experimental observation of this phenomenon in 2007 was preceded by numerical studies starting in 2002 [29, 49–53], all focusing on systems with short-range, contact interactions. More recently, Faraday waves have been studied in dipolar [33, 54–56] and two-component condensates, including the systems with spatially-dependent contact interaction [31, 32]. Numerical studies of Faraday waves have also been extended to mixtures of Bose and Fermi gases [57], as well as Fermi gases exhibiting superfluid behavior [58, 59]. An interesting phenomenon of Bose fireworks [60] is related to Faraday waves, but appears during the free expansion of the system, when density patterns may also emerge [61–63].

The parametric modulation of a BEC system generically leads to the emergence of the Faraday waves. However, resonant behavior can also be observed if the system is modulated at one of its collective mode frequencies [64]. In that case, the Faraday waves are suppressed and resonant waves emerge on a much shorter time scale. Interestingly this can happen not only by modulation of the interaction strength, but also by the modulation of the trapping potential or even the spatial modulation of the trap [65–79].

In the context of dipolar BECs, the study of Faraday waves was limited mostly to their excitation spectrum in one-dimensional and two-dimensional systems [54], while the properties of resonant waves were not studied to the best of our knowledge. Here, we focus on an analytical description of Faraday and resonant waves in dipolar condensates [33]. In particular, we study how such waves develop in ultracold systems of three dipolar species: chromium [10], erbium [12], dysprosium [11]. We consider the system with the parameters specified in Appendix D, with the dipoles oriented along z direction and the cigar-shaped trap in the weakly confined x direction. The radial $(y-z)$ component of the trap is harmonically modulated,

$$\omega_y(t) = \omega_z(t) = \Omega_0(1 + \epsilon \sin \omega_m t)\,, \tag{5.1}$$

where $\epsilon = 0.1 - 0.2$ is the modulation amplitude and ω_m is modulation frequency. These are typical values taken from the experiment of Reference [30].

In this chapter, we develop a variational approach for the study of the dynamics of a driven dipolar BEC and identify the instability of the system leading to the emergence of Faraday and resonant waves. Using this approach, we calculate the dependence of wave properties on the strength of the contact and the dipole-dipole interaction. The analytically obtained expressions for the spatial period of Faraday and resonant waves are compared to results of the extensive numerical simulations, which solve the full three-dimensional mean-field equations for a dipolar BEC.

5.1 Variational approach

For a variational study of Faraday and resonant waves in dipolar condensates, we use a modification [31, 32, 49–53, 56, 64, 80, 81] of the Gaussian ansatz (2.52) to capture the induced density waves in the direction of weak confinement (x direction),

$$\psi(x,y,z,t) = A\, e^{-\frac{x^2}{2u_x^2}-\frac{y^2}{2u_y^2}-\frac{z^2}{2u_z^2}+ix^2\phi_x+iy^2\phi_y+iz^2\phi_z}\left[1+(\alpha+i\beta)\cos kx\right], \tag{5.2}$$

where $A \equiv A(u_x, u_y, u_z, \alpha, \beta, k)$ ensures the normalization of the wave function to unity,

$$A = \frac{1}{\pi^{3/4}\sqrt{u_x u_y u_z}}\frac{\sqrt{2}}{\sqrt{2+\alpha^2+\beta^2+4\alpha\, e^{-k^2u_x^2/4}+(\alpha^2+\beta^2)\, e^{-k^2u_x^2}}}. \tag{5.3}$$

The above variational ansatz involves eight variational parameters $\{u_i, \phi_i, \alpha, \beta\}$, which are functions of time. The parameters u_i represent the condensate widths, while ϕ_i are the conjugated phases, which are necessary to describe the system's dynamics properly. Note that these phases can be omitted when we are interested only in the ground state. The multiplicative factor $1 + (\alpha + i\beta)\cos kx$ describes the density modulation along x direction, and the variational parameters α and β represent the real and the imaginary part of the amplitude of the wave. The wave vector k, which is related to the spatial period ℓ of the density waves by $\ell = 2\pi/k$, is not treated here as a variational parameter. We determine its value from the condition for the instability emergence, which leads to Faraday or resonant waves.

If we insert the modified Gaussian ansatz (5.2) into the Lagrangian density (2.51), we obtain the expressions for the five terms (2.53) of the Lagrangian of the system. The first term reads

$$L_1(t) = \frac{i}{2}\int d\mathbf{r}\,\left(\psi^*\dot{\psi} - \psi\dot{\psi}^*\right) = -\frac{1}{2}\left(u_x^2\dot{\phi}_x + u_y^2\dot{\phi}_y + u_z^2\dot{\phi}_z\right) - \frac{\alpha\dot{\beta} - \beta\dot{\alpha}}{2+\alpha^2+\beta^2}\,, \quad (5.4)$$

and the kinetic energy term is equal to

$$\begin{aligned} L_2(t) &= \frac{1}{2}\int d\mathbf{r}\,\psi^*\nabla^2\psi \\ &= -\frac{1}{4}\left(\frac{1}{u_x^2} + \frac{1}{u_y^2} + \frac{1}{u_z^2} + 4u_x^2\phi_x^2 + 4u_y^2\phi_y^2 + 4u_z^2\phi_z^2\right) - \frac{(\alpha^2+\beta^2)\,k^2}{2(2+\alpha^2+\beta^2)}\,. \end{aligned} \quad (5.5)$$

The potential energy term is calculated using the expression (2.47) for the potential, yielding

$$L_3(t) = -\int d\mathbf{r}\,U\,|\psi|^2 = -\frac{1}{4}\left(\gamma^2u_x^2 + \nu^2u_y^2 + \lambda^2u_z^2\right)\,, \quad (5.6)$$

while the contact interaction term reads

$$L_4(t) = -2\pi N a_s\int d\mathbf{r}\,|\psi|^4 = -\frac{Na_s}{\sqrt{2\pi}\,u_xu_yu_z}\left(1 + \frac{\alpha^4+16\alpha^2+2\alpha^2\beta^2+\beta^4)}{2(2+\alpha^2+\beta^2)^2}\right)\,. \quad (5.7)$$

The Lagrangian term that corresponds to the DDI is calculated following a procedure similar to the one described in Section 2.4. However, due to the modulation term in the modified Gaussian ansatz, it is not possible to perform exact integration to obtain $L_5(t)$. Using the convolution theorem, the DDI term can be written as

$$L_5(t) = -\frac{3Na_{\rm dd}}{2\,(2\pi)^3}\int d\mathbf{k}\,\mathcal{F}\left[U_{\rm dd}\right](\mathbf{k})\,\mathcal{F}\left[|\psi|^2\right](\mathbf{k})\int d\mathbf{r}\,|\psi|^2\,e^{i\,\mathbf{k}\cdot\mathbf{r}}\,, \quad (5.8)$$

where the last integral is equal to $\mathcal{F}\left[|\psi|^2\right](\mathbf{k})$, and can be calculated exactly,

$$\mathcal{F}\left[|\psi|^2\right](\mathbf{k}) = B\,e^{-\frac{1}{4}(k_x^2u_x^2+k_y^2u_y^2+k_z^2u_z^2)}\,, \quad (5.9)$$

where $B \equiv B(k_x, u_x, \alpha, \beta, k)$ is given by

$$B = \frac{4 + 4(e^{-\frac{k}{4}(k-2k_x)u_x^2} + e^{-\frac{k}{4}(k+2k_x)u_x^2})\,\alpha + (2 + e^{-k(k-k_x)u_x^2} + e^{-k(k+k_x)u_x^2})\,(\alpha^2+\beta^2)}{2\left[2 + 4\,e^{-\frac{1}{4}k^2u_x^2}\alpha + (1+e^{-k^2u_x^2})\,(\alpha^2+\beta^2)\right]}. \quad (5.10)$$

Grouping all elements together, the DDI term of the Lagrangian becomes

$$L_5(t) = -\frac{3Na_{\rm dd}}{(2\pi)^2}\int d\mathbf{k}\,\left(3\,\frac{k_z^2}{k_x^2+k_y^2+k_z^2} - 1\right)B^2e^{-\frac{1}{2}(k_x^2u_x^2+k_y^2u_y^2+k_z^2u_z^2)}\,, \quad (5.11)$$

and cannot be exactly calculated. To proceed further, we take into account that the condensate width in the weak confinement direction is large compared to the order widths, as well as compared to the spatial period of the density waves, such that $ku_x \gg 1$. We also take into account that the wave amplitude is small immediately after the waves emerge, such that $\alpha, \beta \ll 1$. Therefore, we approximate the expression for B^2 in the following manner

$$B^2 \approx 1 + \frac{\alpha}{2+\alpha^2+\beta^2} B_1^2 + \frac{\alpha^2}{(2+\alpha^2+\beta^2)^2} B_2^2 \,, \tag{5.12}$$

where $B_1^2 \equiv B_1^2(k_x, u_x, k)$ and $B_2^2 \equiv B_2^2(k_x, u_x, k)$ are given by

$$B_1^2 = 4\, e^{-\frac{1}{4}k(k+2k_x)u_x^2} \left(e^{\frac{1}{2}kk_x u_x^2} - 1 \right)^2 , \tag{5.13}$$

$$B_2^2 = 4\, e^{-\frac{1}{4}k(k+2k_x)u_x^2} \left(e^{\frac{1}{2}kk_x u_x^2} - 1 \right)^2 \left(e^{kk_x u_x^2} - 6e^{\frac{1}{2}kk_x u_x^2} + 1 \right) , \tag{5.14}$$

and correspond to the coefficients in front of the terms linear and quadratic in the wave amplitude, respectively. Since the integral over $\mathbf{k}$ cannot be performed exactly even for the approximate expression (5.12), we replace the coefficients B_1^2 and B_2^2 by their averages over k_x,

$$\langle B_i^2 \rangle = \frac{\int dk_x \left(3\, \frac{k_z^2}{k_x^2+k_y^2+k_z^2} - 1 \right) B_i^2\, e^{-\frac{1}{2}k_x^2 u_x^2}}{\int dk_x \left(3\, \frac{k_z^2}{k_x^2+k_y^2+k_z^2} - 1 \right) e^{-\frac{1}{2}k_x^2 u_x^2}} \approx \frac{\int dk_x \left(3\, \frac{k_z^2}{k_x^2} - 1 \right) B_i^2\, e^{-\frac{1}{2}k_x^2 u_x^2}}{\int dk_x \left(3\, \frac{k_z^2}{k_x^2} - 1 \right) e^{-\frac{1}{2}k_x^2 u_x^2}} \tag{5.15}$$

After that, we obtain $\langle B_1^2 \rangle \approx 0$ and $\langle B_2^2 \rangle \approx -8$. Note that we have neglected all terms proportional to $e^{-k^2 u_x^2/8}$ and its powers, as already argued that ku_x is a large quantity. Therefore, B^2 turns out to depend only on α and β, and reads

$$B^2 \approx 1 - \frac{8\,\alpha^2}{(2+\alpha^2+\beta^2)^2} \,. \tag{5.16}$$

If we look at the expression (5.11), we see that now B^2 can be put in front of the integral sign, and integration over $\mathbf{k}$ can now proceed as in Section 2.4, yielding, i.e., the DDI term of the Lagrangian in terms of the anisotropy function f becomes

$$L_5(t) = \frac{N a_{\rm dd}}{\sqrt{2\pi}\, u_x u_y u_z} f\left(\frac{u_x}{u_z}, \frac{u_y}{u_z} \right) \left(1 - \frac{8\alpha^2}{(2+\alpha^2+\beta^2)^2} \right) . \tag{5.17}$$

Let us compare the calculated Lagrangian terms (2.54)–(2.57) and (2.65) in Section 2.4 with expressions (5.4)–(5.7) and (5.17), respectively. Except for the potential energy term $L_3(t)$, which remains unchanged, we see that all other terms are

modified by an additional additive or multiplicative factor, arising due to additional variational parameters α and β. The Euler-Lagrange equations for the system are given by

$$\frac{d}{dt}\left(\frac{\partial L}{\partial \dot{q}_i}\right) - \frac{\partial L}{\partial q_i} = 0\,, \quad q_i \in \{u_x, u_y, u_z, \phi_x, \phi_y, \phi_z, \alpha, \beta\}\,, \tag{5.18}$$

where L is a sum of all five calculated terms. Assuming that the wave amplitudes α and β are small, such that their quadratic and higher-order terms can be neglected, the equations for the condensate widths, turn out to coincide with those obtained in Section 2.4. The three equations for the phases ϕ_i yield, as in Section 2.4,

$$\phi_i = \frac{\dot{u}_i}{2u_i}\,. \tag{5.19}$$

After elimination of the phases ϕ_i from the corresponding set of equations for the condensate widths u_i, we obtain the second-order differential equations (2.69)–(2.71) again. The Euler-Lagrange equation for the variational parameters β yields

$$\beta = \frac{2\dot{\alpha}}{k^2}\,, \tag{5.20}$$

which we use to eliminates β from the corresponding equation for the parameter α, as was done with the phases. With this, the equation for α turns out to be the second-order differential equation,

$$\ddot{\alpha} + \left\{\frac{k^4}{4} + \sqrt{\frac{2}{\pi}}\frac{N}{u_x u_y u_z}\left[a_s + a_{\rm dd}\, f\left(\frac{u_x}{u_z}, \frac{u_y}{u_z}\right)\right] k^2\right\}\alpha = 0\,. \tag{5.21}$$

In the context of variational analysis of Faraday and resonant waves, the above equation of motion for the wave amplitude α is usually cast into the form of the Mathieu-like equation

$$\ddot{\alpha} + [a(k) + \epsilon b(k)\sin 2\tau]\,\alpha = 0\,. \tag{5.22}$$

This equation can be solved perturbatively in the small modulation amplitude ϵ. Assuming a solution in the form of a harmonic oscillator

$$\alpha(\tau, \epsilon) = P(\epsilon\tau)\cos\left(\tau\sqrt{a(k)}\right) + Q(\epsilon\tau)\sin\left(\tau\sqrt{a(k)}\right)\,, \tag{5.23}$$

we obtain that functions P and Q are exponentials of the form $e^{\pm i\xi\tau}$, where ξ is a complex number. The existence of the imaginary part of ξ leads to the instability,

i.e., to the exponential growth of the wave amplitude, which yields Faraday or resonant waves. It was shown in Reference [82] that the nonvanishing imaginary part of ξ appears for $a(k) = n^2$, where $n \in \mathbb{N}$, and this represents the mathematical form of the instability condition.

In order to cast Equation (5.21) into the Mathieu-like form (5.22), we need to take into account that the radial trap frequencies are modulated, such that the corresponding trap aspect ratio is given by $\nu(t) = \lambda(t) = \lambda_0(1 + \epsilon \sin \eta_m t)$, where $\lambda_0 = \Omega_0/\omega_r$ and $\eta_m = \omega_m/\omega_r$. This generates the dynamics of the system and we need to obtain approximate expressions for the condensate widths in order to get an explicit form of the quantities $a(k)$ and $b(k)$. We assume that the condensate width u_x slowly varies, and can be taken to be constant at the onset of instability. We also assume that second derivatives of the radial widths u_y and u_z, with respect to time, can be neglected, since they are proportional to the small modulation amplitude ϵ. Furthermore, for simplicity, we assume $u_y \approx u_z \equiv u_\rho$, which now satisfies the modified equation (2.70) or (2.71),

$$\lambda^2(t) u_\rho^4 = 1 + \sqrt{\frac{2}{\pi}} \frac{N}{u_x} \left[a_s + \frac{a_{\rm dd}}{2} f_s\left(\frac{u_\rho}{u_x}\right) - a_{\rm dd} f_s'\left(\frac{u_\rho}{u_x}\right) \right] . \tag{5.24}$$

On the right-hand side of the above equation we assume that the ratio u_ρ/u_x is constant and equal to the corresponding ration for the ground state, which can be calculated as in Section 3.1. To derive Equation (5.24), we also use the following limits of the anisotropy function

$$\begin{aligned} f_s^{'}(x) = \lim_{y\to x} x\, f_1(x,y) = \lim_{y\to x} y\, f_2(x,y) = \frac{(2+x^2) f_s(x)}{2(1-x^2)} - 1\,, \\ \lim_{y\to 1} f(x,y) = -\frac{1}{2} f_s(1/x)\,, \qquad \lim_{y\to 1} x f_1(x,y) = f_s^{'}(1/x)\,, \end{aligned} \tag{5.25}$$

If we express u_ρ^2 from Equation (5.24), and use it to estimate the quantity $u_y u_z \approx u_\rho^2$ in Equation (5.21), as well as the above limits, that yield

$$f\left(\frac{u_x}{u_z}, \frac{u_y}{u_z}\right) = -\frac{1}{2} f_s\left(\frac{u_\rho}{u_x}\right) , \tag{5.26}$$

the equation for the variational parameter α can be written as

$$\ddot{\alpha} + \left[\frac{k^4}{4} + \frac{\Lambda k^2}{4}\lambda(t)\right] \alpha = 0\,, \tag{5.27}$$

where Λ is given by

$$\Lambda = \frac{4\sqrt{\frac{2}{\pi}}\, N \left[a_s - \frac{a_{\rm dd}}{2}\, f_s\left(\frac{u_\rho}{u_x}\right)\right]}{u_x \left\{1 + \sqrt{\frac{2}{\pi}}\frac{N}{u_x}\left[a_s + \frac{a_{\rm dd}}{2} f_s\left(\frac{u_\rho}{u_x}\right) - a_{\rm dd} f_s'\left(\frac{u_\rho}{u_x}\right)\right]\right\}^{1/2}}\,. \tag{5.28}$$

Inserting the explicit form for $\lambda(t)$, we obtain

$$\ddot{\alpha} + [a(k) + \epsilon b(k) \sin \eta_m t]\, \alpha = 0\,, \tag{5.29}$$

where

$$a(k) = \frac{k^4}{4} + \frac{\lambda_0 \Lambda k^2}{4}\,, \qquad b(k) = \frac{\lambda_0 \Lambda k^2}{4}\,. \tag{5.30}$$

In order to transform the above equation into the Mathieu-like equation (5.22), we need to make a variable change $\eta_m t \to 2\tau$, which finally yields the expressions for the coefficients $a \equiv a(k)$ and $b \equiv b(k)$,

$$a(k) = \frac{k^4}{\eta_m^2} + \frac{\lambda_0 \Lambda k^2}{\eta_m^2}\,, \qquad b(k) = \frac{\lambda_0 \Lambda k^2}{\eta_m^2}\,. \tag{5.31}$$

As previously discussed, the instability condition for the Faraday waves reads $a(k) = 1$, which can be used to calculate the wave vector of waves shortly after the emergence of the waves,

$$k_F = \sqrt{-\frac{\lambda_0 \Lambda}{2} + \sqrt{\frac{\lambda_0^2 \Lambda^2}{4} + \eta_m^2}}\,. \tag{5.32}$$

This represents the variational prediction for the wave vector k and the spatial period $\ell = 2\pi/k$ of the Faraday waves, which can be directly compared with numerical or experimental results. Let us also stress that the above analysis is consistent with the main characteristic of the Faraday waves, namely, that their oscillation frequency is half that of the driving frequency. Since $\tau = \eta_m t/2$, from Equation (5.22) we see that indeed, the solution of the derived Mathieu-like equation oscillates with the frequency $\eta_m/2$, i.e., with the frequency $\omega_m/2$.

If the modulation frequency is close to one of the collective oscillation modes, the system will exhibit resonant behavior, which is suppressed for an arbitrary value of the modulation frequency. While the system's dynamics will certainly include the Faraday mode at the frequency $\omega_m/2$ even close to a resonance, the resonant

mode with the frequency ω_m will have a larger amplitude and will develop much faster. Although it is clear that the analysis of this section would break down, the condition for the emergence of resonant waves still corresponds to $a(k) = 2^2$, i.e., the wave vector of the resonant wave is given by

$$k_R = \sqrt{-\frac{\lambda_0 \Lambda}{2} + \sqrt{\frac{\lambda_0^2 \Lambda^2}{4} + 4\eta_m^2}}\,. \tag{5.33}$$

In that case, according to $\tau = \eta_m t/2$ and Equation (5.23), the resonant density wave will oscillate with the frequency whose aspect ratio is $(\eta_m/2)\sqrt{2^2} = \eta_m$, i.e., with the frequency ω_m. Depending on the system's parameters, higher resonant modes can also appear corresponding to the conditions $a(k) = n^2$, where n is an integer, corresponding to the oscillation frequencies $n\omega_m/2$.

5.2 Faraday waves in ^{52}Cr, ^{168}Er and ^{164}Dy BECs

In order to study Faraday waves in dipolar condensates, we have performed extensive numerical simulations of the real-time dynamics and solved the dipolar GPE using the programs described in Chapter 6. The parameters for these simulations closely match the physical parameters of BECs of chromium ^{52}Cr, erbium ^{168}Er, and dysprosium ^{164}Dy, which are given in detail in Appendix D. It is well known [65–79] that Faraday waves can be expected as a main excitation mode of the system when the modulation frequency ω_m does not match any of the characteristic frequencies of the system, i.e., when it is sufficiently far from any of the collective oscillations modes or the trap frequencies. Therefore, we use the value $\omega_m = 200 \times 2\pi$ Hz, which we know satisfies these conditions from our study of collective modes from Chapter 4, and the values of the trap frequencies listed in Appendix D.

Figure 5.1 shows time dependence of the integrated density profile in the weak confinement direction $n(x, t)$, which is obtained by integrating the condensate density over the radial coordinates y and z according to Equation (3.14). The emergence of spatial patterns is clearly visible for all three atomic species after around 150 ms. This is consistent with earlier experimental observations [30, 47] and theoretical re-

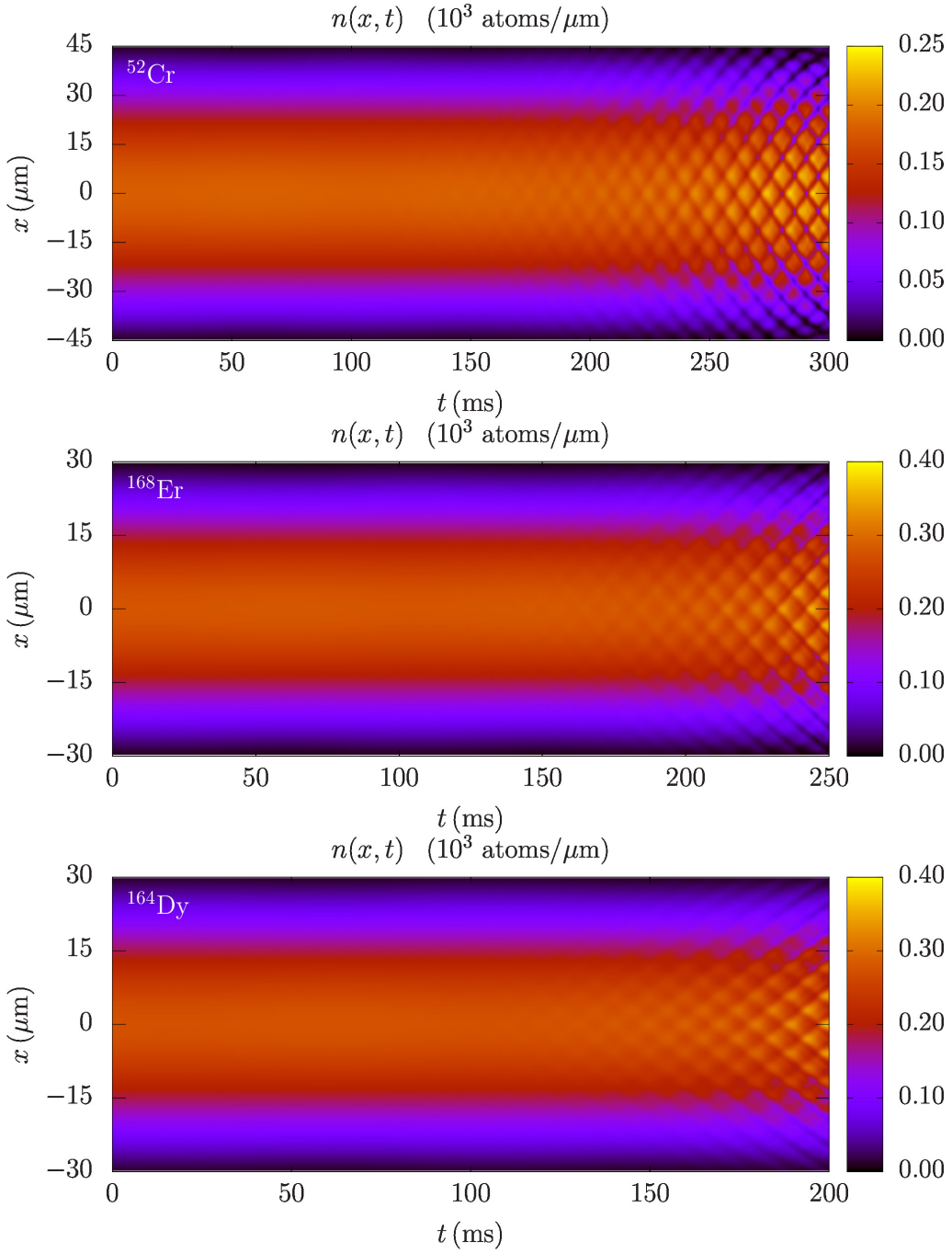

Figure 5.1: Time evolution of the integrated density in the weak confinement direction for a BEC of $N = 10^4$ atoms of chromium ^{52}Cr (top), erbium ^{168}Er (middle), and dysprosium ^{164}Dy (bottom). The results are obtained for a periodic modulation of the trap frequencies ω_y and ω_z according to Equation 5.1 with $\epsilon = 0.2$ and $\omega_m = 200 \times 2\pi$ Hz. The contact interaction strength is $a_s = 150\,a_0$ and the DDI strength is given in Appendix D for each species. The Faraday waves can be visually observed after approximately 150 ms for all three species.

sults [65–79]. The density waves in x direction from Figure 5.1 take time to develop and are the result of the transfer of energy from the modes that are directly excited in the radial directions, where the trap is modulated. This can be seen in Figure 5.2, where we show the corresponding time dependence of integrated density profiles in y and z direction. The density waves in the radial directions emerge immediately after the modulation is switched on at $t = 0$, and their frequency is equal to the mod-

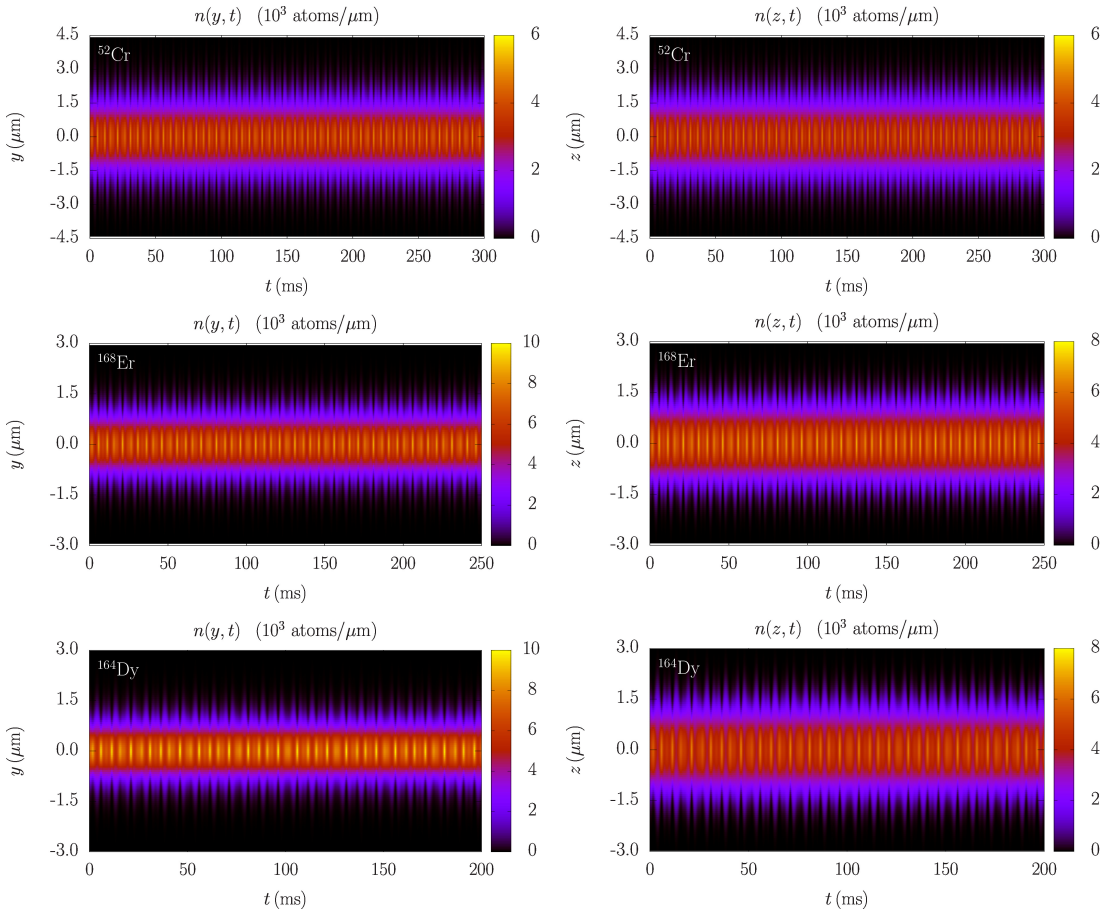

Figure 5.2: Time evolution of the integrated density in y direction (left column) and z direction (right column) for a BEC of $N = 10^4$ atoms of chromium ^{52}Cr (first row), erbium ^{168}Er (second row), and dysprosium ^{164}Dy (third row). The results are obtained for the same parameters as in Figure 5.1. The frequency of oscillations of the condensate densities in the radial direction is equal to $\omega_m = 200 \times 2\pi$ Hz. We see that, due to the dipole-dipole interaction, the width of the condensate is larger in the direction parallel to the dipoles (z direction) than in the orthogonal direction (y direction), in particular for ^{168}Er and ^{164}Dy, as already shown in Section 3.3.

ulation frequency. Comparing the left and right column in Figure 5.2, we can also directly observe the DDI effects. As we know, the dipole-dipole interaction causes the elongation of the condensate width in the polarization direction of the dipoles. Although the trap frequencies in y and z direction are equal, we see in Figure 5.2 that the condensate widths in z direction for all three species are larger than the corresponding y direction widths, and the difference increases as the strength of the DDI increases from chromium to dysprosium.

In order to characterize the density waves, we typically analyze their FFT spectra in the time-frequency and in the spatial-frequency domain. This enables us to determine the frequencies of the main excitation modes, as well as the spatial period of the observed density patterns. However, instead of directly analyzing the density profiles presented in Figures 5.1 and 5.2, for the FFT it is advantageous to have a clearer signal, which can be obtained by considering only the density variations compared to the initial state, i.e., the ground state of the system, before the modulation is switched on. The integrated density profile variation in the confined x direction is shown in Figure 5.3, and the corresponding density profile variations in y and z directions are presented in Figure 5.4.

As expected, the emergence of Faraday waves is now more easily discernible in Figure 5.3, and the same applies to the oscillations of the density shown in Figure 5.4. By looking at these two figures, we can even estimate the main oscillation frequency, e.g., counting the number of maxima or minima in a given time interval. For instance, in the last 50 ms in each of the panels in Figure 5.3 we count 5 periods, which corresponds to the frequency $100 \times 2\pi$ Hz $= \omega_m/2$. This is a distinguishing characteristic of Faraday waves, and therefore we directly determine that in this case the system develops this type of collective oscillations. On the other hand, in Figure 5.4 we can count 10 periods (maxima or minima) in a given 50 ms time interval, which corresponds to the modulation frequency ω_m. Thus, in the radial directions we observe as the main excitation mode the direct response of the system to the harmonic modulation of the trap.

However, this way we can determine only the main excitation modes. The dy-

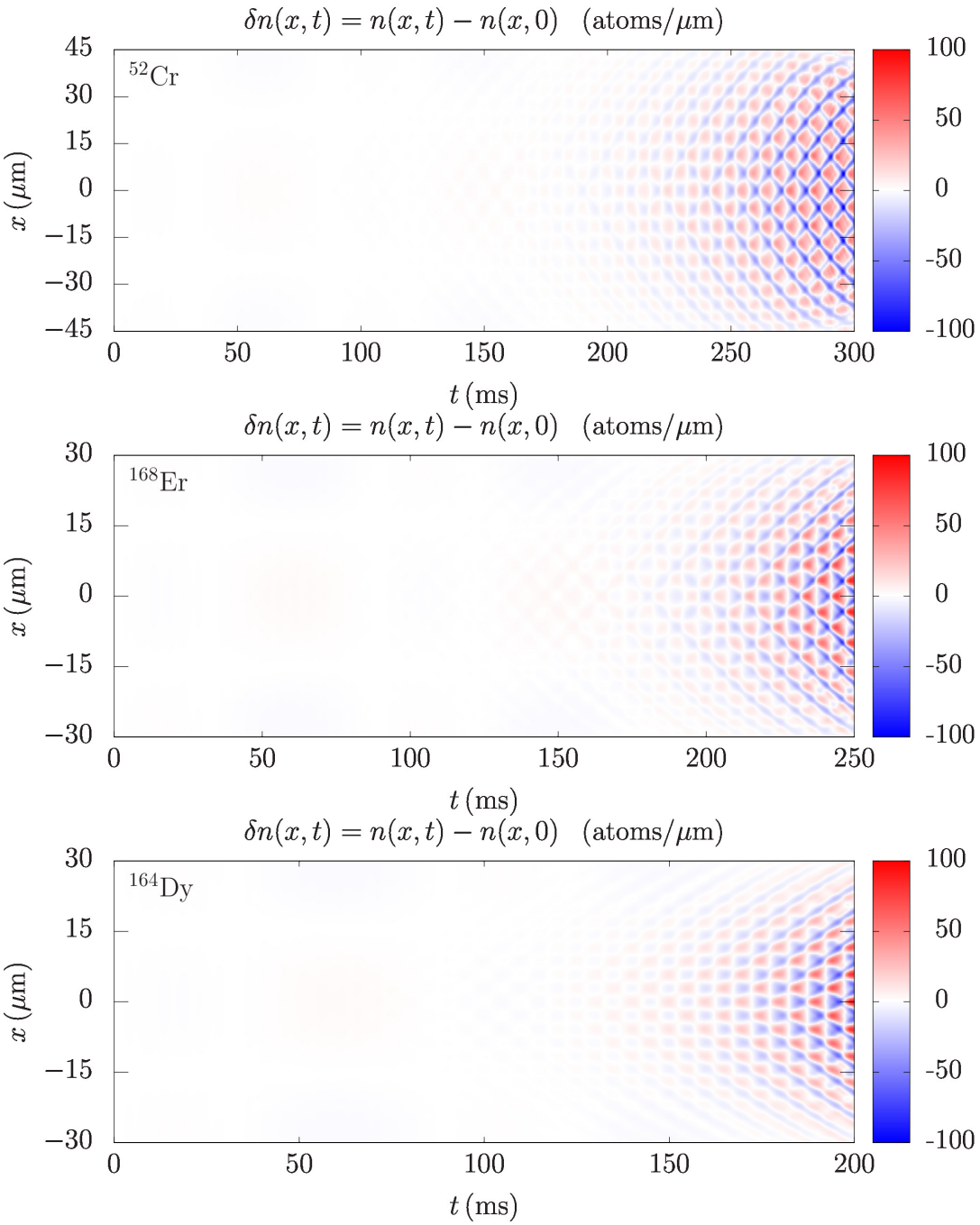

Figure 5.3: Time evolution of the integrated density profile variation in the weak confinement direction for a BEC of $N = 10^4$ atoms of chromium ^{52}Cr (top), erbium ^{168}Er (middle), and dysprosium ^{164}Dy (bottom), for the same parameters as in Figure 5.1. The variations $\delta n(x,t)$ are obtained by subtracting the density profile of the ground state $n(x, t = 0)$ from the time-dependent integrated density $n(x,t)$ presented in Figure 5.1.

namics of the system contains other modes as well, and, over time, they can develop and even start to dominate the behavior of the system. Therefore, it is important to analyze the spectra in more detail. This is done in Figure 5.5 for all integrated density profile variations from Figures 5.3 and 5.4. For simplicity, the FFT analysis is performed for the profiles at the trap center. As expected, in the weak confinement direction, the left column in Figure 5.5, the main excitation mode has a frequency $\omega_m/2$. In addition to this, we observe two other modes, at ω_m and $3\,\omega_m/2$. This

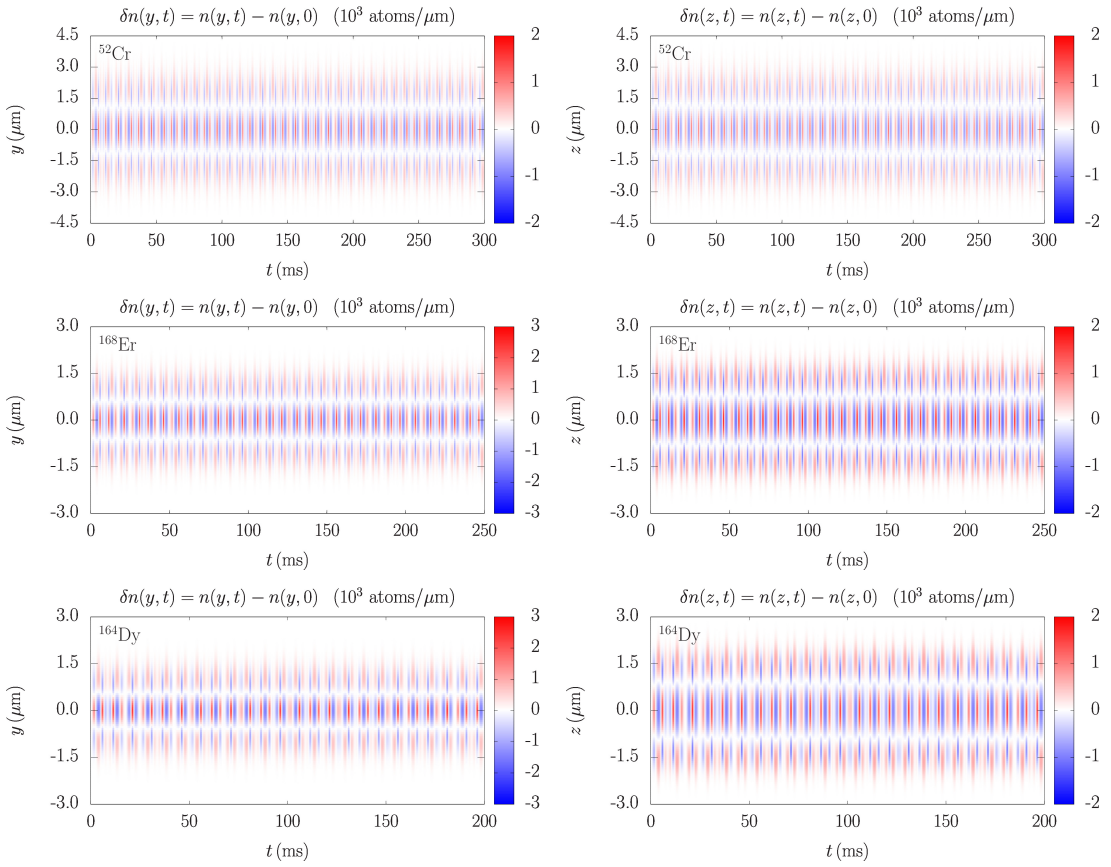

Figure 5.4: Time evolution of the integrated density profile variations in y direction (left column) and in z direction (right column) for a BEC of $N = 10^4$ atoms of chromium ^{52}Cr (first row), erbium ^{168}Er (second row), and dysprosium ^{164}Dy (third row), for the same parameters as in Figure 5.1. The variation in a given direction y or z is obtained by subtracting the density profile of the ground state from the corresponding time-dependent integrated density presented in Figure 5.2. The difference between the condensate widths in y and z direction, which was observed in Figure 5.2, is also clearly visible here.

is expected from the theoretical analysis in Section 5.1, but could not be discerned directly from the density profiles or their variations.

In the Fourier spectra of the integrated density profile variations in the radial directions, middle and right column in Figure 5.5, we see a somewhat richer set of excitation modes. In addition to the main mode corresponding to the trap modulation at ω_m, we see that also the breathing mode is excited at the frequency $\omega_B \approx 321 \times 2\pi$ Hz, which was determined in Section 4.1. The spectra prominently contain the second modulation harmonic at $2\,\omega_m$ as well. We see some other peaks in the spectra as well. For instance, the small peak at around $120 \times 2\pi$ Hz, which can be due to the linear combination of the modes $\omega_B - \omega_m$. However, such an identification would require further theoretical and numerical analysis, which is out of the scope of this thesis.

While the Fourier analysis in the time-frequency domain can be used to determine the character of the induced density waves (Faraday, collective, resonant), the analysis in the spatial-frequency domain enables us to characterize the density patterns and calculate their spatial period. This is illustrated in Figure 5.6 for Faraday waves for all three considered atomic species. The integrated density profile variations are analyzed at appropriate times, which are determined to correspond to the evolution stage when Faraday waves have fully emerged, but the system is still far from the violent dynamics that inevitably follows after the long driving period.

In all three panels of Figure 5.6 the main peak corresponds to the wave vector k_F of the Faraday waves, and we see significant differences: for ^{52}Cr we obtain $k_F = 0.57\,\mu\text{m}^{-1}$, yielding the spatial period $\ell = 2\pi/k_F = 11.02\mu$m; for ^{168}Er we get $k_F = 0.98\,\mu\text{m}^{-1}$ and $\ell = 6.41\mu$m; for ^{164}Dy we have $k_F = 1.10\,\mu\text{m}^{-1}$ and $\ell = 5.71\mu$m. The variational analysis presented in Section 5.1 yields results which are in good agreement with the numerical ones, namely $k_F = 0.51\,\mu\text{m}^{-1}$ for ^{52}Cr, $k_F = 0.91\,\mu\text{m}^{-1}$ for ^{168}Er, and $k_F = 1.06\,\mu\text{m}^{-1}$ for ^{164}Dy. These variational results are shown in Figure 5.6 by vertical blue lines, which illustrates their agreement with the Fourier analysis. The presented spectra also contain some additional peaks that correspond to other geometrical features of the analyzed density profile variations,

such as the condensate width and its higher harmonics, as well as the higher harmonics of the Faraday wave periods, and linear combinations of all of these. However, they are not of interest in our analysis and we will not study them further.

Note that the spatial period of Faraday waves can be also determined by directly looking at the density profile variations in Figure 5.3, and estimating the spacing between the consecutive minima or maxima at the appropriate evolution time. For

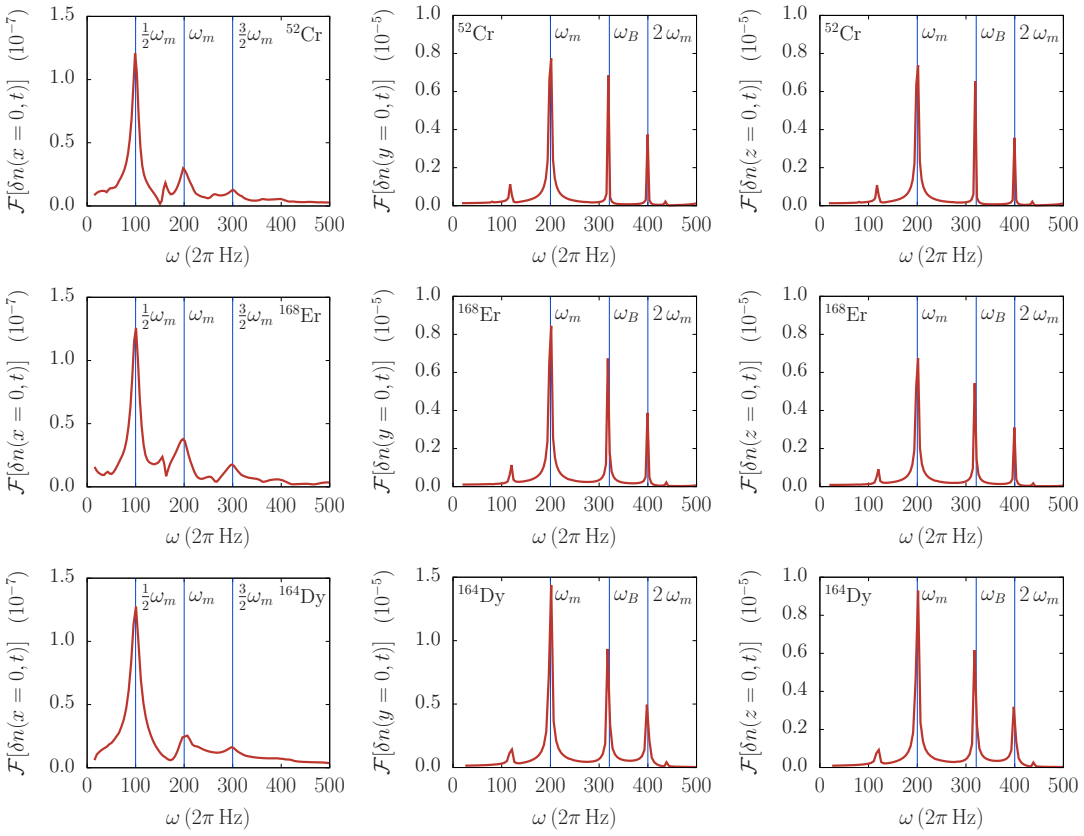

Figure 5.5: The Fourier spectrum in the time-frequency domain of the integrated 1D density profile variations of Faraday waves at the trap center $\delta n(x=0,t)$ in x direction (first column), $\delta n(y=0,t)$ in y direction (second column), and $\delta n(z=0,t)$ in z direction (third column) for a BEC of $N=10^4$ atoms of chromium ^{52}Cr (first row), erbium ^{168}Er (second row), and dysprosium ^{164}Dy (third row). The corresponding density profile variations are shown in Figures 5.3 and 5.4. Vertical blue lines represent theoretical predictions, where $\omega_m/2$ corresponds to Faraday waves, ω_m and $2\,\omega_m$ to resonant waves, and ω_B is the variational result for the breathing mode frequency obtained in Section 4.1.

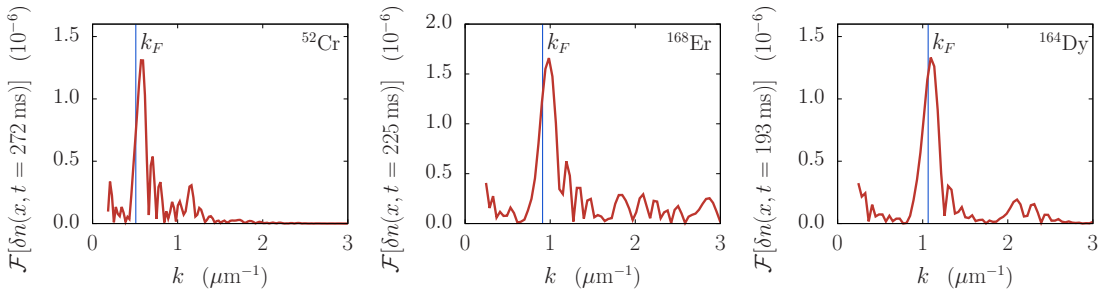

Figure 5.6: The Fourier spectrum in the spatial-frequency domain of the integrated 1D density profile variations of Faraday waves in x direction $\delta n(x, t = 272$ ms) for ^{52}Cr (left), $\delta n(x, t = 225$ ms) for ^{168}Er (middle), and $\delta n(x, t = 193$ ms) for ^{164}Dy (right) BECs with $N = 10^4$ atoms. The corresponding density profile variations are shown in Figure 5.3. Vertical blue lines represent theoretical predictions for the wave vector k_F of the Faraday waves, i.e., the variational result obtained in Section 5.1, Equation (5.32).

instance, for chromium, we count three minima over the spatial extent of 30 μm, yielding an estimate $\ell \approx 10\mu$m. Similarly, for erbium, we count 5 minima over the spatial extent of 30 μm, yielding $\ell \approx 6\mu$m, and for dysprosium, the count and the estimate are the same. Obviously, these estimates are not as precise as the Fourier analysis results, and therefore we rely on FFT spectra to systematically determine the spatial periods of Faraday waves and their functional dependencies on the contact and dipole-dipole interaction strength.

5.3 Interaction effects and properties of Faraday waves

In the previous section, we have shown how Fourier analysis can be used to calculate the spatial period of Faraday waves. Now we systematically study the interaction effects, i.e., how the contact and the dipole-dipole interaction strength affect the properties of generated density waves. First, we explore the influence of the contact interaction on the emergence time and the spatial period of Faraday waves for a fixed value of the dipole-dipole interaction strength, by varying the s-wave scattering length in the experimentally relevant regime. In laboratory this can be achieved by employing the Feshbach resonance technique, which allows to tune a_s by changing

the external magnetic field, thus changing the electronic structure of atoms and their scattering properties.

The existence of Faraday waves is a consequence of nonlinearity of the system, i.e., the presence of the contact and the dipole-dipole interaction terms in the Hamiltonian. In a linear system, described by the pure Schrödinger equation, the harmonic modulation of the trap in the radial direction would not be transferred into the longitudinal direction. Therefore, the emergence time of Faraday waves (and other types of density waves in the longitudinal direction) critically depends on the strength of interatomic interactions. However, if interaction strengths become sufficiently large, the emergence time is less sensitive to their changes. Since we are considering three species where the dipole-dipole interaction is strong in erbium and dysprosium, we can expect that the emergence time of Faraday waves significantly depends on the contact interaction strength only in chromium, where a_{dd} is small.

This is illustrated in Figure 5.7, where we see the density profile variations for chromium for three different values of a_s. Let us first note that the amplitude of density variations is much smaller in the top panel for $a_s = 60\,a_0$ than in the middle panel for $a_s = 80\,a_0$, and significantly smaller than in the bottom panel for $a_s = 150\,a_0$. This is also evident from the fact that in the top and middle panel we can clearly see the quadrupole collective oscillation mode, which has a frequency of around $\omega_Q = 12 \times 2\pi$ Hz. This can be estimated from the figure and compared to the value obtained in Section 4.2 for chromium, Figure 4.2. When the interaction is sufficiently large, the amplitude of Faraday waves is much larger than those of the collective modes, and they cannot be even discerned in the bottom panel in Figure 5.7. Only for weak interactions the amplitude of the Faraday waves is comparable to the amplitude of the collective modes, and this is the reason why we can see them all for small values of a_s.

Like all other excitations, Faraday waves start to develop immediately after the modulation is switched on. The question on their emergence time is related to their amplitude, which is time-dependent and grows exponentially, as can be seen from the solution (5.23) of the Mathieu-like equation that describes the dynamics of the

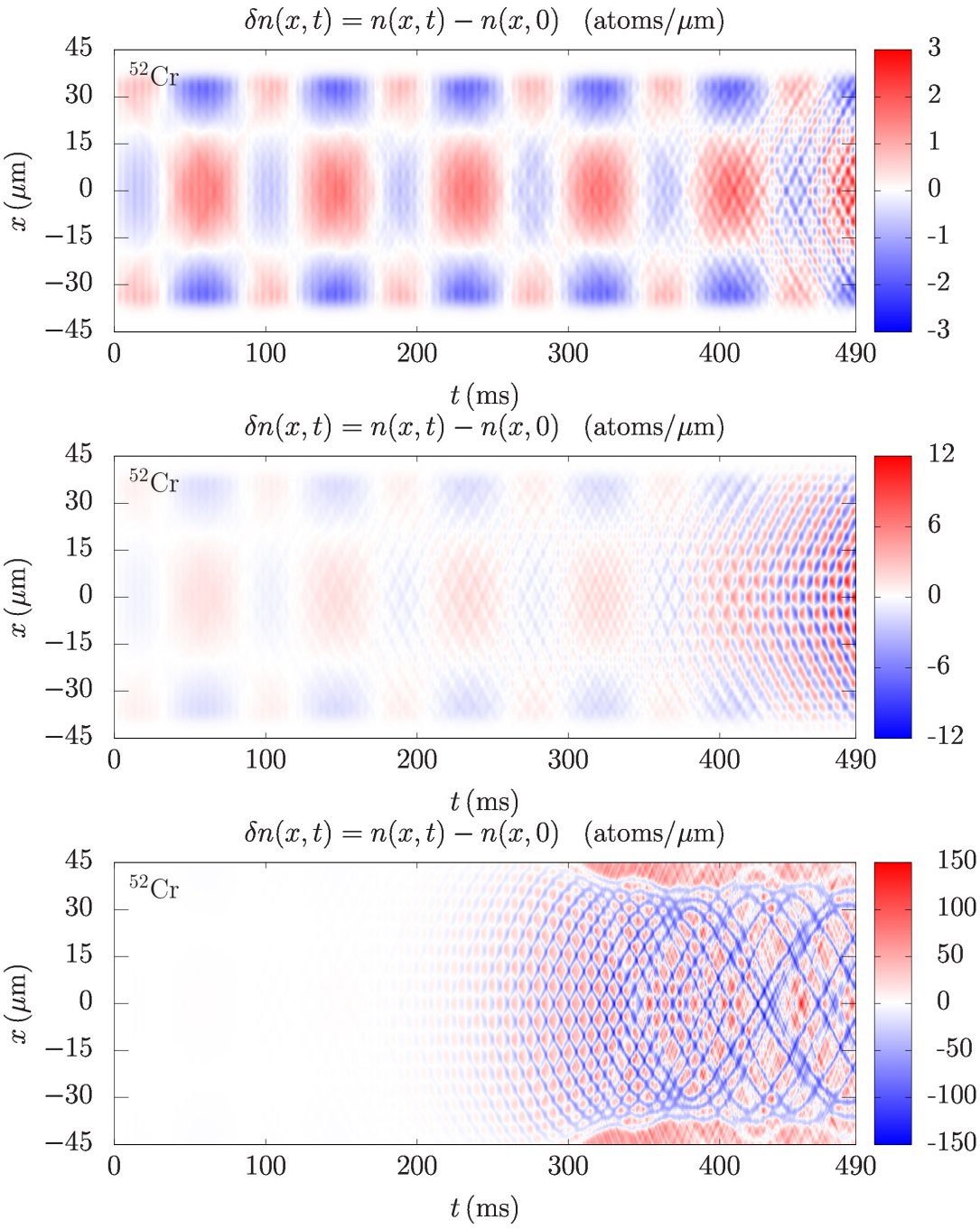

Figure 5.7: Emergence of Faraday waves for different strengths of the contact interaction: $a_s = 60\,a_0$ (top), $a_s = 80\,a_0$ (middle), and $a_s = 150\,a_0$ (bottom) for a BEC of $N = 10^4$ atoms of ^{52}Cr. From these integrated 1D density profile variations $\delta n(x,t)$, obtained for a fixed value of the dipole-dipole interaction strength given in Appendix D, we observe that Faraday waves emerge faster as the contact interaction strength increases.

Faraday density oscillations. The imaginary part of the parameter ξ in Equation (5.23) is responsible for the exponential growth of the Faraday waves' amplitude, which is not the case for collective modes. Therefore, in practical terms, the definition of the emergence time of Faraday waves is always arbitrary and can be expressed as a time needed for the density variations to reach a certain absolute or relative (compared to the total density) value. One can even relate this to the experimental point of view, where there is a threshold for the density variations that can be observed, due to measurement errors. However, in numerical simulations there are no such limitations and one can easily use an arbitrary definition to estimate the emergence time of density waves. The more relevant quantity to study would be the exponent that governs the growth of the wave amplitude, which depends on the interaction strength.

Now we turn our attention to spatial features of the Faraday waves. Figure 5.8 presents the dependence of the wave vector k_F on the s-wave scattering length a_s for all three considered species. We also show the variational results for the dependence $k_F(a_s)$ derived in Section 5.1. The agreement is very good, with errors of the order of 10 - 15 %. We stress that the derived variational expression closely follows the numerical results not only by their values, but, even more importantly, it follows their functional dependence properly.

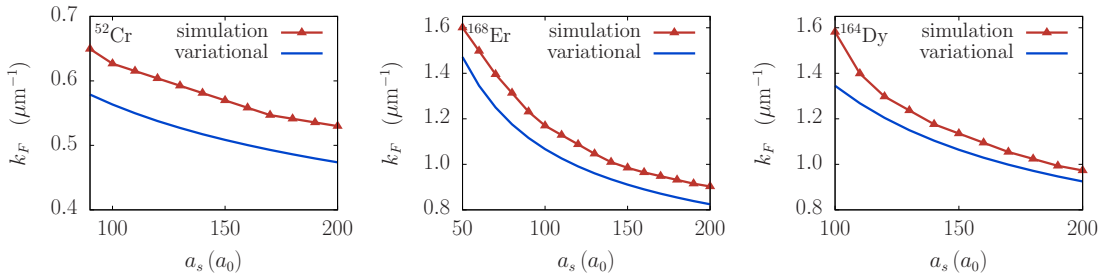

Figure 5.8: Wave vector of the Faraday waves k_F as a function of the contact interaction strength for a BEC of $N = 10^4$ atoms of ^{52}Cr (left), ^{168}Er (middle), and ^{164}Dy (right), for a fixed dipole-dipole interaction strength given in Appendix D. Red upper triangles are numerically obtained values using the FFT analysis as in Figure 5.6, and blue lines are the variational results according to Equation (5.32).

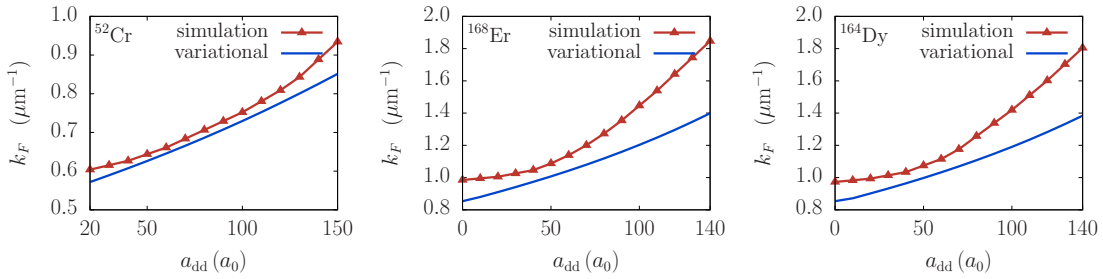

Figure 5.9: Wave vector of the Faraday waves k_F as a function of the dipole-dipole interaction strength for a BEC of $N = 10^4$ atoms of ^{52}Cr (left), ^{168}Er (middle), and ^{164}Dy (right), for a fixed contact interaction strength given in Appendix D. Red upper triangles represent numerically obtained values using the FFT analysis as in Figure 5.6, and blue lines are the variational results according to Equation (5.32).

Next, we study the effects of the dipole-dipole interaction strength for a fixed value of the contact interaction. Figure 5.9 shows the corresponding dependence of k_F on a_{dd}. In contrast to the contact interaction dependence, where k_F was a decreasing function of a_s, here we see that k_F increases as the dipole-dipole interaction strength is increased. Figure 5.9 also shows the variational results, where the level of agreement with the numerically obtained results is different, with errors as small as 7 % for chromium up to around 25 % for erbium and dysprosium for largest values of a_{dd}. Due to complex approximations made in the derivation of variational results, in particular those related to the dipole-dipole interaction term, the obtained functional dependence is not as good as in the case of contact interaction, but still provides reasonable estimates of the wave vector values for the Faraday waves.

5.4 Resonant waves

In the presence of interactions various excitation modes in dipolar BECs are coupled and the energy pumped into the system by periodic driving can be transferred from the driving direction to other, orthogonal directions. In the previous section, we have seen this for non-resonant driving, when the harmonic modulation in the radial direction was transferred to the longitudinal direction in the form of Faraday waves, which were the main excitation mode generated. The main distinguishing property

of these excitations is halving of the oscillation frequency, i.e., the induced density waves have the frequency $\omega_m/2$. Here we study the other important case, when the modulation frequency is resonant, such that the induced density waves have the same frequency. This happens when ω_m is close to one of the characteristic frequencies of the system, e.g., one of the frequencies of the collective oscillation modes or one of the trap frequencies. Although Faraday waves and all other collective oscillation modes are also excited in this case, the largest amplitude corresponds to resonant waves with the frequency ω_m. When generated, these resonant waves dominate the behavior of the system and make all other excitations negligible for the dynamics.

Figure 5.10 shows the integrated density profile variation of ^{168}Er for a resonant wave induced by a harmonic modulation of the radial part of the trapping potential at $\omega_m = \omega_y = \omega_z$, i.e., when the modulation frequency coincides with the radial trapping frequency. In this case, the density waves develop much faster than for non-resonant modulation and are clearly visible already after 55 ms. Due to a vi-

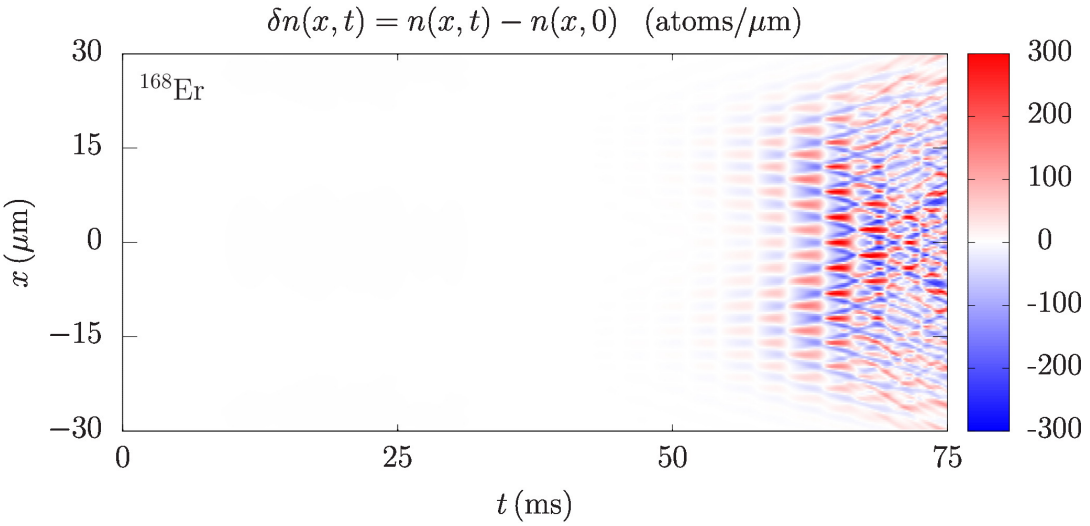

Figure 5.10: Time evolution of the integrated density profile variation in the weak confinement direction for a BEC of $N = 10^4$ atoms of erbium ^{168}Er. The parameters of the system are given in Appendix D, and the modulation frequency used is equal to the weak confinement frequency, $\omega_m = 160.5 \times 2\pi$ Hz $= \omega_y = \omega_z$. We observe resonant behavior corresponding to the first harmonic of the resonant frequency $\omega_y = \omega_z$, which sets in after around 55 ms.

olent dynamics that emerges in the system very fast, it is not easy to estimate the frequency of the waves directly from Figure 5.10, as was possible before. Therefore, we rely on the Fourier analysis in the time-frequency domain, presented in the left panel of Figure 5.11. The obtained FFT spectrum clearly shows that the main excitation mode has a frequency equal to ω_m. We also see that the spectrum is continuous, practically without distinct individual peaks, and only the second harmonic at $2\omega_m = 321 \times 2\pi$ Hz yields a small local maximum. This demonstrates that the system is far from the regime of small perturbations, where individual excitation modes can be observed.

In the right panel of Figure 5.11 we see the Fourier spectrum in the spatial-frequency domain, which yields the wave factor k_R of resonant waves. The FFT results give the value $k_R = 1.59\,\mu\text{m}^{-1}$ and the corresponding spatial period $\ell = 2\pi/k_R = 3.95\,\mu\text{m}$ for ^{168}Er. In the figure we also present the variational result $k_R = 1.40\,\mu\text{m}^{-1}$, calculated using Equation (5.33). The agreement is again quite

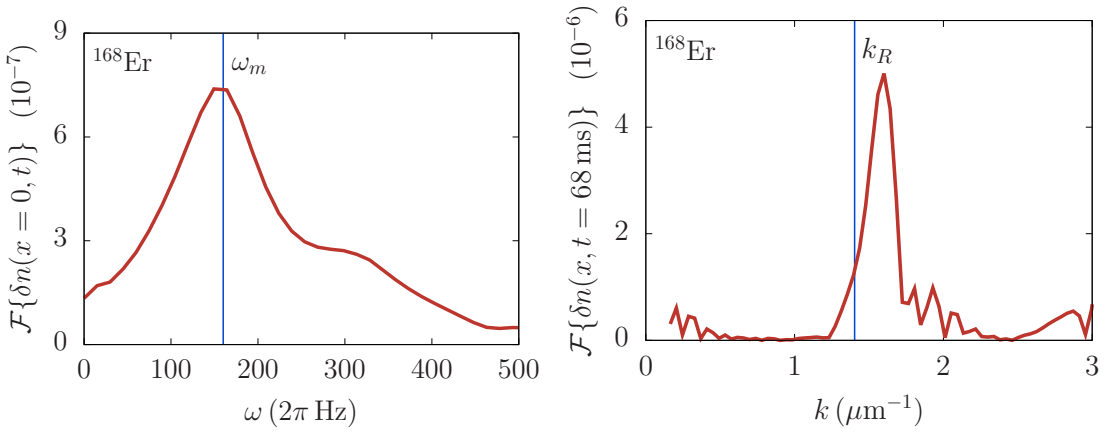

Figure 5.11: The Fourier spectrum of the integrated 1D density profile variations $\delta n(x,t)$ at the trap center in the time-frequency domain (left), and of the density profile variations in x direction $\delta n(x,\, t = 68$ ms) in the spatial-frequency domain (right) of resonant waves for a BEC of $N = 10^4$ atoms of ^{168}Er for the same parameters as in Figure 5.10. The vertical blue line in the left panel represents the modulation frequency ω_m, while in the right panel it corresponds to the theoretical prediction for the wave vector k_R of the resonant waves derived in Section 5.1, Equation (5.33).

good, which indicates that the variational approach we developed in this thesis can be reliably used not only for the Faraday waves, but also for the resonant waves.

This can also be concluded from Figure 5.12, which presents the results for the dependence of the resonant wave vector k_R on the contact and dipole-dipole interaction strength. The agreement between the numerical and variational results is of the order of 10 % over the whole experimentally relevant domain. We see similar behavior for the resonant waves as for the Faraday ones, namely the wave vector decreases as the contact interaction strength increases, while the opposite is true for the dipole-dipole interaction. Again the functional dependence obtained from the variational approach properly describes the numerical results, thus confirming that Equation (5.33) can be used to calculate the spatial period of resonant waves.

It is interesting to note that resonant behavior appears not only under the conditions mentioned above, when ω_m is equal to one of the characteristic frequencies, but also when it matches their higher harmonics. Figure 5.13 illustrates this for ^{168}Er, which is harmonically modulated at twice the radial trapping frequency,

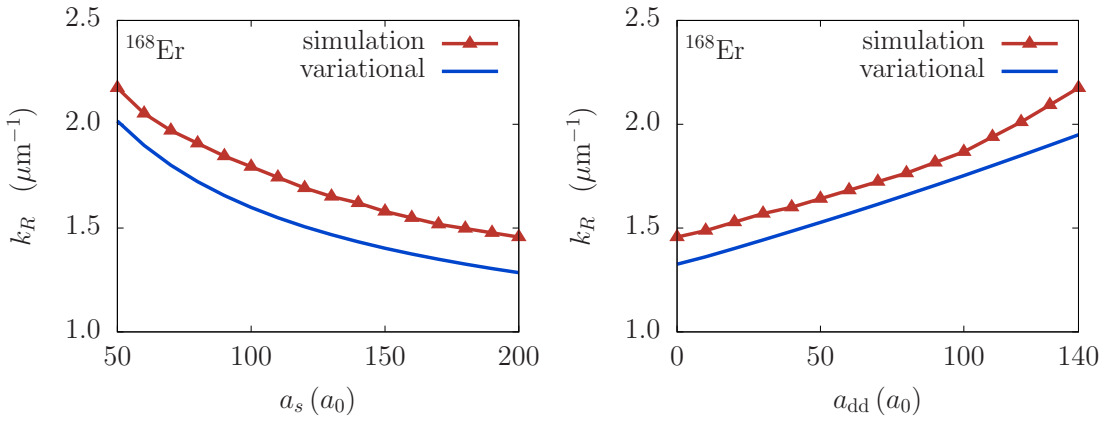

Figure 5.12: Wave vector of the resonant waves k_R as a function of the contact (left) and dipole-dipole (right) interaction strength for a BEC of $N = 10^4$ atoms of ^{168}Er. The results in the left panel are obtained for a fixed dipole-dipole interaction strength given in Appendix D, and similarly, in the right panel, a fixed contact interaction strength from Appendix D is used. In both panels, red upper triangles represent numerically obtained values using the FFT analysis as in the right panel of Figure 5.11, and blue lines are the variational results according to Equation (5.33).

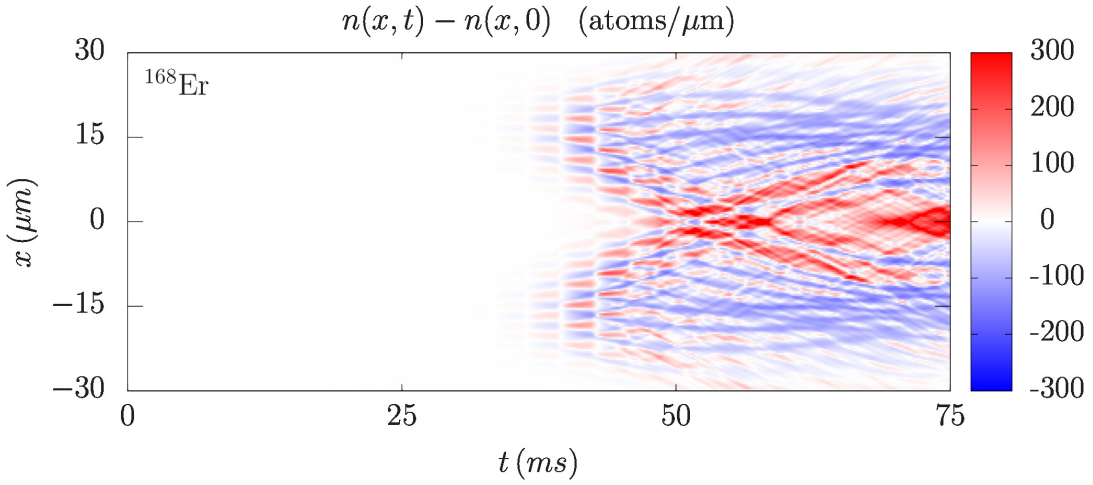

Figure 5.13: Time evolution of the integrated density profile variation in the weak confinement direction for a BEC of $N = 10^4$ atoms of erbium ^{168}Er. The parameters of the system are given in Appendix D, and the modulation frequency used is equal to twice the weak confinement frequency, $\omega_m = 321 \times 2\pi$ Hz $= 2\,\omega_y$. We observe resonant behavior corresponding to the second harmonic of the resonant frequency $\omega_y = \omega_z$, which sets in faster than the first harmonic, already after around 30 ms.

$\omega_m = 321 \times 2\pi$ Hz. In this case, the amplitude of the resonant mode grows even faster and significant density variations can be observed already after 30 ms. Therefore, we see that the modulation at the second harmonic yields even more violent dynamics than the first harmonic. The Fourier analysis in the time-frequency domain reveals that the main excitation mode again has a frequency of $160.5 \times 2\pi$ Hz, but the mode at $\omega_m = 321 \times 2\pi$ Hz is also present. From the experimental point of view, resonant driving is very dangerous and leads to the destruction of the system in a matter of tens of milliseconds. While numerical simulations can be performed for longer time periods, the atoms leave the condensate due to a large, resonant transfer of energy to the system. As the condensate is depleted, the mean-field description of the system breaks down and it cannot be anymore simulated by the dipolar GPE.

6 Algorithm for solving the dipolar GPE

The existence of nonlinear terms in equations describing various physical systems is usually a source of novel phenomena. However, their understanding requires detailed and careful analysis, mainly because we can no longer rely on our intuition based on linear equations and instinctively predict the evolution of the system. From the experimental point of view, the analysis requires development and fine-tuning of new methods that focus on particular phenomena in the condensate. On the other hand, it is often necessary to establish or further develop an analytical or numerical method to solve the corresponding set of equations, usually a set of nonlinear partial differential equations. In the case of a BEC with dipole-dipole interaction, we mostly rely on the dipolar GPE.

A wide range of different numerical methods was developed in the literature. Some of them are focused on the calculation of the ground state properties [83–86], while others focus on the dynamics of the time-dependent GPE [87–95]. Also, there are several methods able to calculate a numerical solution both for the ground state and non-stationary dynamics of a BEC [87–95]. These methods can be divided into several categories: finite difference, split-step, and spectral methods.

A finite difference method approximates the spatial and time derivatives with finite differences, up to the desired order of accuracy, which is derived from the Taylor series expansion. This approach introduces discretization of space and time, with the time step denoted by Δt, and the space step denoted by Δh. Note that the space discretization step can be different in different directions, in which case

we denote the corresponding steps by Δh_j, where $j = 1, 2, 3$. When dealing with dipolar GPE, such discretization is usually implemented using a forward, backward, or central difference scheme in time and a second-order central difference scheme for space derivatives. An algorithm that implements a forward difference scheme in time is known as an explicit method, a backward difference approach yields an implicit method, and a central difference approach in time is a combination of the two, and is designated as a semi-implicit algorithm, or the Crank–Nicolson semi-implicit algorithm [35–37]. In its usual form, it introduces a quadratic error in the calculation in the discretization steps, $\mathcal{O}(\Delta t^2) + \mathcal{O}(\Delta h^2)$, both in the time and the space steps. The fact that we are using a semi-implicit algorithm, i.e., that the space derivatives are expressed as averages of their finite difference approximations in the present and future time step, makes the Crank-Nicolson scheme unconditionally stable [36, 37]. We have used this method in all our implementations.

The split-step method relies on the splitting of the time evolution in each time step into several sub-steps, which corresponds to splitting the Hamiltonian that governance system's dynamics into several parts, and then evolving the wave function independently with respect to each of them. This method is usually combined with the finite difference method, and practically realized by splitting the Hamiltonian $\hat{H} = \hat{T} + \hat{V}$ into the kinetic energy part $\hat{T}$ and the potential energy part $\hat{V}$, which includes the trap potential and nonlinear terms corresponding to the contact and the dipole-dipole interaction. In order to implement the splitting of the Hamiltonian and calculate the time evolution of the system we use the Baker-Campbell-Hausdorff lemma [96]

$$e^{\Delta t(\hat{\mathcal{O}}_1+\hat{\mathcal{O}}_2)} = e^{\Delta t\hat{\mathcal{O}}_1}\, e^{\Delta t\hat{\mathcal{O}}_2}\, e^{-\frac{\Delta t^2}{2}[\hat{\mathcal{O}}_1,\hat{\mathcal{O}}_2]} e^{\frac{\Delta t^3}{6}(2[\hat{\mathcal{O}}_2,[\hat{\mathcal{O}}_1,\hat{\mathcal{O}}_2]]+[\hat{\mathcal{O}}_1,[\hat{\mathcal{O}}_1,\hat{\mathcal{O}}_2]])} \ldots \tag{6.1}$$

The above form of the lemma, know as the Zassenhaus formula [97], expresses the exponential of the sum of two operators $\hat{\mathcal{O}}_1$ and $\hat{\mathcal{O}}_2$, that do not commute in general, by a product of their individual exponentials and higher-order terms that contain quadratic and higher orders of the parameter Δt. If the parameter Δt is small we can neglect these higher-order terms and use the splitting formula which, for the

case of the time evolution of the Hamiltonian $\hat{H} = \hat{T} + \hat{V}$ reads

$$e^{-\frac{i}{\hbar}\hat{H}\Delta t} = e^{-\frac{i}{\hbar}\left(\hat{T}+\hat{V}\right)\Delta t} = e^{-\frac{i}{\hbar}\hat{T}\Delta t}\, e^{-\frac{i}{\hbar}\hat{V}\Delta t} + \mathcal{O}(\Delta t^2)\,. \tag{6.2}$$

In this way, we make the error of the same order as the one due to the finite difference scheme used to approximate time derivatives. In principle, we can go to higher orders in the Zassenhaus formula, but this would be numerically very time-consuming. It would also have to be accompanied by a higher order of approximation for the time derivative. The numerical complexity of such a method would be even higher due to this and therefore is rarely used. One can achieve the desired accuracy of the calculation by using smaller values of the discretization steps. In addition to split-step methods there are also other, direct methods for solving the GPE (or, in general, partial differential equations) such as Euler or Runge-Kutta [98], where time evolution is done in one step, avoiding the Hamiltonian division altogether.

Spectral methods rely on expressing the solution of the GPE in an appropriately chosen basis as a linear combination of orthonormal special functions. In this case, the original equation is rewritten as a set of equations for the corresponding coefficients of the wave function expansion in the selected basis. For instance, if we use the plane-wave basis we get the most common spectral decomposition of the wave function. The kinetic energy part and the potential energy part of the Hamiltonian are diagonal in the k-space and in the real space, respectively, and forward and backward Fourier transformation enables us to compute the evolution with respect to the corresponding part of the Hamiltonian. Note that the spectral methods also belong to the category of split-step approaches and use the Zassenhaus approximation (6.2).

Our numerical algorithm to solve the GPE combines the split-step approach with the semi-implicit Crank-Nicolson method [35–37]. The ground state of the system is calculated using propagation in the imaginary-time [84–86] starting from an arbitrary initial state, while the system's dynamics is obtained using the real-time propagation from a given initial wave function. Our programs that practically

implement the algorithm solve the dimensionally reduced form of the GPE

$$i\,\frac{\partial\psi(\mathbf{r},t)}{\partial t} = \Bigg[-\frac{1}{2}\nabla^2 + U(\mathbf{r},t) + 4\pi N a_s\,|\psi(\mathbf{r},t)|^2 + 3N a_{\rm dd}\int d\mathbf{r}'\,U_{\rm dd}(\mathbf{r}-\mathbf{r}')\,|\psi(\mathbf{r}',t)|^2\Bigg]\psi(\mathbf{r},t)\,. \tag{6.3}$$

Equation (6.3) is derived from the dimensional GPE (2.45) by choosing a reference frequency ω_r, and by expressing all other physical variables in units defined using this frequency

$$\begin{aligned} &x \to \frac{x}{l}\,,\quad y \to \frac{y}{l}\,,\quad z \to \frac{z}{l}\,,\quad a_s \to \frac{a_s}{l}\,,\quad a_{\rm dd} \to \frac{a_{\rm dd}}{l},\quad t \to \omega_r t\,,\\ &\psi(\mathbf{r},t) \to l^{3/2}\,\psi(\mathbf{r},t)\,,\quad U(\mathbf{r},t) \to \frac{1}{\hbar\omega_r}U(\mathbf{r},t)\,,\quad U_{\rm dd}(\mathbf{r},t) \to \frac{1}{\hbar\omega_r}U_{\rm dd}(\mathbf{r},t)\,. \end{aligned} \tag{6.4}$$

Here the unit of length l is harmonic oscillator length $l = \sqrt{\hbar/(m\omega_{\rm r})}$ for the frequency $\omega_{\rm r}$ and the mass m of the atoms in the condensate. In order to transform the numerical results obtained in simulations to the physical units, one has to perform the inverse rescaling.

As a result of this, the trapping potential $U(\mathbf{r},t)$ is transformed into a dimensionless form

$$U(\mathbf{r},t) = \frac{1}{2}\left(\gamma^2x^2 + \nu^2y^2 + \lambda^2z^2\right)\,, \tag{6.5}$$

where $\gamma = \omega_x/\omega_{\rm r}$, $\nu = \omega_y/\omega_{\rm r}$, and $\lambda = \omega_z/\omega_{\rm r}$ are the trap aspect ratios. For practical reasons, we usually set one of the trap frequencies as the referent $\omega_{\rm r}$. Another convenient choice is the geometric mean of the trap frequencies, $\omega_{\rm r} = (\omega_x\omega_y\omega_z)^{1/3}$. Our programs allow to use all three trap aspect ratios independently, but in our simulations, with the cigar-shaped condensates along the x-axis, we choose $\omega_{\rm r} = \omega_y = \omega_z$, so that the trap aspect ratios ν and λ are equal to 1.

6.1 Split-step semi-implicit Crank-Nicolson method

The split-step semi-implicit Crank-Nicolson method introduces the discretization of time and spatial coordinates. The total time of simulation T is discretized into N equal sub-steps $\Delta t = T/N$. The simulation is performed in three spatial dimensions, and we introduce a spatial mesh with N_x, N_y, and N_z equidistant points in x, y, and z

direction, respectively. The corresponding spatial extents of the system (simulation box sizes) are $L_x = N_x\,\Delta x$, $L_y = N_y\,\Delta y$, and $L_z = N_z\,\Delta z$, where Δx, Δy, and Δz are the discretization steps. It is customary to place the coordinate system in the center of the simulation box, such that the coordinates x, y, and z take values from the intervals $[-L_x/2, L_x/2]$, $[-L_y/2, L_y/2]$, and $[-L_z/2, L_z/2]$, respectively.

During the small evolution time Δt, the split-step approach of the algorithm divides the Hamiltonian into the non-derivative ($\hat{H}_0$) and derivative ($\hat{H}_1$, $\hat{H}_2$, $\hat{H}_3$) parts, as follows

$$\hat{H}_0 = U(\mathbf{r};t) + 4\pi N a_s\,|\psi(\mathbf{r};t)|^2 + 3N a_{\rm dd}\int d\mathbf{r}'\,U_{\rm dd}(\mathbf{r}-\mathbf{r}';t)\,|\psi(\mathbf{r}';t)|^2\,, \tag{6.6}$$

$$\hat{H}_1 = \frac{\partial^2}{\partial x^2}\,, \quad \hat{H}_2 = \frac{\partial^2}{\partial y^2}\,, \quad \hat{H}_3 = \frac{\partial^2}{\partial z^2}\,, \tag{6.7}$$

where the Laplacian is split into three parts. Therefore, the initial dipolar GPE given by equation (6.3) transforms into four sequential partial differential equations,

$$i\,\frac{\partial\psi(\mathbf{r};t)}{\partial t} = \hat{H}_j\,\psi(\mathbf{r};t)\,, \quad j = 0,1,2,3\,, \tag{6.8}$$

which are solved one after the other in the algorithm.

Starting from a preceding solution $\psi^n(\mathbf{r})$, obtained in the previous complete time step, the time evolution with respect to $\hat{H}_0$ in the current time step yields an intermediate solution $\psi^{n+1/4}(\mathbf{r})$ of equation (6.8) for $j = 0$. The superscript $1/4$ denotes that this is a first of four sub-steps in the current time iteration. Since $\hat{H}_0$ has no derivatives, it is diagonal in real space and the solution can be written exactly as

$$\psi^{n+1/4}(\mathbf{r}) = e^{-i\hat{H}_0\Delta t}\,\psi^n(\mathbf{r}) \equiv \hat{\mathcal{P}}(\hat{H}_0)\,\psi^n(\mathbf{r})\,. \tag{6.9}$$

From this intermediate solution, using the semi-implicit Crank-Nicolson scheme, the time propagation of the wave function continues and is calculated by solving the

series of partial differential equations,

$$i\,\frac{\psi^{n+2/4}(\mathbf{r})-\psi^{n+1/4}(\mathbf{r})}{\Delta t}=\frac{1}{2}\,\hat{H}_1\left[\psi^{n+2/4}(\mathbf{r})+\psi^{n+1/4}(\mathbf{r})\right]\,, \tag{6.10}$$

$$i\,\frac{\psi^{n+3/4}(\mathbf{r})-\psi^{n+2/4}(\mathbf{r})}{\Delta t}=\frac{1}{2}\,\hat{H}_2\left[\psi^{n+3/4}(\mathbf{r})+\psi^{n+2/4}(\mathbf{r})\right]\,, \tag{6.11}$$

$$i\,\frac{\psi^{n+1}(\mathbf{r})-\psi^{n+3/4}(\mathbf{r})}{\Delta t}=\frac{1}{2}\,\hat{H}_3\left[\psi^{n+1}(\mathbf{r})+\psi^{n+3/4}(\mathbf{r})\right]\,. \tag{6.12}$$

On the left-hand side, partial derivatives in time are estimated by a two-point formula, and on the right-side, the wave function is averaged over the current and the future time sub-step, which is a characteristic for the finite-difference semi-implicit Crank–Nicolson method. Equations (6.10) - (6.12) have a formal solution that propagates the wave function to the next intermediate solution,

$$\psi^{n+2/4}(\mathbf{r})=\frac{1-i\hat{H}_1\Delta t/2}{1+i\hat{H}_1\Delta t/2}\,\psi^{n+1/4}(\mathbf{r})\equiv\hat{\mathcal{P}}(\hat{H}_1)\,\psi^{n+1/4}(\mathbf{r})\,, \tag{6.13}$$

$$\psi^{n+3/4}(\mathbf{r})=\frac{1-i\hat{H}_2\Delta t/2}{1+i\hat{H}_2\Delta t/2}\,\psi^{n+2/4}(\mathbf{r})\equiv\hat{\mathcal{P}}(\hat{H}_2)\,\psi^{n+2/4}(\mathbf{r})\,, \tag{6.14}$$

$$\psi^{n+1}(\mathbf{r})=\frac{1-i\hat{H}_3\Delta t/2}{1+i\hat{H}_3\Delta t/2}\,\psi^{n+3/4}(\mathbf{r})\equiv\hat{\mathcal{P}}(\hat{H}_3)\,\psi^{n+3/4}(\mathbf{r})\,. \tag{6.15}$$

The numerical algorithm for solving the above equations is worked out in Appendix E. Let us denote by $\psi_i^{n+j/4}$ the wave function value in the current time iteration after sub-step j and at the position i in the mesh in the corresponding spatial direction. The algorithm determines the wave function by a recursive relation

$$\psi_{i+1}^{n+(j+1)/4}=\alpha_i^j\psi_i^{n+(j+1)/4}+\beta_i^{n+j/4}\,, \tag{6.16}$$

for $j=1,2,3$, where j corresponds to spatial direction x, y, and z direction, respectively. The coefficients α_i^j and $\beta_i^{n+j/4}$ are defined via backward recursion relations

$$\alpha_{i-1}^j=\gamma_i^j A_j^-\,, \tag{6.17}$$

$$\beta_{i-1}^{n+j/4}=\gamma_i^j\left(A_j^+\beta_i^{n+j/4}-B_i^{n+j/4}\right)\,, \tag{6.18}$$

where coefficients γ_i^j, A_j^-, A_j^+, A_j^0, and $B_i^{n+j/4}$ are defined by relations

$$A_j^-=A_j^+=-\frac{\Delta t}{4\Delta h_j^2}\,,\quad A_j^0=1+i\,\frac{\Delta t}{2\Delta h_j^2}\,, \tag{6.19}$$

$$B_i^{n+j/4}=i\,\frac{\Delta t}{4\Delta h_j^2}\left(\psi_{i+1}^{n+j/4}-2\psi_i^{n+j/4}+\psi_{i-1}^{n+j/4}\right)+\psi_i^{n+j/4}\,, \tag{6.20}$$

where Δh_j denote spatial mesh step in Δx, Δy, and Δz direction for $j = 1, 2, 3$, respectively. The above backward recursion expresses the coefficients $B_i^{n+j/4}$ explicitly in terms of the wave function in the previous sub-step, thus disentangling the semi-implicit form of equations (6.10) - (6.12). From the technical point of view, we see that the coefficients $A_j^{\pm}$, A_j^0, α_i^j, and γ_i^j do not depend on the wave function (i.e., on the time step n), and therefore can be calculated before the time loop in a particular simulation. In other words, these coefficients depend only on the discretization parameters. Within the main time loop, only coefficients $\beta_i^{n+j/4}$ have to be recalculated in each sub-step.

6.2 Dipole-dipole interaction

While the calculation of the potential and nonlinear contact interaction term within the non-derivative part of the Hamiltonian ($\hat{H}_0$) of equation (6.8) for $j = 0$ is straightforward, the calculation of the nonlinear term corresponding to the dipole-dipole interaction at each mesh point introduces additional convolution integral. The integral can be easily solved by moving to the Fourier space, i.e., by treating the dipole-dipole interaction term in momentum space as

$$\int d\mathbf{r}'\, U_{\mathrm{dd}}(\mathbf{r}-\mathbf{r}')\,|\psi(\mathbf{r}')|^2 = \mathcal{F}^{-1}\left\{\mathcal{F}\left[U_{\mathrm{dd}}\right](\mathbf{k})\,\mathcal{F}\left[|\psi|^2\right](\mathbf{k})\right\}(\mathbf{r})\,, \tag{6.21}$$

where $\mathcal{F}$ represents Fourier transform and $\mathcal{F}^{-1}$ inverse Fourier transform, defined respectively by

$$\mathcal{F}[f](\mathbf{k}) = \tilde{f}(\mathbf{k}) = \int d\mathbf{r}\, f(\mathbf{r})\, e^{-i\,\mathbf{k}\cdot\mathbf{r}}\,, \tag{6.22}$$

$$\mathcal{F}^{-1}[\tilde{f}](\mathbf{r}) = f(\mathbf{r}) = \frac{1}{(2\pi)^3}\int d\mathbf{k}\, \tilde{f}(\mathbf{k})\, e^{i\,\mathbf{k}\cdot\mathbf{r}}\,. \tag{6.23}$$

Implementation of the algorithm uses Fast Fourier transform (FFT) for calculation of Fourier transform of the density of wave function, while the Fourier transform of the dipole potential is calculated analytically in Appendix A, yielding

$$\mathcal{F}[U_{\mathrm{dd}}](\mathbf{k}) = \frac{4\pi}{3}\left(3\cos^2\theta - 1\right) = \frac{4\pi}{3}\left(\frac{3\,k_z^2}{\mathbf{k}^2} - 1\right)\,, \tag{6.24}$$

where θ is the angle between the orientation of dipoles and vector $\mathbf{k}$, i.e., in our setup, angle between z direction and vector $\mathbf{k}$. Within the same time step, orientations are constant, so the transformation is performed once per time step Δt. The Fourier transform of density $|\psi(\mathbf{r})|^2$ and inverse Fourier transform is evaluated numerically by using a standard FFT algorithm. The FFT algorithm is carried out in Cartesian coordinates, and the GPE is solved in 3D irrespective of the symmetry of the trapping potential.

Successful implementation of the split-step Crank-Nicolson method using Fourier transformation has to ensure that the wave function and the interaction term disappear at the boundary of the discretization mesh. For the Fourier transform of the long-range dipolar potential, this is not true, and equation (6.24) is undefined at the origin in k-space, i.e., at boundaries in coordinate space. Since the same domain is used for Fourier and inverse Fourier transform in treating the dipolar potential, cutting off the k-space origin will affect the space domain. Thus, boundary effects can play a role when finding the Fourier transform, and a sufficiently large space domain has to be used to have accurate values of the Fourier transform involving the long-range dipolar potential. Inspired by equation (A.10), it was suggested [99] that this could be avoided by truncating the dipolar interaction conveniently at large distances $r = R$ so that it does not affect the boundary, provided R is taken to be larger than the size of the condensate. Then the truncated dipolar potential will cover the whole condensate wave function and will have a continuous Fourier transform at the origin. This improves the accuracy of a calculation using a small space domain. The Fourier transform of the dipolar potential truncated at $r = R$ is used in our implementation of the algorithm for solving dipolar GPE as

$$\tilde{U}_{\rm dd}(\mathbf{k}) = \frac{4\pi}{3}\left(\frac{3\,k_z^2}{\mathbf{k}^2} - 1\right)\left[1 + 3\,\frac{\cos(kR)}{k^2R^2} - 3\,\frac{\sin(kR)}{k^3R^3}\right]. \tag{6.25}$$

The difficulty in using a large space domain is the most severe in 3D algorithms for solving dipolar GPE by the split-step Crank-Nicolson method. The cut-off parameter R of equation (6.25) improves the accuracy of the calculation.

6.3 Calculation of physical quantities

During the evolution of the system, the relevant physical quantities can be calculated using the obtained time-dependent wave function. Since the wave function is obtained with the time resolution of Δt, we can calculate all physical quantities with the same time resolution or choose to calculate them less frequently, to decrease the computation time. Here we list the expectation values calculated by our programs by default.

The size of the system in x, y, and z direction is expressed by the root-mean-square of the corresponding coordinate,

$$x_{\mathrm{rms}} = \sqrt{\langle x^2 \rangle}\,, \quad \langle x^2 \rangle = \int d\mathbf{r}\, x^2\, |\psi(\mathbf{r})|^2\,, \tag{6.26}$$

$$y_{\mathrm{rms}} = \sqrt{\langle y^2 \rangle}\,, \quad \langle y^2 \rangle = \int d\mathbf{r}\, y^2\, |\psi(\mathbf{r})|^2\,, \tag{6.27}$$

$$z_{\mathrm{rms}} = \sqrt{\langle z^2 \rangle}\,, \quad \langle z^2 \rangle = \int d\mathbf{r}\, z^2\, |\psi(\mathbf{r})|^2\,, \tag{6.28}$$

while the size of the whole system is estimated by the quadratic mean,

$$r_{\mathrm{rms}} = \sqrt{\langle x^2 \rangle + \langle y^2 \rangle + \langle z^2 \rangle}\,. \tag{6.29}$$

For stationary states, the wave function has a trivial time dependence $\psi(\mathbf{r}, t) = \psi(\mathbf{r})\, e^{-i\mu t}$, where μ is the chemical potential. If we substitute this into Equation (6.3), and multiply it by $\psi^*(\mathbf{r})$, taking into account that the wave function is normalized to 1, we obtain the following formula for the chemical potential

$$\begin{aligned} \mu = \int d\mathbf{r} \Bigg[\frac{1}{2} |\nabla\psi(\mathbf{r})|^2 + U(\mathbf{r})\, |\psi(\mathbf{r})|^2 + 4\pi N a_s\, |\psi(\mathbf{r})|^4 \\ + 3N a_{\mathrm{dd}} \int d\mathbf{r}'\, U_{\mathrm{dd}}(\mathbf{r} - \mathbf{r}')\, |\psi(\mathbf{r}')|^2\, |\psi(\mathbf{r})|^2 \Bigg]\,. \end{aligned} \tag{6.30}$$

The above expression can be also used for non-stationary states, to obtain the expectation values of the Hamiltonian.

The following expression for the energy E is obtained by multiplying the inter-

action terms by 1/2 in equation (6.30)

$$E = \int d\mathbf{r} \left[\frac{1}{2} |\nabla\psi(\mathbf{r})|^2 + U(\mathbf{r}) |\psi(\mathbf{r})|^2 + 2\pi N a_s |\psi(\mathbf{r})|^4 + \frac{3}{2} N a_{\mathrm{dd}} \int d\mathbf{r}' \, U_{\mathrm{dd}}(\mathbf{r} - \mathbf{r}') |\psi(\mathbf{r}')|^2 |\psi(\mathbf{r})|^2 \right] . \tag{6.31}$$

In a variational approach, the GPE can be obtained by minimizing the above functional with respect to the wave function.

The norm of the wave function is calculated by definition

$$\int d\mathbf{r} \ |\psi(\mathbf{r})|^2 \ , \tag{6.32}$$

and in the real-time propagation, it should be always equal to 1. The Crank-Nicolson scheme conserves the normalization of the wave function, but its monitoring can be used as an early check of the validity of the simulation. However, this is not the case in imaginary-time propagation, since then the evolution operator is not unitary. Therefore, it is necessary to normalize the wave function again after each time step Δt.

6.4 Numerical integration and derivation

Numerical integration within the algorithm is implemented using Simpson's rule

$$\int dx \, f(x) \approx \frac{\Delta x}{3} \sum_{i=1}^{N/2} (f_{2i-2} + 4 f_{2i-1} + f_{2i}) \tag{6.33}$$

where N is a number of equidistant points and Δx the size of a spatial step.

In order to calculate the energy and the chemical potential we also need spatial derivatives of the wave function. For this we use the Richardson extrapolation formula of the fourth order. For instance, the spatial derivative of the wave function in direction j is approximated with

$$\frac{\partial \psi_i^n}{\partial h_j} \approx \frac{1}{12 \Delta h_j} \left(\psi_{i-2}^n - 8\psi_{i-1}^n + 8\psi_{i+1}^n - \psi_{i+2}^n \right) . \tag{6.34}$$

6.5 Algorithm wrap-up

Practical usage of the programs that implement the algorithm for solving the dipolar GPE requires the preparation of an input file that provides the parameter values of the system of interest. This includes a number of atoms in the condensate, which is typically between 10^4 and 10^6. One also has to specify a unit of length l in units of Bohr radius ($a_0 = 5.2917721092 \times 10^{-11}$ m). For a chosen reference frequency ω_r it is calculated as $l = \sqrt{\hbar/(m\omega_r)}$ for atoms with mass m, and is typically of the order of μm. Physical parameters of the system also include the s-wave scattering length a_s, which measures the contact interaction strength, and the dipolar length a_{dd}, which measures dipole-dipole interaction strength. Both are expressed in units of Bohr radius within the input file.

In addition of physical parameters, we also have to supply discretization details such as the time step Δt (in units of $1/\omega_r$) and the number of iterations N. Typical values of the time step Δt we used for our simulations was between 10^{-2} and 10^{-3}, which corresponds to $10^{-2} - 10^{-3}$ ms after re-scaling with the frequency $\omega_r = 2\pi \times 160.5$ Hz. Therefore, for the simulation of the evolution for 250 ms, the number of iterations N has to be between 2.5×10^4 and 2.5×10^5.

The spatial discretization is defined by the size of steps and the number of mesh points in x, y, and z direction. In the simulations, we have used equal numbers of mesh points in all directions, $N_x = N_y = N_z = 500$, with different step sizes, typically $\Delta x = 0.5$ and $\Delta y = \Delta z = 0.1$, due to the cigar shape of the condensate. Such mesh creates a simulation box of the volume of approximately $250 \times 50 \times 50$ μm^3.

Flowchart of the algorithm for solving the dipolar GPE is illustrated in Figure 6.1. Using the parameters specified in the configuration input file, the algorithm in the very first step generates an initial wave function or reads its values from the external file. This is represented by the operator $\hat{\mathcal{I}}$, which will initialize the wave function matrix to be propagated within the main loop of the algorithm. In the case of imaginary-time propagation, most frequently, the initial wave function will

be generated in the form of a predefined Gaussian, or if it is explicitly defined in the input file, it will be populated by the values from the external file. For real-time propagation, the initial wave function is always read from the external file. Usually, it is a wave function obtained from the previous calculation, either in imaginary- or real-time propagation.

Using the initial wave function, the algorithm in N equal time steps Δt propagates the wave function. Each time step consists of four sub-steps, which are implemented using the operators $\hat{\mathcal{P}}(\hat{H}_0)$, $\hat{\mathcal{P}}(\hat{H}_1)$, $\hat{\mathcal{P}}(\hat{H}_2)$, $\hat{\mathcal{P}}(\hat{H}_3)$. After each step, the operator $\hat{\mathcal{M}}$ calculates the relevant physical quantities. In the case of imaginary-time propagation, there is an additional operation in which we normalize the wave function to 1 using the operator $\hat{\mathcal{N}}$. After the main loop is finished, the simulation saves the wave function for further use (operator $\hat{\mathcal{E}}$).

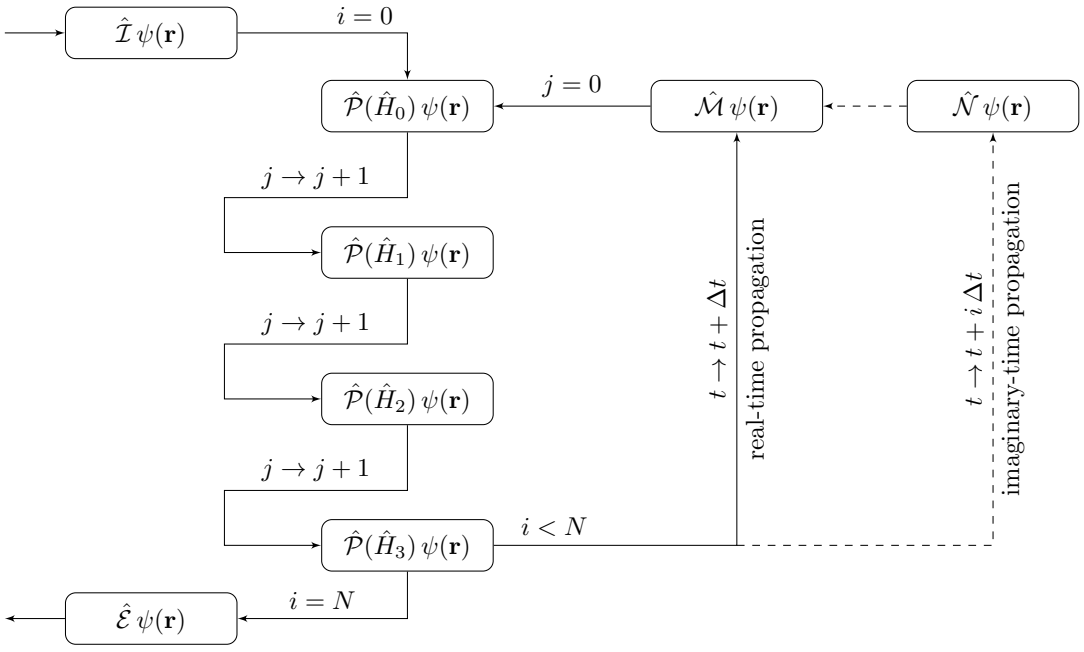

Figure 6.1: Flowchart of the algorithm for solving the dipolar GPE. The operator $\hat{\mathcal{I}}$ is responsible for the initialization of the wave function matrix. Propagation of the wave function is done in four sub-steps using operators $\hat{\mathcal{P}}(\hat{H}_0)$, $\hat{\mathcal{P}}(\hat{H}_1)$, $\hat{\mathcal{P}}(\hat{H}_2)$, $\hat{\mathcal{P}}(\hat{H}_3)$. The operator $\hat{\mathcal{M}}$ calculates physical quantities of the system, and the operator $\hat{\mathcal{E}}$ saves the wave function for further use. In the case of imaginary-time propagation, the operator $\hat{\mathcal{N}}$ normalizes the wave function.

6.6 Parallelization and optimization

The algorithm for solving fully-anisotropic three-dimensional dipolar GPE is developed based on our previous programs [88, 89]. The original program for the contact interaction GPE was written in Fortran [87] by Adhikari and Muruganandam. Later on, we have rewritten this program in the C programming language, and parallelized it using the Open Multi-Processing (OpenMP) library [90–92, 95]. Afterward, we have developed the programs that include both the contact and the dipole-dipole interaction in C and in Fortran [93, 94]. We have demonstrated excellent agreement of recent experimental observation of dipolar BECs of ^{52}Cr, ^{164}Dy, and ^{168}Er atoms with the numerical results. The programs had to be parallelized, which allows the utilization of all available processors/cores on a shared memory computer, leading to the speedup of $70 - 90\%$ of the ideal one.

Figure 6.2 illustrates the speedup (blue down triangles) and the efficiency (red up triangles) in the execution time of the imaginary-time (left panel) and real-time (right panel) propagation as a function of a number of utilized CPU cores. The speedup $S(N_c)$ is calculated as a ratio of the execution time of a simulation on a single CPU core and a simulation using N_c cores. The efficiency $E(N_c) = S(N_c)/N_c$

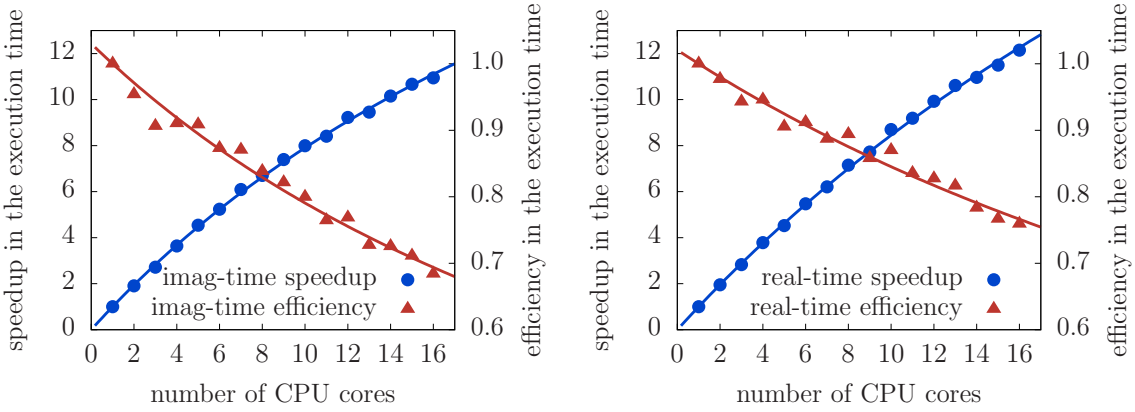

Figure 6.2: Speedup (blue down triangles) and efficiency (red up triangles) of the algorithm for solving the dipolar GPE during imaginary-time (left) and real-time (right) propagation as a function of the number of utilized CPU cores. Solid lines represent fits to measured data according to Amdahl's law.

is defined as a ratio of the speedup, measured in numerical experiments, and the idea one which is equal to N_c. In all simulations, we have used a consistent spatial mesh of the size of $500 \times 500 \times 500$. Starting from a single CPU core, we gradually increase the number of utilized cores up to 16 on an Intel Xeon CPU E5-2670 machine with a clock frequency of 2.60 GHz. The programs are compiled and optimized using the Intel compiler.

Based on Amdahl's law [100], the expected execution times of a sequential (which remains constant) and a parallelized region of the code (which scales with a number of cores N_c). If p is parallelized fraction of the code, the expected speedup is given by

$$S(N_c) = \frac{1}{(1-p) + p/N_c}, \tag{6.35}$$

and similarly for $E(N_c)$. Solid lines in Figure 6.2 represent the fits to measured data according to relation (6.35), which allows us to verify the consistency of the performance of our programs and to estimate the parallel fraction p.

Details on the testing of parallelization scaling are given in Appendix F.

7 Conclusions

This thesis explores the Faraday and resonant density waves in ultracold dipolar Bose-Einstein condensates. It also studies the collective oscillation modes of dipolar condensates and their ground-state properties for experimentally relevant atomic species with the permanent magnetic dipole moment: chromium ^{52}Cr, erbium ^{168}Er, and dysprosium ^{164}Dy. The interplay of the contact and the dipole-dipole interaction in such systems is a hot research topic today, but a detailed understanding of their dynamics and even the stability is still lacking. This thesis contributes to variational and numerical description of driven dipolar systems and their properties, which are important for ongoing experiments, and will be of particular interest as the strongly dipolar regime becomes experimentally available.

We have introduced here a variational approach and used it to describe the ground state, the collective oscillation modes, and the Faraday and resonant waves in dipolar BECs. This approach is based on the Gaussian variational ansatz, which includes the condensate widths and the conjugated dynamical phases as parameters. The ansatz is extended to include density modulations in order to capture the dynamics of density waves. Using our approach, we have derived analytical expressions for the ground-state widths of the condensate, and the frequencies of the collective oscillation modes: the breathing, the quadrupole, and the radial-quadrupole mode. These results are verified by comparison with the numerical results obtained by solving the dipolar GPE for each of the three atomic species. We have found very good agreement between the analytical and numerical results, and confirmed that the derived expressions for the ground-state widths and collective oscillation frequencies

can be reliably used in the relevant parameter ranges.

We have studied the effects of the contact and the dipole-dipole interaction on the properties of the ground state and of the collective oscillation modes. While the increase of the contact interaction strength always leads to an increase of condensate widths, the situation is more complex when the dipole-dipole interaction is varied. In a cigar-shaped geometry when the dipoles are oriented in the radial direction, the increase of the DDI strength leads to the increase of condensate widths in the weak-confinement direction and in the direction of the dipoles, while the width in the third direction decreases. We have also studied the frequencies of the collective modes, where the interaction effects turn out to be less pronounced, in particular for the breathing and the quadrupole mode, whose values practically remain constant over the whole range of experimentally relevant values of a_s and a_{dd}. The frequency of the radial-quadrupole mode is more sensitive to changes of interaction strengths, especially the contact interaction strength a_s, and shows a nonmonotonous behavior as a function of the dipole-dipole interaction strength a_{dd}.

The main contribution of the thesis is the study of driven dipolar BECs, where the emergence of density waves is expected. This phenomenon is investigated in an experimentally-inspired setup, where the dipolar condensate is confined into a cigar-shaped harmonic trap. The dipole moments of the atoms are assumed to be orthogonal to the weak confinement axis, since this maximizes the stability of the system. The driving of the system is achieved by harmonic modulation of the radial part of the trap, and the density waves were observed in the longitudinal, weak-confinement direction.

Using our variational approach, the obtained equations for the dynamical evolution of the system are cast into the form of the Mathieu-like differential equation. This allowed us to identify the most unstable solutions of the Mathieu's equation with the Faraday and the resonant waves, which we have observed numerically. Based on this idea, we have derived analytical expressions for the periods of these two types of density waves. Performing the FFT analysis of the results of extensive numerical simulations, we were able to calculate the corresponding periods numer-

ically, as functions of the contact and the dipole-dipole interaction strength. The comparison of variational and numerical results shows very good agreement and demonstrates that the derived analytical expressions provide a full understanding of the properties of density waves in dipolar condensates.

The thesis presents the split-step semi-implicit Crank-Nicolson method used to solve the dipolar GPE, as well as the details about the corresponding programs, including the calculation of the dipole-dipole interaction term and relevant physical quantities. We have also presented the scalability testing results of our parallel programs, which demonstrate their efficiency on parallel computer clusters.

A Fourier transform of the DDI potential

In contrast to the contact interaction, which is symmetric and has a short range, the dipolar interaction between atoms or molecules is anisotropic and has a long range. The dipolar effects are brought in into the GPE through an additional nonlinear interaction term that reads in the dimensionless form

$$3Na_{\mathrm{dd}} \int d\mathbf{r}'\, U_{\mathrm{dd}}(\mathbf{r}-\mathbf{r}')\, |\psi(\mathbf{r}')|^2 \,, \tag{A.1}$$

where N is the number of atoms in the condensate, a_{dd} the length that quantifies the strength of the DDI, $|\psi(\mathbf{r}')|^2$ the density of the condensate, and $U_{\mathrm{dd}}(\mathbf{r}-\mathbf{r}')$ the DDI potential. For an arbitrary orientation of the dipoles defined by a unit vector $\mathbf{m}$, the dipolar potential is given by

$$U_{\mathrm{dd}}(\mathbf{r}) = \frac{\mathbf{r}^2 - 3\,(\mathbf{r}\cdot\mathbf{m})^2}{r^5} \,. \tag{A.2}$$

If the dipoles are oriented in z direction, the above expression transforms into

$$U_{\mathrm{dd}}(\mathbf{r}) = \frac{1-3\cos^2\theta}{r^3} \,. \tag{A.3}$$

where θ is the angle between the vector $\mathbf{r}$ and the polarization axis (z direction).

In coordinate space, due to issues with the numerical divergence at short distances, calculation of the dipolar term in the GPE is not straightforward. This is usually resolved by switching to the $\mathbf{k}$-space, where the calculation does not suffer from a singular behavior. Additionally, this allows the use of the FFT, which speeds up numerical calculations. By means of the convolution theorem, the integral (A.1) transforms into

$$\int d\mathbf{r}'\, U_{\mathrm{dd}}(\mathbf{r}-\mathbf{r}')\, |\psi(\mathbf{r}')|^2 = \mathcal{F}^{-1}\left\{\mathcal{F}\left[U_{\mathrm{dd}}\right](\mathbf{k})\, \mathcal{F}\left[|\psi|^2\right](\mathbf{k})\right\}(\mathbf{r}) \,, \tag{A.4}$$

where $\mathcal{F}$ represents the Fourier transform and $\mathcal{F}^{-1}$ the inverse Fourier transform, defined respectively by

$$\mathcal{F}[f](\mathbf{k}) = \tilde{f}(\mathbf{k}) = \int d\mathbf{r}\, f(\mathbf{r})\, e^{-i\,\mathbf{k}\cdot\mathbf{r}} \,, \tag{A.5}$$

$$\mathcal{F}^{-1}[\tilde{f}](\mathbf{r}) = f(\mathbf{r}) = \frac{1}{(2\pi)^3} \int d\mathbf{k}\, \tilde{f}(\mathbf{k})\, e^{i\,\mathbf{k}\cdot\mathbf{r}} \,. \tag{A.6}$$

The Fourier transform of the dipolar potential $\tilde{U}_{\rm dd}(\mathbf{k})$ can be calculated analytically using the spherical coordinates,

$$\tilde{U}_{\rm dd}(\mathbf{k}) = \int d\mathbf{r}\, U_{\rm dd}(\mathbf{r})\, e^{-i\,\mathbf{k}\cdot\mathbf{r}} = \int_0^\infty dr \int_0^{2\pi} d\varphi \int_0^\pi \sin\theta\, d\theta \times \frac{1-3\cos^2\theta}{r}\, e^{-ikr(\sin\theta\sin\theta_k\cos(\varphi-\varphi_k)+\cos\theta\cos\theta_k)}\,, \tag{A.7}$$

where, in spherical coordinates, $\mathbf{k} = (k, \theta_k, \varphi_k)$. Although the coordinate system is chosen such that the vector $\mathbf{m}$ is oriented along z axis, we still have the freedom to rotate it around this axis, which makes it possible to eliminate the angle φ_k. If we denote the θ_k in the selected coordinate system by α, the integral (A.7) becomes

$$\tilde{U}_{\rm dd}(\mathbf{k}) = \int_0^\infty dr \int_0^{2\pi} d\varphi \int_0^\pi d\theta \sin\theta\, \frac{1-3\left(\sin\alpha\sin\theta\sin\varphi+\cos\alpha\cos\theta\right)^2}{r}\, e^{-ikr\cos\theta}\,. \tag{A.8}$$

After integration over the variable φ, we obtain

$$\tilde{U}_{\rm dd}(\mathbf{k}) = \pi\left(3\cos^2\alpha-1\right)\int_0^\infty dr \int_0^\pi d\theta \sin\theta\, \frac{1-3\cos^2\theta}{r}\, e^{-ikr\cos\theta}\,. \tag{A.9}$$

The θ-integral above is solved by a variable change $u = \cos\theta$, yielding

$$\tilde{U}_{\rm dd}(\mathbf{k}) = 4\pi\left(1-3\cos^2\alpha\right)\int_0^\infty dr\, \left[\frac{\sin(kr)}{kr^2}+\frac{3\cos(kr)}{k^2r^3}-\frac{3\sin(kr)}{k^3r^4}\right]. \tag{A.10}$$

This integral is calculated using another variable change $v = kr$,

$$\begin{aligned}\tilde{U}_{\rm dd}(\mathbf{k}) &= 4\pi\left(1-3\cos^2\alpha\right)\lim_{b\to0}\int_{kb}^\infty dv\, \left[\frac{\sin v}{v^2}+\frac{3\cos v}{v^3}-\frac{3\sin v}{v^4}\right] \\ &= 4\pi\left(1-3\cos^2\alpha\right)\lim_{b\to0}\frac{kb\cos(kb)-\sin(kb)}{(kb)^3} \\ &= \frac{4\pi}{3}\left(3\cos^2\alpha-1\right) = \frac{4\pi}{3}\left(\frac{3\,k_z^2}{k^2}-1\right).\end{aligned} \tag{A.11}$$

According to this, we can immediately write the general expression for an arbitrary orientation of the dipoles $\mathbf{m}$ in the form

$$\tilde{U}_{\rm dd}(\mathbf{k}) = \frac{4\pi}{3}\left[\frac{3\,(\mathbf{m}\cdot\mathbf{k})^2}{k^2}-1\right]. \tag{A.12}$$

B Lagrangian of the DDI term

Using the Lagrangian density (2.51), we calculate the Lagrangian term (2.64) that corresponds to the DDI energy for the Gaussian ansatz (2.52), used in the variational study of the collective oscillation modes, as well as the term (5.11) for the modified ansatz (5.2), used to describe the Faraday and resonant waves. Note that both expressions can be written in the form

$$L_5(t) = -\frac{3Na_{\rm dd}}{(2\pi)^2}\, B^2 \int d\mathbf{k} \left(3\,\frac{k_z^2}{k_x^2+k_y^2+k_z^2} - 1 \right) e^{-\frac{1}{2}(k_x^2u_x^2+k_y^2u_y^2+k_z^2u_z^2)}\,, \tag{B.1}$$

where expression (2.64) is obtained for $B = 1$, while we get expression (5.11) for

$$B^2 = 1 - \frac{8\,\alpha^2}{(2+\alpha^2+\beta^2)^2}\,. \tag{B.2}$$

The above integral describes the anisotropic character of the dipole-dipole interaction in ultracold quantum gases. After switching to the spherical coordinate system via the following change of variables

$$k_xu_x = k\sin\theta\cos\varphi\,, \quad k_yu_y = k\sin\theta\sin\varphi\,, \quad k_zu_z = k\cos\theta\,, \tag{B.3}$$

the above integral transforms into

$$\begin{aligned} L_5(t) = -\frac{Na_{\rm dd}}{(2\pi)^2\,u_xu_yu_z}\, B^2 \int_0^\infty dk\, k^2 e^{-k^2/2} \int_0^{2\pi} d\varphi \int_0^\pi d\theta \sin\theta \\ \times \left(\frac{3\,\frac{1}{u_z^2}\cos^2\theta}{\frac{1}{u_x^2}\sin^2\theta\cos^2\varphi + \frac{1}{u_y^2}\sin^2\theta\sin^2\varphi + \frac{1}{u_z^2}\cos^2\theta} - 1 \right)\,. \end{aligned} \tag{B.4}$$

The integral over k is of the Gaussian type that can be solved analytically, leading to

$$\begin{aligned} L_5(t) = -\frac{Na_{\rm dd}}{(2\pi)^2 u_xu_yu_z}\, B^2 \sqrt{\frac{\pi}{2}} \int_0^{2\pi} d\varphi \int_0^\pi d\theta \sin\theta \\ \times \left(\frac{3\,\frac{u_x^2u_y^2}{u_z^4}\cos^2\theta}{\frac{u_y^2}{u_z^2}\sin^2\theta\cos^2\varphi + \frac{u_x^2}{u_z^2}\sin^2\theta\sin^2\varphi + \frac{u_x^2u_y^2}{u_z^4}\cos^2\theta} - 1 \right)\,. \end{aligned} \tag{B.5}$$

If we introduce the dipolar anisotropy function [42], see Appendix C for details,

$$f(x,y) = -\frac{1}{4\pi} \int_0^{2\pi} d\varphi \int_0^\pi d\theta \sin\theta \left(\frac{3\,x^2y^2\cos^2\theta}{x^2\sin^2\varphi\sin^2\theta + y^2\cos^2\varphi\sin^2\theta x^2y^2\cos^2\theta} - 1 \right)\,, \tag{B.6}$$

we can write $L_5(t)$ as

$$L_5(t) = \frac{N a_{\rm dd}}{\sqrt{2\pi}\, u_x u_y u_z} B^2 f\left(\frac{u_x}{u_z}, \frac{u_y}{u_z}\right), \tag{B.7}$$

where exact expressions for the anisotropy function in terms of the elliptic integrals of the first (F) and the second (E) kind for different values of its arguments are listed in Appendix C. For our analysis, due to geometry of the system described in Appendix D, the most relevant region of parameters is $0 < u_y/u_z < 1 < u_x/u_z$, in which the anisotropy function can be written as

$$f(x,y) = \frac{1+2y^2}{1-y^2} - \frac{3xy\sqrt{x^2-y^2}\, E(\theta,k)}{(x^2-1)(1-y^2)} + \frac{3xy\, F(\theta,k)}{(x^2-1)\sqrt{x^2-y^2}}, \tag{B.8}$$

where $k = \sqrt{(x^2-1)/(x^2-y^2)}$, and $\sin\theta = \sqrt{x^2-y^2}/x$.

C Anisotropy function

In theoretical studies of dipolar ultracold atomic or molecular systems, the anisotropy function emerges as a consequence of the anisotropic character of the dipole-dipole interaction [42]. It is defined as

$$\begin{aligned} f(x,y) &= -\frac{1}{4\pi}\int_0^{2\pi} d\varphi \int_0^{\pi} d\theta \sin\theta \left(\frac{3\,x^2y^2\cos^2\theta}{x^2\sin^2\varphi\sin^2\theta + y^2\cos^2\varphi\sin^2\theta + x^2y^2\cos^2\theta} - 1 \right) \\ &= 1 - \frac{3\,x^2y^2}{4\pi}\int_0^{\pi} d\theta \sin\theta\cos^2\theta \int_0^{\pi} d\varphi \frac{1}{(x^2\sin^2\varphi + y^2\cos^2\varphi)\sin^2\theta + x^2y^2\cos^2\theta}. \end{aligned} \tag{C.1}$$

According to the above definition, we can assume $x, y \geq 0$ without loss of generality. The φ integral can be solved using relation (3.642.1) from Reference [43], yielding

$$f(x,y) = 1 - \frac{3\,xy}{2}\int_0^{\pi} d\theta \sin\theta \frac{\cos^2\theta}{\sqrt{1-(1-x^2)\cos^2\theta}\sqrt{1-(1-y^2)\cos^2\theta}}\,. \tag{C.2}$$

Note that function f is symmetric in its arguments $f(x,y) = f(y,x)$ [42]. Depending on the values of the arguments x and y, we can consider the following cases:

1. $x < y < 1$

   Using the substitution $u = \sqrt{1-x^2}\cos\theta$, the integral (C.2) becomes

   $$f(x,y) = 1 + \frac{3\,xy}{(1-x^2)^{3/2}}\int_0^{\sqrt{1-x^2}} du \frac{u^2}{\sqrt{1-k^2u^2}\sqrt{1-u^2}}\,, \tag{C.3}$$

   where $k^2 = (1-y^2)/(1-x^2) < 1$. The solution of the above u-integral can be expressed via elliptic integrals [43] of the first and the second kind, respectively,

   $$F(\theta,k) = \int_0^{\sin\theta} du \frac{1}{\sqrt{(1-u^2)(1-k^2u^2)}} = \int_0^{\theta} d\theta \frac{1}{\sqrt{1-k^2\sin^2\theta}}\,, \tag{C.4}$$

   $$E(\theta,k) = \int_0^{\sin\theta} du \frac{\sqrt{1-k^2u^2}}{\sqrt{1-u^2}} = \int_0^{\theta} d\theta \sqrt{1-k^2\sin^2\theta}\,, \tag{C.5}$$

yielding

$$f(x,y) = 1 + 3xy\frac{E(\theta,k) - F(\theta,k)}{(1-y^2)\sqrt{1-x^2}}\,, \tag{C.6}$$

where $\sin\theta = \sqrt{1-x^2}$.

2. $y < x < 1$

   Due to the symmetry of the anisotropy function, its value $f(x,y)$ can be calculated as $f(y,x)$ according to case 1.

3. $x < 1 < y$

   In this region it is necessary to analytically continue the function (C.6) using the table (8.127) from Reference [43]. With the transformations

$$k_1 = \frac{i\,k}{k'}\,, \qquad \sin\theta_1 = \frac{k'\,\sin\theta}{\Delta\theta}, \qquad \cos\theta_1 = \frac{\cos\theta}{\Delta\theta}\,, \tag{C.7}$$

   we obtain

$$f(x,y) = \frac{1+2x^2}{1-x^2} + \frac{3xy\sqrt{y^2-x^2}\,E(\theta_1,k_1)}{(y^2-1)(x^2-1)} + \frac{3xy\,F(\theta_1,k_1)}{(y^2-1)\sqrt{y^2-x^2}}\,, \tag{C.8}$$

   where $k_1 = \sqrt{\frac{y^2-1}{y^2-x^2}}$ and $\sin\theta_1 = \sqrt{y^2-x^2}/y$.

4. $y < 1 < x$

   Due to the symmetry of the anisotropy function, its value $f(x,y)$ can be calculated as $f(y,x)$ according to case 3.

5. $1 < x < y$

   In this region we proceed similarly as in the case 3, using the transformations

$$k_1 = \frac{k'}{i\,k}\,, \qquad \sin\theta_1 = -\frac{i\,k\,\sin\theta}{\Delta\theta}, \qquad \cos\theta_1 = \frac{1}{\Delta\theta}\,, \tag{C.9}$$

   where $k' = \sqrt{1-k^2}$ and $\Delta\theta = \sqrt{1-k^2\sin^2\theta}$, and obtain

$$f(x,y) = \frac{1+2x^2}{1-x^2} + \frac{3xy\,E(\theta_1,k_1)}{(x^2-1)\sqrt{y^2-1}}\,, \tag{C.10}$$

   where $k_1 = \sqrt{\frac{y^2-x^2}{y^2-1}}$ and $\sin\theta_1 = \sqrt{y^2-1}/y$.

6. $1 < y < x$

   Due to the symmetry of the anisotropy function, its value $f(x,y)$ can be calculated as $f(y,x)$ according to case 5.

7. $x = y$

   In the special case of equal arguments, $x \to y$, which corresponds to cylindrical symmetry of the system, the anisotropy function depends only on a single argument, and is given as

$$f_s(x) = \lim_{x \to y} f(x, y) = \frac{1 + 2x^2 - 3x^2\, d(x)}{1 - x^2}\,, \tag{C.11}$$

   where $d(x)$ is given by

$$d(x) = \begin{cases} \frac{1}{\sqrt{1-x^2}} \tanh^{-1} \sqrt{1 - x^2}\,, & x < 1\,, \\ 0\,, & x = 1\,, \\ \frac{1}{\sqrt{x^2-1}} \tan^{-1} \sqrt{x^2 - 1}\,, & 1 < x\,. \end{cases} \tag{C.12}$$

8. $x \neq y = 1$

$$f(x, 1) = \lim_{y \to 1} f(x, y) = -\frac{1}{2}\, f_s(1/x) \tag{C.13}$$

9. $x = 1 \neq y$

$$f(1, y) = f(y, 1) = -\frac{1}{2}\, f_s(1/y) \tag{C.14}$$

In this thesis, the parameters of the anisotropy function are ratios of the condensate widths u_x/u_z and u_y/u_z. As we have seen in Chapter 3, due to geometry of the system, the condensate in the ground state is much more elongated in x direction than in the other two directions. Also, we have observed that the dipole-dipole interaction increases the condensate width in z direction, and decreases it in y direction. The same relationships between the condensate widths are valid during the non-stationary dynamics of the condensate, as we have seen in Chapters 4 and 5. Therefore, in our analysis $0 < u_y < u_z < u_x$, i.e., $0 < u_y/u_z < 1 < u_x/u_z$, which corresponds to the case 4 above.

In the thesis we use $f_i(x, y)$ to denote the first partial derivative of the anisotropy function with respect to its argument $i = 1, 2$, and f_{ij} to denote the second partial derivative

$$f_{ij}(x_1, x_2) = \frac{\partial^2}{\partial x_i\, \partial x_j} f(x_1, x_2)\,. \tag{C.15}$$

In our analysis of the cylindrically symmetric ultracold quantum gases, which exists if the polarization direction matches the weak confinement direction of the trap, we have used the following useful limits:

$$\lim_{y\to x} x\, f_1(x,y) = \lim_{y\to x} y\, f_2(x,y) = f_s'(x) = \frac{(2+x^2)f_s(x)}{2(1-x^2)} - 1\,, \tag{C.16}$$

$$\lim_{y\to x} f_{11}(x,y) = \lim_{y\to x} f_{22}(x,y) = \frac{9\left[(4+x^2)\, f_s(x) - 2\,(1-x^2)\right]}{8\,(1-x^2)^2}\,, \tag{C.17}$$

$$\lim_{y\to x} f_{12}(x,y) = \lim_{y\to x} f_{21}(x,y) = \frac{(8+8x^2-x^4)\, f_s(x) - 2\,(4-5x^2+x^4)}{8x^2\,(1-x^2)^2}\,, \tag{C.18}$$

$$\lim_{y\to 1} x f_1(x,y) = f_s'(1/x)\,. \tag{C.19}$$

D Parameters of the system

In all numerical simulations and variational calculations we have used the system and discretization parameters specified here, unless otherwise stated. We have considered three atomic species and Table 4 lists the corresponding values of the mass m in atomic mass units u, the s-wave scattering length a_s in units of Bohr radius a_0, the dipole moment μ_{d} in units of Bohr magneton μ_{B}, the dipole-dipole interaction strength a_{dd} in units of Bohr radius (a_0), and the harmonic oscillator length l with respect to the chosen referent frequency $\omega_r = 160.5 \times 2\pi$ Hz.

Table 4: Summary of atomic species parameters used in numerical simulations and variational calculations.

Species	m (u)	a_s (a_0)	μ_{d} (μ_{B})	a_{dd} (a_0)	l (μm)
^{52}Cr	51.94050	105	6	15.126	1.10112
^{168}Er	167.93237	100	7	66.564	0.61238
^{164}Dy	163.92918	100	10	132.607	0.61981

All simulations and calculations are performed with the same number of atoms, $N = 10^4$.

We have considered the harmonically trapped system, with the frequencies taken from Reference [30], i.e., $\omega_x = 7 \times 2\pi$ Hz, $\omega_y = 160.5 \times 2\pi$ Hz, and $\omega_z = 160.5 \times 2\pi$ Hz. The trapping potential is defined by Equation (2.22), and for the chosen frequencies the atoms are weakly confined in x direction, i.e., we have used a cigar-shaped trap. Therefore, we refer to x direction as the longitudinal one, while y and z direction represent the radial ones. In order to cast the underlying equations into a dimensionless form, we have chosen the referent frequency $\omega_r = \omega_y = \omega_z = 160.5 \times 2\pi$ Hz, which defines the length scale through the harmonic oscillator length $l = \sqrt{\hbar/(m\omega_r)}$, the time scale as $1/\omega_r$, the energy scale as $\hbar\omega_r$. The trapping frequencies are also expressed in units of ω_r through the trap aspect ratios $\gamma = \omega_x/\omega_r = 0.04361$, $\nu = \omega_y/\omega_r = 1$, and $\lambda = \omega_z/\omega_r = 1$.

We assume that the dipoles are oriented along z direction, i.e., orthogonal to the weakly confined x direction. The Fourier transform of the dipolar interaction potential is thus

$$\mathcal{F}[U_{\rm dd}(\mathbf{r})](\mathbf{k}) = \frac{4\pi}{3}\left(\frac{3\,k_z^2}{\mathbf{k}^2} - 1\right). \tag{D.1}$$

The system is driven by a harmonic modulation of the frequencies in the tightly confined y and z direction,

$$\omega_y(t) = \omega_z(t) = \Omega_0(1 + \epsilon \sin \omega_m t)\,, \tag{D.2}$$

where $\Omega_0 = \omega_y = \omega_z$ has a value given above, $\epsilon = 0.1 - 0.2$ is the modulation amplitude, and ω_m is the modulation frequency. The modulation frequency is expressed in units of ω_r through the aspect ratio $\eta_m = \omega_m/\omega_r$.

We have studied the properties of the ground state, collective oscillation modes, Faraday and resonant waves as functions of the contact and the dipole-dipole interaction strength. This models BEC experiments, where the strength of the contact interaction can be varied over a broad range of values using the Feshbach resonance technique [9]. This is also possible for the strength of the DDI, which can be tuned using a fast rotating magnetic field [24, 25]. Therefore, the values of a_s and $a_{\rm dd}$ listed in Table 4 are used whenever we refer to their fixed values, while in some calculations we have considered experimentally relevant ranges of these interaction strengths.

In numerical simulations, we have discretized space and time by defining the corresponding spacings and the time step, as well as the size of the space mesh and the number of the time steps. In our simulations we have used equal numbers of mesh points in all directions, $N_x = N_y = N_z = 500$, with different spacings, $\Delta x = 0.5$ and $\Delta y = \Delta z = 0.1$. This choice was made due to the cigar shape of the condensate. Such a mesh corresponds to the simulation box of the volume of approximately $250 \times 50 \times 50$ μm^3, which is appropriate for the above trapping potential and the considered atomic species.

Time was discretized using the time step Δt with the typical values between

10^{-2} and 10^{-3} in units of $1/\omega_r$. For the Faraday and resonant waves, the number of time steps (iterations) N was in the range $1 - 2 \times 10^5$, which corresponds to the simulation of the evolution in the range 250-500 ms. For the calculation of the collective oscillation modes, we had to use much larger iteration numbers, for at least one order of magnitude, in order to achieve the accuracy of 0.1 Hz.

The value of the cutoff parameter R from Equation (6.25) in all simulations was $R = 10$.

The ground state of the condensate was calculated using the imaginary-time propagation starting from the Gaussian initial wave function, defined by

$$\psi(x, y, z) = \frac{(\gamma\,\nu\,\lambda)^{1/4}}{\pi^{3/4}}\, e^{-\frac{1}{2}(\gamma x^2+\nu y^2+\lambda z^2)}\,. \tag{D.3}$$

It corresponds to the solution of the Schrödinger equation, i.e., the GPE for $a_s = a_{\mathrm{dd}} = 0$, and represents the dimensionless form of Equation (3.1).

The values of the physical constants used are as follows:

u $= 1.6605390 \times 10^{-27}$ kg (atomic mass unit),

$a_0 = 5.29177210 \times 10^{-11}$ m (Bohr radius),

$\mu_{\mathrm{B}} = 9.2740099 \times 10^{-24}\,\mathrm{JT}^{-1}$ (Bohr magneton).

E Semi-implicit Crank–Nicolson scheme

Here we describe the practical implementation of the semi-implicit Crank–Nicolson algorithm [35–37]. In Chapter 6 we have introduced the time and the spatial discretization used to solve the dipolar GPE. The total evolution time T that will be simulated is discretized by dividing it into N_t equal sub-steps of the duration $\Delta t = T/N_t$. The spatial coordinates are discretized by introducing a spatial mesh of N_x, N_y, and N_z equidistant points in x, y, and z direction, respectively. The spatial extents of the system considered are given by $L_x = N_x\,\Delta x$, $L_y = N_y\,\Delta y$, and $L_z = N_z\,\Delta z$, where Δx, Δy, and Δz are discretization steps in the corresponding directions. For practical reasons, the center of the coordinate system coincides with the simulation box center, such that the coordinates take the values $x \in [-L_x/2, L_x/2]$, $y \in [-L_y/2, L_y/2]$, and $z \in [-L_z/2, L_z/2]$.

In addition to this, within each time step Δt, the split-step nature of the algorithm divides our Hamiltonian into four parts: the non-derivative part $\hat{H}_0$, and the three parts that contain spatial derivatives, $\hat{H}_1$, $\hat{H}_2$, $\hat{H}_3$, which read

$$\hat{H}_0 = U(\mathbf{r},t) + 4\pi N a_s \left|\psi(\mathbf{r},t)\right|^2 + 3N a_{\mathrm{dd}} \int d\mathbf{r}'\, U_{\mathrm{dd}}(\mathbf{r}-\mathbf{r}') \left|\psi(\mathbf{r}',t)\right|^2 , \tag{E.1}$$

$$\hat{H}_1 = \frac{\partial^2}{\partial x^2} , \quad \hat{H}_2 = \frac{\partial^2}{\partial y^2} , \quad \hat{H}_3 = \frac{\partial^2}{\partial z^2} . \tag{E.2}$$

By doing this, we have approximated our single dipolar GPE with the four sequential partial differential equations,

$$i\,\frac{\partial\psi(\mathbf{r},t)}{\partial t} = \hat{H}_0\,\psi(\mathbf{r},t) , \tag{E.3}$$

$$i\,\frac{\partial\psi(\mathbf{r},t)}{\partial t} = \hat{H}_1\,\psi(\mathbf{r},t) , \quad i\,\frac{\partial\psi(\mathbf{r},t)}{\partial t} = \hat{H}_2\,\psi(\mathbf{r},t) , \quad i\,\frac{\partial\psi(\mathbf{r},t)}{\partial t} = \hat{H}_3\,\psi(\mathbf{r},t) , \tag{E.4}$$

which are solved one after the other in the algorithm.

In a given time step n, we start with the wave function $\psi^n(\mathbf{r})$, obtained in the previous time step. We point out that the time dependence of the wave function is now denoted by the superscript n, which corresponds to the time $t = n\,\Delta t$. The time propagation proceeds by solving Equation (E.3), which can be done explicitly

according to (6.9). This produces the intermediate solution $\psi^{n+1/4}(\mathbf{r})$, ready to be propagated in time by solving Equations (E.4). This is done by expressing the corresponding derivative operators in a semi-implicit form,

$$i\,\frac{\psi^{n+2/4}(\mathbf{r})-\psi^{n+1/4}(\mathbf{r})}{\Delta t}=\frac{1}{2}\,\hat{H}_1\left[\psi^{n+2/4}(\mathbf{r})+\psi^{n+1/4}(\mathbf{r})\right]\,, \tag{E.5}$$

$$i\,\frac{\psi^{n+3/4}(\mathbf{r})-\psi^{n+2/4}(\mathbf{r})}{\Delta t}=\frac{1}{2}\,\hat{H}_2\left[\psi^{n+3/4}(\mathbf{r})+\psi^{n+2/4}(\mathbf{r})\right]\,, \tag{E.6}$$

$$i\,\frac{\psi^{n+1}(\mathbf{r})-\psi^{n+3/4}(\mathbf{r})}{\Delta t}=\frac{1}{2}\,\hat{H}_3\left[\psi^{n+1}(\mathbf{r})+\psi^{n+3/4}(\mathbf{r})\right]\,. \tag{E.7}$$

The complete propagation procedure outlined above yields the wave function $\psi^{n+1}(\mathbf{r})$ at the moment $t=(n+1)\Delta t$. On the left-hand sides of Equations (E.5) - (E.7) the partial derivative with respect to time is expressed by a two-point formula, while on the right-hand sides instead of the wave function at the current time, we use a linear combination of the current and the future wave function values to improve the stability of the algorithm. This makes the algorithm semi-implicit.

For convenience, let us denote the spatial mesh step in the x, y, and z direction by Δh_i, respectively, and use the lower index of the wave function to define a position in the mesh in the given direction. For instance, when we are considering Equation (E.5) along x direction, $\psi_i^{n+j/4}$ denotes the wave function value at $x=-L_x/2+i\,\Delta h_1$, while the values of the other two coordinates are implicitly assumed. In this notation, with the three-point formula for the Laplacian on the right-hand side of Equations (E.5) - (E.7), the equation in the given direction j reads

$$\begin{aligned} i\,\frac{\psi_i^{n+(j+1)/4}-\psi_i^{n+j/4}}{\Delta t}=\frac{1}{4\,\Delta h_j^2}\Big(&\psi_{i+1}^{n+(j+1)/4}-2\,\psi_i^{n+(j+1)/4}+\psi_{i-1}^{n+(j+1)/4}\\ &+\psi_{i+1}^{n+j/4}-2\,\psi_i^{n+j/4}+\psi_{i-1}^{n+j/4}\Big)\,, \end{aligned} \tag{E.8}$$

where $j=1,2,3$ defines the spatial direction of propagation. In the above equation, the known quantities have the upper index $n+j/4$, while the unknown quantities have the superscript $n+(j+1)/4$. Taking this into account, Equation (E.8) can be written in the form of a series of tridiagonal equations,

$$A_j^-\,\psi_{i-1}^{n+(j+1)/4}+A_j^0\psi_i^{n+(j+1)/4}+A_j^+\,\psi_{i+1}^{n+(j+1)/4}=B_i^{n+j/4}\,, \tag{E.9}$$

where the following coefficients are defined by the known quantities,

$$A_j^- = A_j^+ = -\frac{\Delta t}{4\Delta h_j^2}\,, \quad A_j^0 = 1 + i\,\frac{\Delta t}{2\Delta h_j^2}\,, \tag{E.10}$$

$$B_i^{n+j/4} = i\,\frac{\Delta t}{4\Delta h_j^2}\left(\psi_{i+1}^{n+j/4} - 2\psi_i^{n+j/4} + \psi_{i-1}^{n+j/4}\right) + \psi_i^{n+j/4}\,. \tag{E.11}$$

Equation (E.9) is solved by using the forward recursion method, i.e., by expressing the mesh values of the propagated wave function in each spatial direction in the form

$$\psi_{i+1}^{n+(j+1)/4} = \alpha_i^j \psi_i^{n+(j+1)/4} + \beta_i^{n+j/4}\,. \tag{E.12}$$

Inserting the above rule into Equation (E.9), the propagated mesh values of the wave function are given by

$$\psi_i^{n+(j+1)/4} = \gamma_i^j \left(A_j^- \psi_{i-1}^{n+(j+1)/4} + A_j^+ \beta_i^{n+j/4} - B_i^{n+j/4}\right)\,, \tag{E.13}$$

with

$$\gamma_i^j = -\frac{1}{A_j^0 + A_j^+ \alpha_i^j}\,. \tag{E.14}$$

We now obtain the backward recursion relations for the coefficients α_i^j and $\beta_i^{n+j/4}$ from Equations (E.12) and (E.13),

$$\alpha_{i-1}^j = \gamma_i^j A_j^-\,, \tag{E.15}$$

$$\beta_{i-1}^{n+j/4} = \gamma_i^j \left(A_j^+ \beta_i^{n+j/4} - B_i^{n+j/4}\right)\,. \tag{E.16}$$

In the algorithm, the coefficients $\alpha_i^{j/4}$ and $\beta_i^{n+j/4}$ are calculated starting from $i = N_j - 2$ to $i = 0$. Since the value of the wave function must vanish at the mesh boundary, we chose the initial border values of $\alpha_{N_j-1}^{j/4}$ and $\beta_{N_j-1}^{n+j/4}$ to be equal to 0. The coefficients A_j^-, A_j^+, A_j^0, α_i^j, and γ_i^j do not depend on the time step n, and are therefore constant for a particular mesh setup. Only the coefficients $\beta_i^{n+j/4}$, and consequentially $B_i^{n+j/4}$, have to be recalculated after each time step, for each spatial direction $j = 1, 2, 3$.

F Details on testing of the scaling of programs

Here we give the details related to the testing setup used in Chapter 6. The code that implements the algorithm for solving the dipolar GPE is optimized for use with the commercially-licensed Intel and the free, open-source GNU compiler suite. We have also tested and verified the compilation with IBM's xlc compiler, PGI's pgcc compiler, and Oracle's suncc (former Sun's) compiler. Beside of the most generic, fully-anisotropic three-dimensional trap, we have written additional independent codes for 1D and 2D systems, for 3D system with cylindrical (effectively 2D) and spherical (effectively 1D) symmetry, and 2D systems with cylindrical symmetry (effectively 1D). All outputs from the simulations are stored using the Hierarchical Data Format (HDF) library [101], which is designed to store and organize large amounts of data. Using HDF, the average size of the results of a typical simulation is around 2 GB of storage space. This includes the wave function calculated in the imaginary-time simulation and all results of the real-time propagation. Compared to the same amount of information stored in a plain text format, HDF provides compression by an average factor of ten. Also, since HDF is a widely used format, various externally developed visualization tools can be used for the analysis of the obtained results.

In addition to the OpenMP-parallelized version of the code [90–92], our group has parallelized the algorithm using the Message Passing Interface (MPI) library [92] that enables utilization of distributed memory computing systems (computer clusters). Furthermore, using the CUDA toolkit, the group has developed algorithms optimized for the graphics processing units (GPU) able to utilize hardware accelerators [93]. Finally, combining all parallelization techniques (OpenMP, MPI, and CUDA), hybrid programs for solving the dipolar GPE were also developed and made publicly available [94]. These programs are able to utilize state-of-the-art computing clusters available today.

The PARADOX computing cluster at the Scientific Computing Laboratory, Cen-

ter for the Study of Complex Systems of the Institute of Physics Belgrade has been used for development and testing of the programs. This resource has more than 2,500 Intel Xeon E5-2670 Sandy Bridge processing cores at a frequency of 2.6 GHz and 32 GB of RAM (2 GB per CPU core). Additional 106 NVIDIA Tesla M2090 graphic cards with 6 GB of RAM are distributed over available computing nodes. The cluster nodes are interconnected via a QDR Infiniband technology, through a non-blocking 144-port Mellanox QDR Infiniband switch. The communication speed of all nodes is 40 Gbps in both directions, while the peak computing power of PARADOX is 105 TFlops. The cluster provides around 100 TB of storage space, which is distributed via a Lustre high-performance parallel file system that uses Infiniband technology.

References

[1] C. C. Bradley, C. A. Sackett, J. J. Tollett, and R. G. Hulet, *Evidence of Bose-Einstein Condensation in an Atomic Gas with Attractive Interactions*, Phys. Rev. Lett. **75**, 1687 (1995).

[2] M. H. Anderson, J. R. Ensher, M. R. Matthews, C. E. Wieman, and E. A. Cornell, *Observation of Bose-Einstein condensation in a dilute atomic vapor*, Science **269**, 198 (1995).

[3] K. B. Davis, M. O. Mewes, M. R. Andrews, N. J. van Druten, D. S. Durfee, D. M. Kurn, and W. Ketterle, *Bose-Einstein condensation in a gas of sodium atoms*, Phys. Rev. Lett. **75**, 3969 (1995).

[4] S. N. Bose, *Plancks gesetz und lichtquantenhypothese*, Z. Phys. **26**, 178 (1924).

[5] A. Einstein, *Quantentheorie des einatomigen idealen Gases*, Sitzungsber. Preuss. Akad. Wiss., Phys. Math. Kl. **22**, 261 (1924).

[6] R. P. Feynman, *Simulating physics with computers*, Int. J. Theor. Phys. **21**, 467 (1982).

[7] C. J. Pethick and H. Smith, *Bose–Einstein condensation in dilute gases*, Cambridge University Press (2008).

[8] L. P. Pitaevskii and S. Stringari, *Bose-Einstein condensation*, Oxford University Press (2003).

[9] S. Inouye, M. R. Andrews, J. Stenger, H. J. Miesner, D. M. Stamper-Kurn, and W. Ketterle, *Observation of Feshbach resonances in a Bose–Einstein condensate*, Nature **392**, 32354 (1998).

[10] T. Lahaye, T. Koch, B. Fröhlich, M. Fattori, J. Metz, A. Griesmaier, S. Giovanazzi, and T. Pfau, *Strong dipolar effects in a quantum ferrofluid*, Nature **448**, 672 (2007).

[11] M. Lu, N. Q. Burdick, S. H. Youn, and B. L. Lev, *Strongly dipolar Bose-Einstein condensate of dysprosium*, Phys. Rev. Lett. **107**, 190401 (2011).

[12] K. Aikawa, A. Frisch, M. Mark, S. Baier, A. Rietzler, R. Grimm, and F. Ferlaino, *Bose-Einstein condensation of erbium*, Phys. Rev. Lett. **108**, 210401 (2012).

[13] M. H. G. de Miranda, A. Chotia, B. Neyenhuis, D. Wang, G. Quemener, S. Ospelkaus, J. L. Bohn, J. Ye, and D. S. Jin, *Controlling the quantum stereodynamics of ultracold bimolecular reactions*, Nat. Phys. **7**, 502 (2011).

[14] A. Frisch, M. Mark, K. Aikawa, S. Baier, R. Grimm, A. Petrov, S. Kotochigova, G. Quemener, M. Lepers, O. Dulieu, and F. Ferlaino, *Ultracold dipolar molecules composed of strongly magnetic atoms*, Phys. Rev. Lett. **115**, 203201 (2015).

[15] M. A. Baranov, *Theoretical progress in many-body physics with ultracold dipolar gases*, Phys. Rep. **464**, 71 (2008).

[16] N. G. Parker, C. Ticknor, A. M. Martin, and D. H. J. O'Dell, *Structure formation during the collapse of a dipolar atomic Bose-Einstein condensate*, Phys. Rev. A **79**, 013617 (2009).

[17] R. M. Wilson, S. Ronen, and J. L. Bohn, *Angular collapse of dipolar Bose-Einstein condensates*, Phys. Rev. A **80**, 023614 (2009).

[18] A. Junginger, J. Main, G. Wunner, and T. Bartsch, *Symmetry-breaking thermally induced collapse of dipolar Bose-Einstein condensates*, Phys. Rev. A **86**, 023632 (2012).

[19] H. Kadau, M. Schmitt, M. Wenzel, C. Wink, T. Maier, I. Ferrier-Barbut, and T. Pfau, *Observing the Rosensweig instability of a quantum ferrofluid*, Nature **530**, 194 (2016).

[20] I. Ferrier-Barbut, H. Kadau, M. Schmitt, M. Wenzel, and T. Pfau, *Observation of quantum droplets in a strongly dipolar Bose gas*, Phys. Rev. Lett. **116**, 215301 (2016).

[21] L. Chomaz, S. Baier, D. Petter, M. J. Mark, F. Wachtler, L. Santos, and F. Ferlaino, *Quantum-fluctuation-driven crossover from a dilute Bose-Einstein condensate to a macrodroplet in a dipolar quantum fluid*, Phys. Rev. X **6**, 041039 (2016).

[22] R. E. Rosensweig, *Ferrohydrodynamics*, Cambridge University Press (1985).

[23] F. Böttcher, J-N. Schmidt, M. Wenzel, J. Hertkorn, M. Guo, T. Langen, and T. Pfau, *Transient Supersolid Properties in an Array of Dipolar Quantum Droplets*, Phys. Rev. X **9**, 011051 (2019).

[24] S. Giovanazzi, A. Görlitz, and T. Pfau, *Tuning the Dipolar Interaction in Quantum Gases*, Phys. Rev. Lett. **89**, 130401 (2002).

[25] Y. Tang, W. Kao, K-Y. Li, and B. L. Lev, *Tuning the Dipole-Dipole Interaction in a Quantum Gas with a Rotating Magnetic Field*, Phys. Rev. Lett. **120**, 230401 (2018).

[26] D. S. Jin, J. R. Ensher, M. R. Matthews, C. E. Wieman, and E. A. Cornell, *Collective excitations of a Bose-Einstein condensate in a dilute gas*, Phys. Rev. Lett. **77**, 420 (1996).

[27] M. O. Mewes, M. R. Andrews, N. J. van Druten, D. M. Kurn, D. S. Durfee, C. G. Townsend, and W. Ketterle, *Collective excitations of a Bose-Einstein condensate in a magnetic trap*, Phys. Rev. Lett. **77**, 988 (1996).

[28] M. Faraday, *On a peculiar class of acoustical figures; and on certain forms assumed by groups of particles upon vibrating elastic surfaces*, Phil. Trans. R. Soc. Lond. **121**, 299 (1831).

[29] K. Staliunas, S. Longhi, and G. J. de Valcárcel, *Faraday patterns in Bose-Einstein condensates*, Phys. Rev. Lett. **89**, 210406 (2002).

[30] P. Engels, C. Atherton, and M. A. Hoefer, *Observation of Faraday waves in a Bose-Einstein condensate*, Phys. Rev. Lett. **98**, 095301 (2007).

[31] A. Balaž and I. Nicolin, *Faraday waves in binary nonmiscible Bose-Einstein condensates*, Phys. Rev. A **85**, 023613 (2012).

[32] A. Balaž, R. Paun, A. I. Nicolin, S. Balasubramanian, and R. Ramaswamy, *Faraday waves in collisionally inhomogeneous Bose-Einstein condensates*, Phys. Rev. A **89**, 023609 (2014).

[33] D. Vudragović and A. Balaž, *Faraday and Resonant Waves in Dipolar Cigar-Shaped Bose-Einstein Condensates*, Symmetry **11**, 1090 (2019).

[34] L. D. Landau and E. M. Lifshitz, *Quantum Mechanics 3rd Edition*, Pergamon (1977).

[35] J. Crank and P. Nicolson, *A practical method for numerical evaluation of solutions of partial differential equations of the heat-conduction type*, P. Adv Comput Math **6**, 207 (1996).

[36] W. Ames, *Numerical Methods for Partial Differential Equations 3rd Edition*, Academic Press (1992).

[37] R. Dautray and J.-L. Lions, *Mathematical Analysis and Numerical Methods for Science and Technology*, Springer-Verlag Berlin Heidelberg (2000).

[38] S. Yi and L. You, *Trapped atomic condensates with anisotropic interactions*, Phys. Rev. A **61**, 041604 (2000).

[39] L. Santos, G. V. Shlyapnikov, P. Zoller, and M. Lewenstein, *Bose-Einstein Condensation in Trapped Dipolar Gases*, Phys. Rev. Lett. **85**, 1791 (2000).

[40] S. Yi and L. You, *Probing dipolar effects with condensate shape oscillation*, Phys. Rev. A **66**, 013607 (2002).

[41] S. Yi and L. You, *Calibrating Dipolar Interaction in an Atomic Condensate*, Phys. Rev. Lett. **92**, 193201 (2004).

[42] S. Giovanazzi, P. Pedri, L. Santos, A. Griesmaier, M. Fattori, T. Koch, J. Stuhler, and T. Pfau, *Expansion dynamics of a dipolar Bose-Einstein condensate*, Phys. Rev. A **74**, 013621 (2006).

[43] I. S. Gradshteyn and I. M. Ryzhik, *Table of Integrals, Series, and Products 7th Edition*, Academic Press is an imprint of Elsevier (1985).

[44] D. M. Stamper-Kurn, H.-J. Miesner, S. Inouye, M. R. Andrews, and W. Ketterle, *Collisionless and Hydrodynamic Excitations of a Bose-Einstein Condensate*, Phys. Rev. Lett. **81**, 500 (1998).

[45] S. Stringari, *Collective Excitations of a Trapped Bose-Condensed Gas*, Phys. Rev. Lett. **77**, 2360 (1996).

[46] S. Giovanazzi, L. Santos, and T. Pfau, *Collective oscillations of dipolar Bose-Einstein condensates and accurate comparison between contact and dipolar interactions*, Phys. Rev. A **75**, 015604 (2007).

[47] S. E. Pollack, D. Dries, R. G. Hulet, K. M. F. Magalhães, E. A. L. Henn, E. R. F. Ramos, M. A. Caracanhas, and V. S. Bagnato, *Collective excitation of a Bose-Einstein condensate by modulation of the atomic scattering length*, Phys. Rev. A **81**, 053627 (2010).

[48] H. Abe, T. Ueda, M. Morikawa, Y. Saitoh, R. Nomura, and Y. Okuda, *Faraday instability of superfluid surface*, Phys. Rev. E **76**, 046305 (2007).

[49] A. I. Nicolin, R. Carretero-González, and P. G. Kevrekidis, *Faraday waves in Bose-Einstein condensates*, Phys. Rev. A **76**, 063609 (2007).

[50] A. I. Nicolin and M. C. Raportaru, *Faraday waves in high-density cigar-shaped Bose–Einstein condensates*, Physica A **389**, 4663 (2010).

[51] A. I. Nicolin and M. C. Raportaru, *Faraday waves in one-dimensional Bose-Einstein condensates*, Proc. Rom. Acad. **12**, 209 (2011).

[52] A. I. Nicolin, *Faraday waves in Bose-Einstein condensates subject to anisotropic transverse confinement*, Rom. Rep. Phys. **63**, 1329 (2011).

[53] S. Balasubramanian, R. Ramaswamy, and A. I. Nicolin, *Faraday waves in cigar-shaped Bose-Einstein condensates with radially inhomogeneous scattering lengths*, Rom. Rep. Phys. **65**, 820 (2013).

[54] R. Nath and L. Santos, *Faraday patterns in two-dimensional dipolar Bose-Einstein condensates*, Phys. Rev. A **81**, 033626 (2010).

[55] K. Łakomy, R. Nath, and L. Santos, *Faraday patterns in coupled one-dimensional dipolar condensates*, Phys. Rev. A **86**, 023620 (2012).

[56] A. I. Nicolin, *Density waves in dipolar Bose-Einstein condensates*, Proc. Rom. Acad. **14**, 35 (2013).

[57] F. Kh. Abdullaev, M. Ögren, and M. P. Sørensen, *Faraday waves in quasi-one-dimensional superfluid Fermi-Bose mixtures*, Phys. Rev. A **87**, 023616 (2013).

[58] P. Capuzzi and P. Vignolo, *Faraday waves in elongated superfluid fermionic clouds*, Phys. Rev. A **78**, 043613 (2008).

[59] R. A. Tang, H. C. Li, and J. K. Xue, *Faraday instability and Faraday patterns in a superfluid Fermi gas*, J. Phys. B **44**, 115303 (2011).

[60] H. Fu, L. Feng, B. M. Anderson, L. W. Clark, J. Hu, J. W. Andrade, C. Chin, and K. Levin, *Density Waves and Jet Emission Asymmetry in Bose Fireworks*, Phys. Rev. Lett. **121**, 243001 (2018).

[61] L. Salasnich, N. Manini, F. Bonelli, M. Korbman, and A. Parola, *Self-induced density modulations in the free expansion of Bose-Einstein condensates*, Phys. Rev. A **75**, 043616 (2007).

[62] A. Imambekov, I. E. Mazets, D. S. Petrov, V. Gritsev, S. Manz, S. Hofferberth, T. Schumm, E. Demler, and J. Schmiedmayer, *Density ripples in expanding low-dimensional gases as a probe of correlations*, Phys. Rev. A **80**, 033604 (2009).

[63] S. Manz, R. Bücker, T. Betz, Ch. Koller, S. Hofferberth, I. E. Mazets, A. Imambekov, E. Demler, A. Perrin, J. Schmiedmayer, and T. Schumm, *Two-point density correlations of quasicondensates in free expansion*, Phys. Rev. A **81**, 031610 (2010).

[64] A. I. Nicolin, *Resonant wave formation in Bose-Einstein condensates*, Phys. Rev. E **84**, 056202 (2011).

[65] P. Capuzzi, M. Gattobigio, and P. Vignolo, *Suppression of Faraday waves in a Bose-Einstein condensate in the presence of an optical lattice*, Phys. Rev. A **83**, 013603 (2011).

[66] K. Staliunas, *Removal of excitations of Bose-Einstein condensates by space- and time-modulated potentials*, Phys. Rev. A **84**, 013626 (2011).

[67] C. Gaul, E. Díaz, R. P. A. Lima, F. Domínguez-Adame, and C. A. Müller, *Stability and decay of Bloch oscillations in the presence of time-dependent nonlinearity*, Phys. Rev. A **84**, 053627 (2011).

[68] E. Díaz, A. G. Mena, K. Asakura, and C. Gaul, *Super–Bloch oscillations with modulated interaction*, Phys. Rev. A **87**, 015601 (2013).

[69] I. Brouzos and P. Schmelcher, *Controlled excitation and resonant acceleration of ultracold few-boson systems by driven interactions in a harmonic trap*, Phys. Rev. A **85**, 033635 (2012).

[70] F. K. Diakonos, P. A. Kalozoumis, A. I. Karanikas, N. Manifavas, and P. Schmelcher, *Geometric-phase-propagator approach to time-dependent quantum systems*, Phys. Rev. A **85**, 062110 (2012).

[71] I. Vidanović, A. Balaž, H. Al-Jibbouri, and A. Pelster, *Nonlinear Bose-Einstein-condensate dynamics induced by a harmonic modulation of the s-wave scattering length*, Phys. Rev. A **84**, 013618 (2011).

[72] H. Al-Jibbouri and A. Pelster, *Breakdown of the Kohn theorem near a Feshbach resonance in a magnetic trap*, Phys. Rev. A **88**, 033621 (2013).

[73] D. Kobyakov, A. Bezett, E. Lundh, M. Marklund, and V. Bychkov, *Quantum swapping of immiscible Bose-Einstein condensates as an alternative to the Rayleigh-Taylor instability*, Phys. Rev. A **85**, 013630 (2012).

[74] W. H. Hu, L. Jin, and Z. Song, *Dynamics of one-dimensional tight-binding models with arbitrary time-dependent external homogeneous fields*, Quantum Inf. Process. **12**, 3569 (2013).

[75] R. R. Sakhel, A. R. Sakhel, and H. B. Ghassib, *Nonequilibrium Dynamics of a Bose-Einstein Condensate Excited by a Red Laser Inside a Power-Law Trap with Hard Walls*, J. Low Temp. Phys. **173**, 177 (2013).

[76] A. Balaž, I. Vidanović, A. Bogojević, A. Belić, and A. Pelster, *Fast converging path integrals for time-dependent potentials: I. Recursive calculation of short-time expansion of the propagator*, J. Stat. Mech.: Theory Exp. **2011**, P03004 (2011).

[77] I. Vidanović, A. Bogojević, A. Balaž, and A. Belić, *Properties of quantum systems via diagonalization of transition amplitudes. II. Systematic improvements of short-time propagation*, Phys. Rev. E **80**, 066706 (2009).

[78] A. Bogojević, I. Vidanović, A. Balaž, and A. Belić, *Fast convergence of path integrals for many-body systems*, Phys. Lett. A **372**, 3341 (2008).

[79] A. Bogojević, A. Balaž, and A. Belić, *Asymptotic properties of path integral ideals*, Phys. Rev. E **72**, 036128 (2005).

[80] J. B. Sudharsan, R. Radha, M. C. Raportaru, A. I. Nicolin, and A. Balaz, *Faraday and resonant waves in binary collisionally-inhomogeneous Bose–Einstein condensates*, J. Phys. B: At. Mol. Opt. **49**, 165303 (2016).

[81] A. I. Nicolin, *Variational treatment of Faraday waves in inhomogeneous Bose–Einstein condensates*, Physica A **391**, 1062 (2012).

[82] N. W. McLachlan, *Theory and Application of Mathieu Functions*, Oxford University Press: New York (1951).

[83] W. Bao and W. Tang, *Ground-state solution of Bose–Einstein condensate by directly minimizing the energy functional*, J. Comput. Phys. **187**, 230 (2003).

[84] M. L. Chiofalo, S. Succi, and M. P. Tosi, *Ground state of trapped interacting Bose-Einstein condensates by an explicit imaginary-time algorithm*, Phys. Rev. E **62**, 7438 (2000).

[85] L. Lehtovaara, J. Toivanen, and J. Eloranta, *Solution of time-independent Schrödinger equation by the imaginary time propagation method*, J. Comput. Phys. **221**, 148 (2007).

[86] M. M. Cerimele, M. L. Chiofalo, and F. Pistella, *Numerical solution of the stationary Gross–Pitaevskii equation: tests of a combined imaginary-time-marching technique with splitting*, Nonlinear Anal. Theory Methods Appl. **47**, 3345 (2001).

[87] P. Muruganandam and S. K. Adhikari, *Fortran programs for the time-dependent Gross-Pitaevskii equation in a fully anisotropic trap*, Comput. Phys. Commun. **180**, 1888 (2009).

[88] D. Vudragović, I. Vidanović, A. Balaž, P. Muruganandam, and S. K. Adhikari, *C Programs for solving the time-dependent Gross-Pitaevskii equation in a fully anisotropic trap*, Comput. Phys. Commun. **183**, 2021 (2012).

[89] R. K. Kumar, Luis E. Young-S., D. Vudragović, A. Balaž, P. Muruganandam, and S. K. Adhikari, *Fortran and C programs for the time-dependent dipolar Gross-Pitaevskii equation in an anisotropic trap*, Comput. Phys. Commun. **195**, 117 (2015).

[90] Luis E. Young-S., D. Vudragović, P. Muruganandam, S. K. Adhikari, and A. Balaž, *OpenMP Fortran and C programs for solving the time-dependent Gross-Pitaevskii equation in an anisotropic trap*, Comput. Phys. Commun. **204**, 209 (2016).

[91] Luis E. Young-S., P. Muruganandam, S. K. Adhikari, V. Lončar, D. Vudragović, and A. Balaž, *OpenMP GNU and Intel Fortran programs for solving the time-dependent Gross-Pitaevskii equation*, Comput. Phys. Commun. **220**, 503 (2017).

[92] B. Satarić, V. Slavnić, A. Belić, A. Balaž, P. Muruganandam, and S. K. Adhikari, *Hybrid OpenMP/MPI programs for solving the time-dependent Gross–Pitaevskii equation in a fully anisotropic trap*, Comput. Phys. Commun. **200**, 411 (2016).

[93] V. Lončar, A. Balaž, A. Bogojević, S. Škrbić, P. Muruganandam, and S. K. Adhikari, *CUDA programs for solving the time-dependent dipolar Gross–Pitaevskii equation in an anisotropic trap*, Comput. Phys. Commun. **200**, 406 (2016).

[94] V. Lončar, Luis E. Young-S., S. Škrbić, P. Muruganandam, S. K. Adhikari, and A. Balaž, *OpenMP, OpenMP/MPI, and CUDA/MPI C programs for solving the time-dependent dipolar Gross–Pitaevskii equation*, Comput. Phys. Commun. **209**, 190 (2016).

[95] R. K. Kumar, V. Lončar, P. Muruganandam, S. K. Adhikari, and A. Balaž, *C and Fortran OpenMP programs for rotating Bose–Einstein condensates*, Comput. Phys. Commun. **240**, 74 (2019).

[96] R. Achilles and A. Bonfiglioli, *The early proofs of the theorem of Campbell, Baker, Hausdorff, and Dynkin*, A. Arch. Hist. Exact Sci. **66**, 295 (2012).

[97] F. Casas, A. Murua, and M. Nadinic, *Efficient computation of the Zassenhaus formula*, Comput. Phys. Commun. **183**, 2386 (2012).

[98] M. Edwards and K. Burnett, *Numerical solution of the nonlinear Schrödinger equation for small samples of trapped neutral atoms*, Phys. Rev. A **51**, 1382 (1995).

[99] S. Ronen, D. C. E. Bortolotti, and J. L. Bohn, *Bogoliubov modes of a dipolar condensate in a cylindrical trap*, Phys. Rev. A **74**, 013623 (2006).

[100] G. M. Amdahl, *Validity of the Single Processor Approach to Achieving Large Scale Computing Capabilities*, Spring Joint Computer Conference, Atlantic City, New Jersey, 18-20 April 1967.

[101] The HDF Group, *Hierarchical Data Format, version 5*, (1997-2019).

Biography of the author

Dušan Vudragović was born on 3 May 1980 in Sremska Mitrovica, Republic of Serbia. He completed his primary school education at the Elementary school "Dositej Obradović" in Putinci, and continued his education at the "Stevan Puzić" high school in Ruma. He started undergraduate studies in the field of applied physics and informatics at the Faculty of Physics, University of Belgrade in 1999. During the studies, he received scholarships from the Ministry of Science of the Republic of Serbia, and the Government of the Republic of Serbia, as well as the award for the best 1000 students in Serbia from the Norwegian Embassy in Belgrade. He graduated in 2005 with GPA 9.62/10. Dušan's diploma thesis entitled "Measurement of the Effective Transverse Ion Beam Emission" was done under the supervision of Prof. Dr. Ivan Aničin.

From 2006 to 2008 he worked at CERN, Geneva within the framework of the FP6 projects SEE-GRID-2 (SEE-GRID eInfrastructure for regional eScience) and EGEE-II (Enabling Grids for E-sciencE). He started PhD studies in the field of particle physics at the Faculty of Physics, University of Belgrade in 2012, and switched to the condensed matter physics in 2016 under the supervision of Dr. Antun Balaž.

Dušan Vudragović is employed at the Institute of Physics Belgrade as a research assistant at the Scientific Computing Laboratory of the National Center of Excellence for the Study of Complex Systems. He is a member of two national research projects: ON171017, led by Dr. Antun Balaž, and III43007, as part of the workpackage PP4 led by Dr. Aleksandar Bogojević. As a part of international cooperation, he was involved in several FP6, FP7, and Horizon 2020 projects. Currently, he is involved in two Horizon 2020 projects, SMARTCHAIN and NI4OS-Europe.

Dušan Vudragović has published 23 papers in peer-reviewed international journals and presented his results at various international conferences. The results of this thesis are published in 5 papers in leading international journals.

Изјава о ауторству

Име и презиме аутора - **Душан Вудраговић**

Број индекса – **2016/8020**

Изјављујем

да је докторска дисертација под насловом

Faraday waves in ultracold dipolar Bose gases

(Фарадејеви таласи у ултрахладним диполним Бозе гасовима)

- резултат сопственог истраживачког рада;
- да дисертација у целини ни у деловима није била предложена за стицање друге дипломе према студијским програмима других високошколских установа;
- да су резултати коректно наведени и
- да нисам кршио/ла ауторска права и користио/ла интелектуалну својину других лица.

Потпис аутора

У Београду, 31. 08. 2019. год.

Душан Вудраговић

Изјава о истоветности штампане и електронске верзије докторског рада

Име и презиме аутора – **Душан Вудраговић**

Број индекса – **2016/8020**

Студијски програм - **Физика кондензованог стања**

Наслов рада - **Faraday waves in ultracold dipolar Bose gases (Фарадејеви таласи у ултрахладним диполним Бозе гасовима)**

Ментор - **др Антун Балаж**

Изјављујем да је штампана верзија мог докторског рада истоветна електронској верзији коју сам предао ради похрањења у **Дигиталном репозиторијуму Универзитета у Београду.**

Дозвољавам да се објаве моји лични подаци везани за добијање академског назива доктора наука, као што су име и презиме, година и место рођења и датум одбране рада.

Ови лични подаци могу се објавити на мрежним страницама дигиталне библиотеке, у електронском каталогу и у публикацијама Универзитета у Београду.

Потпис аутора

У Београду, 31. 08. 2019. год.

Душан Вудраговић

Изјава о коришћењу

Овлашћујем Универзитетску библиотеку „Светозар Марковић“ да у Дигитални репозиторијум Универзитета у Београду унесе моју докторску дисертацију под насловом:

Faraday waves in ultracold dipolar Bose gases (Фарадејеви таласи у ултрахладним диполним Бозе гасовима)

која је моје ауторско дело.

Дисертацију са свим прилозима предао/ла сам у електронском формату погодном за трајно архивирање.

Моју докторску дисертацију похрањену у Дигиталном репозиторијуму Универзитета у Београду и доступну у отвореном приступу могу да користе сви који поштују одредбе садржане у одабраном типу лиценце Креативне заједнице (Creative Commons) за коју сам се одлучио/ла.

1. Ауторство (CC BY)

2. Ауторство – некомерцијално (CC BY-NC)

3. Ауторство – некомерцијално – без прерада (CC BY-NC-ND)

④. **Ауторство – некомерцијално – делити под истим условима (CC BY-NC-SA)**

5. Ауторство – без прерада (CC BY-ND)

6. Ауторство – делити под истим условима (CC BY-SA)

(Молимо да заокружите само једну од шест понуђених лиценци.
Кратак опис лиценци је саставни део ове изјаве).

Потпис аутора

У Београду, 31. 08. 2019. год.

Душан Вудраговић

1. **Ауторство**. Дозвољавате умножавање, дистрибуцију и јавно саопштавање дела, и прераде, ако се наведе име аутора на начин одређен од стране аутора или даваоца лиценце, чак и у комерцијалне сврхе. Ово је најслободнија од свих лиценци.

2. **Ауторство – некомерцијално**. Дозвољавате умножавање, дистрибуцију и јавно саопштавање дела, и прераде, ако се наведе име аутора на начин одређен од стране аутора или даваоца лиценце. Ова лиценца не дозвољава комерцијалну употребу дела.

3. **Ауторство – некомерцијално – без прерада**. Дозвољавате умножавање, дистрибуцију и јавно саопштавање дела, без промена, преобликовања или употребе дела у свом делу, ако се наведе име аутора на начин одређен од стране аутора или даваоца лиценце. Ова лиценца не дозвољава комерцијалну употребу дела. У односу на све остале лиценце, овом лиценцом се ограничава највећи обим права коришћења дела.

4. **Ауторство – некомерцијално – делити под истим условима**. Дозвољавате умножавање, дистрибуцију и јавно саопштавање дела, и прераде, ако се наведе име аутора на начин одређен од стране аутора или даваоца лиценце и ако се прерада дистрибуира под истом или сличном лиценцом. Ова лиценца не дозвољава комерцијалну употребу дела и прерада.

5. **Ауторство – без прерада**. Дозвољавате умножавање, дистрибуцију и јавно саопштавање дела, без промена, преобликовања или употребе дела у свом делу, ако се наведе име аутора на начин одређен од стране аутора или даваоца лиценце. Ова лиценца дозвољава комерцијалну употребу дела.

6. **Ауторство – делити под истим условима**. Дозвољавате умножавање, дистрибуцију и јавно саопштавање дела, и прераде, ако се наведе име аутора на начин одређен од стране аутора или даваоца лиценце и ако се прерада дистрибуира под истом или сличном лиценцом. Ова лиценца дозвољава комерцијалну употребу дела и прерада. Слична је софтверским лиценцама, односно лиценцама отвореног кода.